TEMPERATURE-DEPENDENCE OF STRESS-RELATED PHENOMENA AT CONFINED DIMENSION

by

RAHMAT SAPTONO

Presented to the Faculty of the Graduate School of

The University of Texas at Arlington in Partial Fulfillment

of the Requirements

for the Degree of

DOCTOR OF PHILOSOPHY

THE UNIVERSITY OF TEXAS AT ARLINGTON

May 2014

Copyright © by Rahmat Saptono 2014

All Rights Reserved

Acknowledgements

The author wishes to thank Supervising Professor Choong-un Kim of the UT Arlington for suggesting the topic developed in this dissertation along with guidance and supports. He wishes to express his gratitude to Prof. Efstathios Meletis, Prof. Seong Jin Koh, Prof. Yaowu Hao, Prof. Nancy L. Michael, and Prof. Kyungsuk Yum, the Members of Committee, for having dedicated their time and assistances. Special thanks to MSE Department Chair, Academic Advisor, Faculties, Supporting Staffs, and Group Members.

The author acknowledges his debt to the Indonesian and US Governments for their supports through 3 years Fulbright-DIKTI Program followed by Graduate Research Assistantship provided by his Supervising Professor.

May 09, 2014

Abstract

TEMPERATURE-DEPENDENCE OF STRESS-RELATED PHENOMENA

AT CONFINED DIMENSION

Rahmat Saptono, PhD

The University of Texas at Arlington, 2014

Supervising Professor: Choong-Un Kim

Efforts have been made to develop a simple but physically sound model. The model was specifically proposed to capture, explain, and estimate the temperature sensitivity and strengthening mechanism phenomena in small volume material with particular reference to the roles grain boundary and surface. Model-inspired phenomenology approach was applied to reveal the key mechanisms and find directions for a more complete constitutive model.

The model was developed in the limited space where diffusion is insignificant. It was assumed that the plastic flow was predominantly governed by the thermally-activated process of dislocation glide overcoming barriers. Simple mathematical functions were formulated and evaluated to model the behavior. The figures of merit functions were fitted into the experimental data to evaluate physical parameters. Normalization was performed prior to the regression analysis to extract real variables and allow global evaluation.

Behavior of the small volume materials subjected to temperature variation within the range of argument can be generally condensed, described and predicted by an exponential decay model. In particular, the models are able to explain the responsible mechanism behind the observed phenomena. Important findings had been concluded

through the model application along with simplified observation and analysis. Surface is not a part of main strengthening mechanism. Thin film exhibits atypical high flow stress because of high density grain boundary and dislocation density, which is a true effect of confinement. Grain boundary strengthening becomes weaker and mechanism becomes short-range in thin films with small grains.

Exponential decay model explains the temperature-dependence of flow stress behavior in small volume metallic materials with physical validity. The validity is proven by finding a direct connection of the model to the established physical mechanistic model in the field. Despite of quite a few limitations, it provides directions for more complete and advanced constitutive equations and guidance for further investigations through physical experiment.

Table of Contents

Acknowledgements iii

Abstract iv

Table of Contents vi

List of Illustrations vii

List of Tables xi

Chapter 1 Introduction 1

Chapter 2 Literature Review 29

Physical Mechanistic Foundations 29

General Models for the Temperature-dependence of Flow Stress 37

Specific Issues and Models at Confined Dimension 44

Chapter 3 Method 68

General Procedure and Approach 68

Assumptions 69

Model Descriptions 69

Data Collection and Preparation 71

Analysis 72

Chapter 4 Results 76

Chapter 5 Discussion 108

Chapter 6 Conclusion 159

References 160

Biographical Information 167

List of Illustrations

Figure 1-1 Temperature-dependence of yield strength in thick and thin film of Al, Cu, and Au interconnects 24

Figure 2-1 A simplified model of gliding dislocation pinned by discrete obstacles 30

Figure 2-2 A schematic illustration of a dislocation segment pinned by local obstacles and two corresponding free body diagrams of the segment under equilibrium 31

Figure 2-3 Thermally-activated dislocation glide resistance diagram 33

Figure 2-4 Schematic of long-range and short-range internal stress fields..........36

Figure 2-5 Dislocation line model at confined dimension and corresponding crss as predicted by force balance analysis..........44

Figure 2-6 Schematic illustration of thickness-dependence of strength 46

Figure 2-7 Bending of a threading dislocation in a strained film on a substrate..........47

Figure 2-8 Dislocation motions in a film at confined dimension 48

Figure 2-9 Illustration of misfit dislocation movement in thin film on substrates..........51

Figure 2-10 Schematic illustrations of a dislocation line passed through a film on substrate..........52

Figure 2-11 Schematic illustrations of possible dislocations configuration associated with strain hardening 53

Figure 2-12 A cylindrical disc model of thin film grain..........55

Figure 2-13 Cross-sectional TEM image of a 350nm thick epitaxial Al film deposited on a single crystal (0001) alpha-$Al_2 0_3$ substrate..........56

Figure 2-14 Cross sectional TEM image of a 350nm thick epitaxial Al film deposited on a single crystal (0001) alpha-$Al_2 0_3$ substrate during heating..........57

Figure 2-15 Dynamic cross sectional TEM images during heating cycle of a 450nm thick polycrystalline Cu on a Si substrate with a-SiNx diffusion barrier 58

Figure 2-16 Schematic illustration of dislocation core spreading 59
Figure 2-17 Plan-view TEM images of Cu grains at 600°C and 130°C............................60
Figure 3-1 General flow chart for physical modeling of material 68
Figure 3-2 Model-inspired phenomenology approach 69
Figure 3-3 Proposed model I 70
Figure 3-4 Proposed model II 70
Figure 3-5 Proposed model III 71
Figure 4-1 Data plot corresponding to proposed model I..76
Figure 4-2 Data plot corresponding to proposed model II...77
Figure 4-3 Data plot corresponding to proposed model III..78
Figure 4-4 Preliminary analysis of bulk materials 79
Figure 4-5 Preliminary analysis of confined materials 80
Figure 4-6 Linear plot of Al bulk materials corresponding to proposed model I 81
Figure 4-7 Linear plot of Al bulk materials corresponding to proposed model II 82
Figure 4-8 Linear plot of Al bulk materials corresponding to proposed model III 83
Figure 4-9 Linear plot of Al bulk materials in Zone I and Zone II corresponding to
proposed model I 84
Figure 4-10 Linear plot of Al bulk materials in Zone I and Zone II corresponding to
proposed model II 85
Figure 4-11 Linear plot of Al bulk materials in Zone I and Zone II corresponding to
proposed model III 86
Figure 4-12 Linear plot of Al confined materials corresponding to proposed model I 87
Figure 4-13 Linear plot of Al confined materials corresponding to proposed model II......88
Figure 4-14 Linear plot of Al confined materials corresponding to proposed model III.....89
Figure 4-15 Linear plot of Cu bulk materials corresponding to proposed model I............90

Figure 4-16 Linear plot of Cu bulk materials corresponding to proposed model II...........91

Figure 4-17 Linear plot of Cu bulk materials corresponding to proposed model III..........92

Figure 4-18 Linear plot of Cu bulk materials in Zone I corresponding to proposed model I 93

Figure 4-19 Linear plot of Cu bulk materials in Zone I corresponding to proposed model II 94

Figure 4-20 Linear plot of Cu bulk materials in Zone I corresponding to proposed model III 95

Figure 4-21 Linear plot of Cu bulk materials in Zone II corresponding to proposed model I 96

Figure 4-22 Linear plot of Cu bulk materials in Zone II corresponding to proposed model II 97

Figure 4-23 Linear plot of Cu bulk materials in Zone II corresponding to proposed model III 98

Figure 4-24 Linear plot of Cu confined materials corresponding to proposed model I 99

Figure 4-25 Linear plot of Cu confined materials corresponding to proposed model II ..100

Figure 4-26 Linear plot of Cu confined materials corresponding to proposed model III .101

Figure 4-27 Linear plot of Au confined materials corresponding to proposed model I ...102

Figure 4-28 Linear plot of Au confined materials corresponding to proposed model II ..103

Figure 4-29 Linear plot of Au confined materials corresponding to proposed model III .104

Figure 5-1 Typical (averaged) behavior of confined materials 108

Figure 5-2 Idealized and real description of the behavior 109

Figure 5-3 A reciprocal of homologous temperature plot representing the temperature-dependence of mechanical behavior in typical metals..110

Figure 5-4 Comparison of bulk and small volume datasets of Cu 112

Figure 5-5 Model I fitted to the experimental data of confined Al 114

Figure 5-6 Model II fitted to the experimental data of confined Al 115

Figure 5-7 Model III fitted to the experimental data of confined Al 116

Figure 5-8 Model I fitted to the experimental data of confined Cu....................................117

Figure 5-9 Model II fitted to the experimental data of confined Cu...................................118

Figure 5-10 Model III fitted to the experimental data of confined Cu 119

Figure 5-11 Model I fitted to the experimental data of confined Au 120

Figure 5-12 Model II fitted to the experimental data of confined Au 121

Figure 5-13 Model III fitted to the experimental data of confined Au 122

Figure 5-14 Model I, II, III fitted to the experimental data of confined Al..........................123

Figure 5-15 Model I, II, III fitted to the experimental data of confined Cu 124

Figure 5-16 Model I, II, III fitted to the experimental data of confined Au 125

Figure 5-17 Model to data fit check of linearized logarithmic reciprocal model (model III check to confined Cu data)..131

Figure 5-18 Model to data global fit to small volume Cu..143

Figure 5-19 Model to data global fit to small volume Al 143

Figure 5-20 Model to data global fit to small volume Au 144

Figure 5-21 Comparison of the two models 147

Figure 5-22 Exponential decay model...149

Figure 5-23 Exponential decay model to small volume Cu data global fit 150

Figure 5-24 Three key size parameters of dimensional and micro-structural constraints 152

Figure 5-25 Role of grain boundary from Al data sets 154

Figure 5-26 Role of surface from Au data sets...155

Figure 5-27 Findings from Cu data sets..156

List of Tables

Table 1-1 Summary of temperature-dependence of stress studies[1-41] 4

Table 3-1 Data for materials[97] 72

Table 4-1 Linear regression analysis (least-squares fit to straight line) of Bulk Al and Cu 105

Table 4-2 Linear regression analysis (least-squares fit to straight line) of confined Al data 106

Table 4-3 Linear regression analysis (least-squares fit to straight line) of confined Cu data 106

Table 4-4 Linear regression analysis of confined Au data >500nm...............................106

Table 4-5 Linear regression analysis of confined Au data <500nm...............................107

Table 5-1 Physically sound parameters obtained from the models...............................135

Chapter 1

Introduction

Despite of the fact that the primary function of electronic materials is not to carry mechanical loading, the importance of stress-related phenomena cannot be overlooked. In electronic packaging stress is generally a result of an interaction between a small volume material and its environment. The so called interaction stress may be generated by the difference of CTE and lattice orientation as well as the evolution structure and modification of bonding at the interface/surface. In a particular situation, the stress may become the root cause of excessive deformation, void and hillock, crack and delamination, resulting in a structural failure. Alternatively, the migration of electrons alone may also produce stress.

In small geometry, this problem is reasonably much intensified as a tiny discontinuity or excess is significant enough to produce a functional failure. Failure of a sub functional unit may result in the malfunction of the entire system. We learned from these causes and effects that stress-related phenomena are very important in term of reliability.

One of the important phenomena is the temperature-dependence of flow stress. In thin film metal interconnects, the permanent respond of polycrystalline thin film metal to loading can be identified as a key phenomenon. Characterizing when a polycrystalline thin film metal starts to flow under different range of arguments, therefore, is not only interesting and challenging but also relevant and important in terms of design, fabrication, use, and performance. Qualitative and quantitative understandings are both imperative in achieving the ultimate benefits of physical experimentation.

Studies of temperature-dependent stress in confined interconnect materials have been long-established since the late 1960s. In 1969, Castro and Campbell[1] studied the temperature dependence of stress in Al film of 1000 nm thick attached to an oxidized Si, produced by the evaporation technique. Since then, many studies have been performed in the space of interest. The status of temperature-dependence of flow stress studies is summarized in Table 1-1 and Figure 1-1[1-42].

Aims of studies varied from the practical measurement and description of stress with respect to temperature cycling, to the quantitative interpretation of appeared behavior, the identification of general and specific mechanisms, the prediction of the behaviors including the practical estimation and control of reliability. Various thicknesses of materials have been studied ranging from 1000 nm to 100 nm. Most of these materials were films attached to Si wafer substrates of various geometries and conditions, fabricated by various techniques under various process condition including evaporation, electron beam deposition, and magnetron sputtering. Methods are varied but the radius of curvature measurements coupled with in situ XRD-based or LASER-based optical techniques were typically used. Range of temperature varied from $0.008T_M$ to $0.9T_{M,}$ but most of them were set between Room Temperature and 550°C. In addition to high purity Al, Al alloy with minor wt% of Si, Cu, and Ti had also been investigated[1-6].

Cu and Au interconnects came into play in the early 1990s. In 1991, Flinn[7] reported the mechanical behavior of 1000 nm Cu thin film attached on Si wafer in the range of temperature between room temperature and 600°C. A former study on Au film on substrate was also reported in 1991 by Katz et.al.[12]

Processes, preparation, and measurements techniques were almost similar to those established in Al studies. New techniques of stress measurements have been developed and employed including nano-indentation, micro-tensile test, bulge test, and

membrane resonance. In the early 2000s, in-situ TEM techniques were employed in addition to the common experimental setup aimed at developing more detailed understanding of the mechanical behavior related the existing theories of plasticity.

Table 1-1 Summary of temperature-dependence of stress studies[1-41]

Material	Substrate/Structure	Temperature Range (^oC)	Methods	Aims of Study	References
Al film (99.999%) Thickness (nm): 1000 *(Evaporated)*	Si beam, Si wafer Dimension: 15 x 3 mm 100μm thick Layer: 500 nm SiO_2 both side (steam oxidized)	RT – 500 RT – 300 -196 – 50	Radius of curvature measurement XRD (In situ)	To study stress in Al film with regard to temperature cycling.	Castro & Campbell (1969)
Al film Thickness (nm): 200–1600 *(Electron beam deposited)* Passivation: SiN (PCVD) or P-glass (CVD)	(100) Si wafer Dimension: 2 inch 0.012 inch thick Layer: SiO_2 (steam oxidized)	25 – 500	Radius of curvature measurement Laser-based optical-lever technique. (In situ)	To measure stress as a function of temperature for Al film with various thickness for a number of heating and cooling cycles.	Sinha & Sheng (1977)

Table 1-1 Continued

Al film Thickness (nm): 460 *(Electron beam deposited)* 480 *(DC magnetron sputtered)*	(001) Si strip Dimension: 25 mm x 2 mm 115 μm thick Layer: 500 nm SiO_2 (thermally oxidized)	RT – 320	Radius of curvature measurement XRD (In situ)	To measure stress relaxation at various temperatures in Al thin films deposited on Si. To identify the stress relaxation mechanism by considering stress-temperature behavior	Hershkovitz et.al. (1985)
Thin films of: 99.999% Al 99.95% W. Thickness (nm): 210,260,420,590,1090 (Al) 70,110,160,220,450 (W) *(Magnetron sputtered at Room Temp.)*	(100) Si wafer p-type 5-20 μΩ Layer: 100 nm SiO_2 (thermally oxidized)	RT – 450	Radius of curvature measurement Laser-based optical-lever technique. (In situ) Room Temp. Nano-indentation.	To describe the application of substrate bending technique and sub micron indentation technique to determine the strength of two materials used for metallization	Doerner et.al (1986)

Table 1-1 Continued

Thin films of Al-1%Si Al-1%Si2%Cu Al-1%Si3%Ti Thickness (nm): 1000 (typical) *(Sputtered)*	Si wafer Dimension: 500 μm (typical)	RT – 450	Radius of curvature measurement Laser-based optical-lever technique. (In situ)	To derive the relation between stress in thin film on substrate and corresponding elastic deformation of the substrate To describe the use of a laser scanning technique to measure the stress-induced curvature of waver and hence the film To present experimental results for stress in Al-Si as a function of temperature To present theoretical analysis of the elastic plastic behavior of the films.	Flinn et.al. (1987)

Table 1-1 Continued

Thin film of Al-1%Si, Al-2%Cu Thickness (nm): 210, 590 *(Magnetron sputtered at Room Temp.)*	(100) Si wafer p-type 5-20$\mu\Omega$ Layer: 100 nm SiO_2 (thermally oxidized)	RT – 450	Radius of curvature Laser-based optical-lever technique. (In situ)	To discuss quantitative interpretation of stress during thermal cycling and plastic deformation mechanisms, their relation to hillock.	Gardner & Flinn (1988)
Thin film of Al and its alloys Layered Al alloys Thickness (nm): varied *(Magnetron sputtered at Room Temp.)*	Si wafers p-type 5-20$\mu\Omega$ Layer: 100 nm SiO_2 (thermally oxidized)	RT – 550 (varied)	Radius of curvature Laser-based optical-lever technique. (In situ)	To determine the impact of stress on the growth of silicide-induced stress by bending a thin Si substrate and then annealing the samples while bent.	Gardner & Flinn (1990)

Table 1-1 Continued

Thin films of: Al-1%Si Al-1%Si-0.5%Cu Thickness (nm): 800 *(Magnetron sputtered)* Passivation: P-SiN, P-SiN/PSG	Si substrate Layer: SiO_2 (thermally oxidized)	RT – 450	XRD Inclined incident Method	To explain voiding failure comprehensively by mean of those aspects on metallization stress obtained experimentally To be able to estimate and control the practical reliability of the device.	Tezaki et.al. (1990)
Cu thin film Thickness (nm): 1000 *(Sputtered)*	Si wafer Dimension: 100 mm Layer: 100 nm SiO_2 (thermally oxidized)	RT – 600	Radius of curvature measurement Laser-based optical-lever technique. Inverted optical system (In situ)	To investigate and attempt to understand the mechanical behavior of thin film.	Flinn (1991)

Table 1-1 Continued

Thin films of: Al 1%Si Al0.75%Si0.5%Cu Thickness (nm): 100 *(DC magnetron sputtered)*	(100) n-type Si wafer Dimension: 150 mm dia. 675 μm thick Layer: SiO_2 (steamed oxidized) Oxide, oxy-nitride, nitride insulating layer (PECVD) Phosphorous doped glass capping layer (APCVD & LPCVD)	25 – 400	Radius of curvature measurement Laser-based optical-lever technique. (In situ)	To characterize metal film stress over a very wide temperature range.	Draper & Hill (1991)

Table 1-1 Continued

Au thin Film Thickness (nm): 100 *(Electron beam deposited)*	Corning cover-glass of soda-lime type (Soda-lime glass containing SiO, as the major constitu-ent and has a nomi-nal composition in wt. %. of SiOz:Naz:CaO: MgO:A1,O&O, = 72.6:15.2: 4.6: 3.6:1.7:0.8)	25-500	Radius of curvature measurement (In situ) TEM, SEM, SIMS	To measure stress for thin gold film grown on glass substrate during heating and cooling cycles in the temperature range 25-500°C To correlate the measured stress to microstructural changes in the gold layer and to interfacial reaction between the gold and the glass substrate	Katz et.al. (1991)
(99.9998%) Cu thin film Thickness (nm): 1000 *(Magnetron sputtered)*	(100) Si wafer Dimension: 125 mm Layer: SiO_2 (oxidized)	25 – 450	Radius of curvature measurement Optical-based technique	To predict stresses developed in thin blanket film subjected to thermal cycling based on an analysis of existing creep model.	Thouless et.al. (1993)

Table 1-1 Continued

Al thin film Thickness (nm): 500 *(UHV evaporated)* 500 nm grain size	Si wafer Dimension: 150 μm thick, Layer: SiO_2 on one side (oxidized)	RT – 500	Radius of curvature measurement Laser-based optical-lever technique. (In situ)	To determine dominant deformation mechanism.	Volkert et.al. (1994)
Al-1wt%Si-0.5wt% Cu thin film Thickness: 800 nm *(Sputtered)* Passivation: Nitride 1.19 mm thick (PECVD)	(100) Si wafer Dimension: 2 inch Layer: SiO_2 (thermally oxidized)	RT – 420	Radius of curvature measurement (in situ)	To examine the kinetics of tensile stress relaxation mechanism in Al-Si- Cu layer at temperature between 45°C and 165°C	Witvrouw et.al. (1994)
Continuous Cu film Thickness (nm): 200, 400, 800, 1200 *(RF magnetron sputtered)* random orientation and {111} fiber texture Passivation: Si_2N_4 0.2, 0.05, 0.025, 0.0125 μm thick	(100) Si wafer Layer: 35 nm SiO_2 (thermally oxidized) Layer: Ta barrier	RT – 400	XRD Method	To determine effects of film texture, thickness, and passivation layer.	R.P. Vinci et.al. (1995)

Table 1-1 Continued

Al(0.5wt% Cu) thin film Thickness (nm): 800 *(Sputtered)*	(100) Si wafer Dimension: 6 inch Layer: SiO_2 (thermally oxidized)	RT – 450	Radius of curvature measurement (in situ)	To study the kinetics of tensile stress relaxation in Al(0.5wt%Cu) film,	Proost et.al. (1997)
Cu thin film Thickness (nm): 450-1000, 300 *(Magnetron sputtered at Room Temp.)* Passivation: Si_2N_4 50 nm thick	Si wafer Layer: SiO_2 50 or 100 nm Si_2N_4 Diffusion Barrier on both side	RT – 600	Radius of curvature measurement (in situ)	To study the thermal stress behavior of Cu films having thickness of between 450 nm and 1000 nm with and without a thin (50 nm) Si nitride passivation layer.	Keller et.al. (1998)
High purity (99.999%) Cu film Thickness (nm): 40, 400 *(Electron beam deposited)* Passivation: Cu 1 nm thick layer SiO_x 8, 80 nm thick	Si substrate Layer: SiO_2 10 nm thin Cr interlayer	RT – 450	Radius of curvature measurement Laser interfero-meter technique (in situ)	To measure stress in passivated Cu film including their dependence on temperature and thickness.	Shen et.al. (1998)

Table 1-1 Continued

Pure (99.999%) Au film Thickness (nm): 2100 *(Thermally evaporated)*	Si waver Layer: SiO_2 *(patterned oxidized)* Free standing tensile specimens *(standard lithographic technique)*	RT – 600	Micro tensile test	To demonstrate procedures for performing uniaxial tensile tests on free-standing thin films at elevated temperature To use these methods to characterize gold film approximately 2 μm thick.	Emery et.al. (1998)
Al alloy (Al-1%Si) thin film Thickness (nm): 500 (nominal) *(RF magnetron sputtered)*	Single crystal (100) Si wafer Dimension: (20 mm x 20 mm) 380 $\pm$ 15 μm thick	RT – 450	Radius of curvature measurement Laser beam deflection system (in situ)	To better understand thermal cycling behavior.	Koike et.al. (1998)
Thin films of: Al-0.5wt%Cu Al-1wt%Si-0.5wt%Cu Thickness (nm): 800 *(Sputtered)*	(100) Si wafer Dimension: 5 and 6 inch Layer: SiO_2 (thermally oxidized)	RT – 450 (Al-Cu) RT – 420 (Al-Si-Cu)	Radius of curvature measurement (in situ)	To examine the kinetics of tensile stress relaxation mechanisms of Al-Cu and Al-Si-Cu type films at temperatures between 45-175°C.	Witvrouw et.al. (1999)

Table 1-1 Continued

Cu film Thickness (nm): 600-1000 on one side. *(Sputtered)*	Si substrate Layer: Si_3N_4 barrier on both sides	RT – 600	Radius of curvature measurement (in situ).	To obtain correspondence between experiment and simulation.	Keller et.al. (1999)
Au film Thickness (nm): 100-2500	(100) Si wafer Dimension: 100 mm Layer: Low stress Si Nitride Diffusion Barrier W and Ti Adhesion Layer 10 nm	RT – 600	Radius of curvature measurement (in situ)	To study strain gradient plasticity limited to the thicker than about 1000 nm thickness.	Leung et.al. (2000)
Cu Film (99.999% purity) Thickness (nm): ~ 500 *(Magnetron sputtered at Room Temp.)*	(100) Si wafer Dimension: 500 μm thick Layer: 50 nm thick Amorphous SiOx Amorphous SiNx diffusion barrier	RT – 600	Radius of curvature measurements (in situ)	To analyze thermal- stress-induced dislocation plasticity and dislocation- interface interactions.	Dehm et.al. (2001)

Table 1-1 Continued

Cu Film Thickness (nm): 300,450,500,600,1000 *(Sputtered)* Passivation: 50 nm Si_3N_4 *(Sputtered)*	(100) Si wafer Layer: SiO_2 (oxidized) 100 nm Si_3N_4 barrier on both side (CVD)	RT – 600	XRD Method (in situ)	To complement study on stresses distribution in Cu film.	Baker et.al. (2001)
Cu film Thickness (nm): 500 (nominal) 535 (actual) *(Magnetron sputtered)*	(111) Si wafer Layer: 600 nm SiO2 (thermally oxidized)	RT – 520	Radius of curvature measurement Laser-based optical-lever technique. (In situ)	To analysis the stra-in hardening behavi-or of thin metallic films on substrates focusing on the idea of an additional contribution to strain hardening that arises from the interaction of a threading dislocations laying parallel to it.	Weihnacht and Bruckner (2001)

Table 1-1 Continued

Thin film of: Pure Cu Dilute Cu-Al *(UHV sputtered)*	(100) Si wafer Dimension: 2 inch Layer: 50 nm SiOx on both side (thermally oxidized) SiNx diffusion barrier (CVD)	RT – 500	Radius of curvature measurement Laser scanning	To study thermal stress evolution in pure Cu and self-passivated Cu-Al alloy film.	Weiss et.al. (2001)
Cu foils *(Electrodeposited, Rolled, and Annealed)*	Foils of various conditions and thicknesses are glued to a specially designed grip. Free-standing tensile specimen	RT - 300	Special designed laser speckle based dilatometer (LSBD)	To provide a link between mechanical properties of bulk and thin materials To form a basis for a quantification of size effect	Weiss et.al. (2002)

Table 1-1 Continued

Cu film Thickness (nm): 500 *(Unpassivated/ Self-passivated Cu-1at.%Al film)* *Cu film Thickness (nm): 700*	Si substrate Layer: SiNx Diffusion Barrier Polymide substrate	RT – 500	Radius of curvature measurement (in situ) XRD (in situ)	To describe current level of understanding of dislocation plasticity in thin films and small structures in which the film or structure dimension plays important role.	Kraft et.al. (2002)
Cu film Thickness (nm): 400 *(Electron beam deposited)* Passivation: SiO_x ~80 nm thick	Si substrate Layer: SiO_2 Thin Cr interlayer diffusion barrier.	RT – 450	Radius of curvature measurement (in situ)	To characterize and model thermo-mechanical response of Cu thin film To present general experimental featu-res on the thermo-mechanical respon-se of passivated Cu films and the deve-lopment of the cons-titutive model.	Ege & Shen (2003)

Table 1-1 Continued

Cu film Thickness (nm): 400, 250,40 *(Sputtered)* Passivation: SiOx (20% of Cu film thick) Thickness (nm): 1000 *(Sputtered)* Passivation: SiOx 50 nm thick	Si substrate Layer: SiO_2 15 nm thin Cr interlayer diffusion barrier Layer: SiO_2 50 nm Ta interlayer barrier	-196 - 600	Radius of curvature measurement (in situ)	To develop a detailed understanding of the mechanical behavior of passivated Cu films in particular the temperature-dependent elastic plastic response within the continuum framework.	Shen & Ramamurty (2003)
Al films Thickness (nm): 33, 107, 205 *(Electron beam deposited)*	Si wafer Dimension: 720 μm thick a 210 nm tensile film of SiN*x*	25 – 300	Membrane Resonance (the natural ‘‘drum-head’’ resonant frequency of a rectangular membrane)	To investigate stress relaxation behavior of Al films 33, 107, and 205 nm thick.	Hyun et.al. (2003)

Table 1-1 Continued

Cu and Al film Epitaxial Polycrystalline Thickness (nm): 100-2000 *(Magnetron sputtered)*	Single crystal (0001) a-Al_2O_3 Dimension: 50 mm 330 μm thick (Epitaxial) (001) Si substrates Dimension: 50 mm 280 μm thick (Polycrystaline) Layer: 50 nm thick a-SiOx or 100 nm bilayer a-SiNx/a-SiOx Inter-diffusion barrier (nitrided/oxidized)	RT – 500 (Cu) RT – 400 (Al)	Radius of curvature measurement Laser scanning (in situ)	To summarize recent advances in thin film plasticity. To study stress-temperature evolution of the various thin films in term of existing theories of plasticity in thin metals under consideration of recent in situ transmission TEM.	Dehm et.al (2003)

Table 1-1 Continued

Polycrystalline Al thin films (99.999%) Thickness (nm): 500-4400 *(Magnetron sputtered)*	Films are deposited on Photoresist covered glass plates and released in an acetone bath. Free standing specimen	RT – 240	Bulge Test	To study the plastic behavior of free standing thin Al film during biaxial Bulge testing. To investigate the influence of the initial film thickness and deformation temperature.	Cieslar (2004)
Thin films of Au and Cu (RF sputtered) Thickness (nm): 3200 (Cu/Pt) 2700 (Au)	(100) Si wafer Dimension: 3 μm thick Layer: 5-10 nm Pt layer	RT - 130	High Temperature Nano-indentation	To describe nano-indentation technique for measuring sputter-deposited Au and Cu thin film's mechanical properties at elevated temperatures up to 130 °C.	Volinsky et.al. (2004)

Table 1-1 Continued

Ultrathin film of: Au Au/SiN_x SiN_x/Au/SiN_x Thickness (nm): 80 -500 (varied) *(DC Magnetron sputtered)* Passivated/Unpassivated Passivation: SiN_x inter & surface layer	Dogbone-shaped Kapton polyimide substrates with a gauge section of 6 x 20 mm 125-mm-thick Free standing tensile specimen	-150 - 200	Novel Synchrotron based tensile testing technique. XRD Optical strain measurement CCD Camera	To adapt other techniques to elevated temperatures in order to achieve more defined loading conditions.	Gruber et.al. (2008)
np Au thin film Thickness (nm): 45-75 *(Sputtered at RT)*	(100) oriented Si wafer Layer: 10 nm a-SiO_x 50 nm a-SiN_x 10 nm Ta Adhesive interlayer 10 nm Au Adhesive Stabilizer interlayer	RT – 200	Wafer curvature measurement	To discuss the fabrication and characterization of blanket np-Au thin films that is completely crack-free over the dimensions (75 mm) of the Si wafer substrate.	Sun et.al. (2008)

Table 1-1 Continued

Gold nano wire nanocrystalline (20-30 nm) grain size nanostructured (20 nm high, 40 nm width, and 1 mm long) *(combination of extreme UV lithography and a lift-off process using the XIL beam line of SLS)*	125 μm thick Kapton polymide foil (top up approach) 2 nm Cr interlayer	-100 - 170	$Sin^2 \varphi$ -tensile test using powder diffraction stage of Materials Science beamline at SLS.	To study the temperature dependence of the yield strength and the onset of cracking of gold nanowires on flexible polymide substrate.	Olliges et.al. (2009)
Gold nano lines and thin films Thickness/Dimension: 20 nm 40 nm x 20 nm x 1 mm *(EUV-IL)* Passivation: 700 nm parylene on top	125 μm thick Kapton polymide foil (top up approach) 2 nm Cr interlayer	-100 - 120	$Sin^2 \varphi$ -tensile test.	To investigate the thermo-mechanical properties of (i) 20 nm thick homogeneous gold thin films (ii) 40 nm width, 20 nm height, 1 mm length.	Olliges et.al. (2011)

Table 1-1 Continued

Cu thin film Thickness (nm): 650 *(Sputtered)* Capping Layers: - 35 nm thick SiCxNyHz film deposited at 350°C. - 7.5 nm thick CoWP film - hybrid cap	(001) Si wafers Dimension: 300 mm dia. Layers: 30/10 nm thick barrier layers 80 nm thick seed layer Conventional barrier layers.	25 - 350	In situ Glancing-Incident GIXRD measurement.	To address the effects of capping material on the mechanical response Cu films and patterned feature during thermal excursions.	Murray et.al. (2012)
Nanocrystalline Au thin film *(RF Sputtered)*	Dog-bone-shaped micro-tensile specimens Gauge Sections: 100 mm length 100 mm width 850 nm thickness (Free standing)	23 - 110	Micro-tensile Test	To investigate the contribution of different mechanisms of inelastic deformation in nano-crystalline Au thin films studied in the range of 10^{-5}-10 s^{-1} and 298–383 K.	Karanjgaokar (2012)

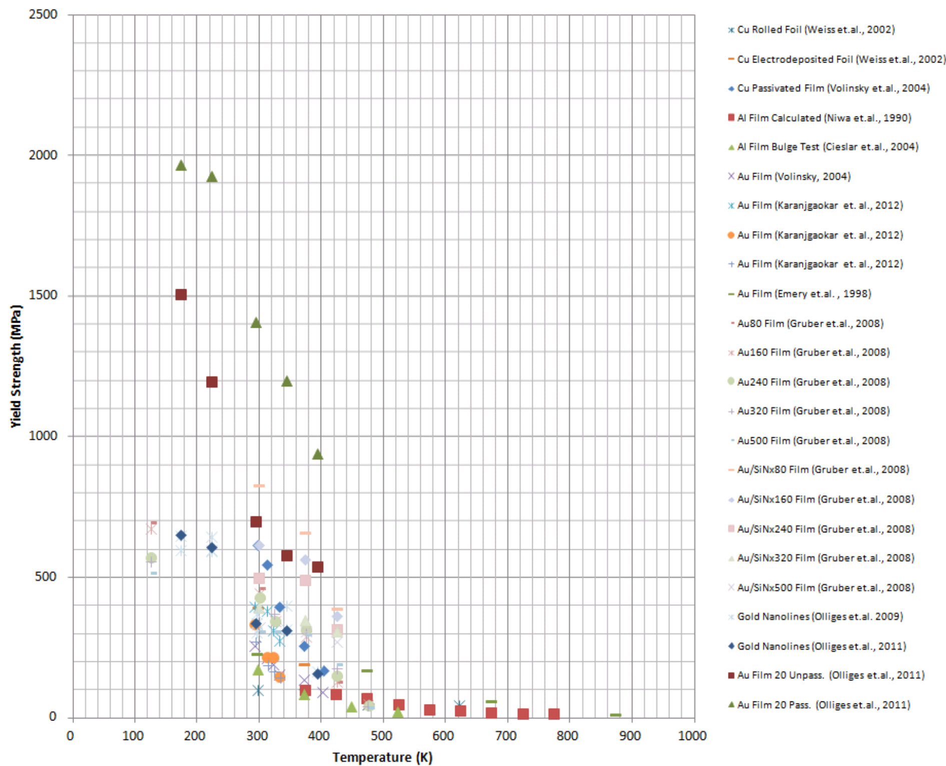

Figure 1-1 Temperature-dependence of yield strength in thick and thin film of Al, Cu, and Au interconnects

(after ref.[29,35-39,41,42])

Study of the flow stress in various temperatures was traditionally more established in bulk materials[43-48]. Not only has the study of the behavior at confined dimension been challenging the design and ability of test structure but also opening the reinterpretation of the long established theories and models. Area of study involves free standing thin films and those attached on substrates and covered by confinements.

Different behaviors are expected in confined materials by some common arguments. Hardwick[49] highlighted (1) reduced geometry and (2) increased surface to volume ratio as two key reasons in free-standing materials. The first argument had a

direct consequence on the length of dislocation and the geometry of slip plane. Reduction of dislocation length would typically increase strength whereas the confinement of slip plane would reasonably change the nature of strengthening. Moreover, decreased length would hinder the operation of dislocation sources. More pronounced contributions of irregularities and oxide films on the surface are believed to be the manifestation of increasing surface to film ratio. An irregularity raises stress whereas a film pins and inhibits dislocation at the exit. Process history also contributes to the different behavior. Effects of characteristic process-history on thin film geometry and morphology had been elaborated by Alexopoulos and Sullivan[50].

Despite of these common grounds, the mechanism of plastic deformation at confined dimension has not been fully understood. Although the role of dislocations in plastic deformation is unquestionable, their characteristics and behaviors may be altered quite significantly at confined dimensions. As a result, the operating mechanism and hence the appeared behavior will also change. One of the most widely accepted facts is the increase of yield with the reduction of thickness[51]. It is also well recognized that the observed behavior in confined materials may also be sensitively influenced by the sample geometry as well as surface and interface conditions.

Frost[52] reviewed comprehensively the mechanism of plastic deformation in thin film. It was assumed that the operating mechanism at atomic level was the same. Unique condition at surface and interface, however, might result in a peculiar total mechanism. It was also believed that there was a characteristic dimension of dislocations that really worked in bulk material.

Roles of interface misfit dislocations in confined materials was revealed by Matthews[53] in the earlier literature. Murakami et.al.[54,55] studied the behavior of dislocations in a Pb thin film attached on a substrate. It was observed that dislocation

crossed in thickness direction from one side to another side on which the film was confined by native surface oxide layer, boundaries, and interfaces. No source of dislocation, however, was assumed to operate as indicated by the unchanged density of dislocation. Both parallel and inclined planes of gliding were observed. Strength model were developed based on dislocation theories including force criterion, work hardening effects, and energy criterion. Freund[56,57] and Nix[58,59] elaborated unique characteristics of dislocation in thin film on substrate and developed a constitutive model for the thickness-dependence of stress.

Dislocation plasticity in thin metal films and small structures was purposely reviewed in ref.[61]. It was concluded that while the general trend was able to be captured (i.e. the smaller the stronger), the functional dependence was not clearly established, either empirically or theoretically. Geometry of grains in polycrystalline metals and the chemistry of the interfaces had added to the uncertainty. Moreover, Kraft et.al.[62], strongly believed that *"there was no scaling law with one universal power-law exponent encompassing the entire range"*. Instead, they believed that, *"there are different physical mechanisms giving rise to the inelastic deformation for different size regimes and various boundary conditions"*[62]. Shortly, it was assumed that the behavior, in addition to the dimension, depended more complexly on the traditional and other parameters, which cannot be generalized by a simple single law.

Attempts have been made to model the temperature-dependent behavior to achieve more benefits of bulk experimental data. A phenomenological model, which is essentially an empirical fit of the data, is used only to encapsulate the phenomena. A physical model, more importantly, contains the essential physics of the problem and also has a predictive power[63].

A physical model should be developed based on the application of the first principles and used to describe the mechanisms. An ideal model, referring to Kocks[64], should provide a general relation between the external measureable parameters of mechanical behavior and the internal parameter of microscopic structures that is applicable in a wide range of conditions for many materials. Number of material parameters should be ideally kept minimum and able to be measured in a simple way[64].

Essentially, accurate phenomenological descriptions and sound physical mechanistic foundations are a pre-requisite for establishing such a general relation[65]. In general, the closer the phenomenological description to the physical foundations, the more likely it can be interpolated and extrapolated. Practically, a physically sound model should be able to pass both interpolation and extrapolation test.

A general philosophy of developing such a physical-mechanistic constitutive model for plasticity was reviewed in ref.[3], making the use of the basic thermodynamics and kinetics theory. Physical-based model, however, is not always easy to be constructed due to the higher level of complexities. According to Ashby[63], (1) structure evolution, (2) multiple mechanisms, (3) linked processes, and (3) spatial variations, are the source of these complexities. At confined dimensions, most of them are assumed to come into play. One of the most reliable approaches to deal with such complexities is "model-inspired phenomenology approach"[64,65]. In a particular situation, this semi-empirical approach may also produce a physically-sound model.

General purpose of the present study is to gain sound understanding and new insight into the temperature-dependence of yield strength in confined key metals interconnect while capturing the temperature-dependent aspects of the phenomena in an appropriate constitutive equation.

This dissertation is written through a main central hypothesis which is constructed from the following research questions:

1. What are the physical origin and the ruling mechanism of the observed temperature-dependence of flow stress?
2. What are the most suitable constitutive models and equations to describe the appeared behavior in the space of interest?
3. Can a model, which is developed by a thermally-activated dislocation-mediated obstacle-controlled model-inspired phenomenology approach, predict the behavior at confined dimension?

Main hypothesis of this dissertation is that, *"a sound model can be developed to describe and predict the behavior of key metals interconnect at confined dimension by using a model-inspired phenomenology approach"*

Most important purpose of this dissertation is, therefore, to determine a general relationship between temperature and flow stress at confined dimension based on relevant data published in literatures, which must be proven by sound statistical analysis as well as reasonable physics and explained mechanism.

The results of this dissertation will expectantly provide significant implications in both theoretical and practical aspects of temperature-dependence stress related phenomena particularly in the design, processing, testing and applications of confined metallization lines.

Chapter 2

Literature Review

Temperature-dependence of flow stress has been studied extensively for many reasons and purposes. In bulk structural material, there have been established theories, methods, and models. In confined materials, however, they may not readily work. Instead, they have to be reviewed, redesigned and reinterpreted. This chapter presents (1) physical mechanistic foundations for the temperature-dependence of flow stress, (2) general models for temperature-dependence of flow stress, (3) specific issues and models at confined dimension.

Physical Mechanistic Foundations

Physics deals with established theories or first principles underlying physical phenomena. Mechanism deals with a process taken place at atomic levels which results in a measurable plastic strain. Plastic deformation occurs generally through distinct or simultaneous mechanisms comprising three basic mechanisms: (1) stress-induced transformation, (2) dislocation movements, and/or (3) transport phenomena. The most important controlling mechanisms in most cases with particular reference to the present study are dislocation glide and/or climb mechanism. Of a particular interest is a region of thermal activation, in which the behavior is chiefly governed by the thermally-activated movement of dislocation line overcoming short-range barriers.

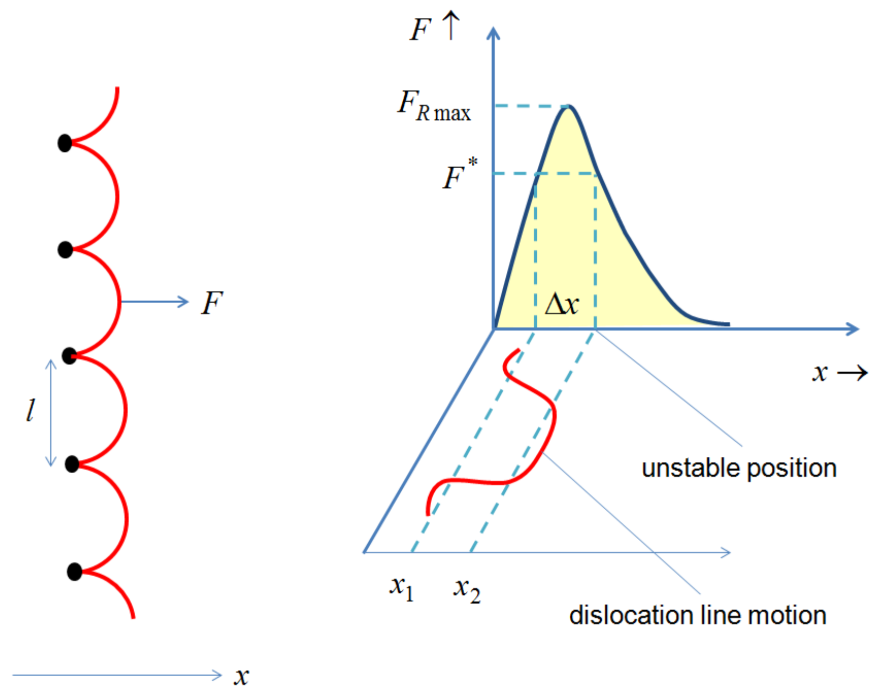

Figure 2-1 A simplified model of gliding dislocation pinned by discrete obstacles (after ref.[66])

General model of the mechanism is depicted in Figure 2-1. Mechanical equilibrium of a dislocation segment pinned by discrete local obstacles was illustrated in Figure 2-2. It can be seen from the figure that the obstacles exert reactive forces F_R of equal magnitude in opposite direction as a force F is applied to the segment. The tension of the dislocation segment T can also be specified from another free body diagram.

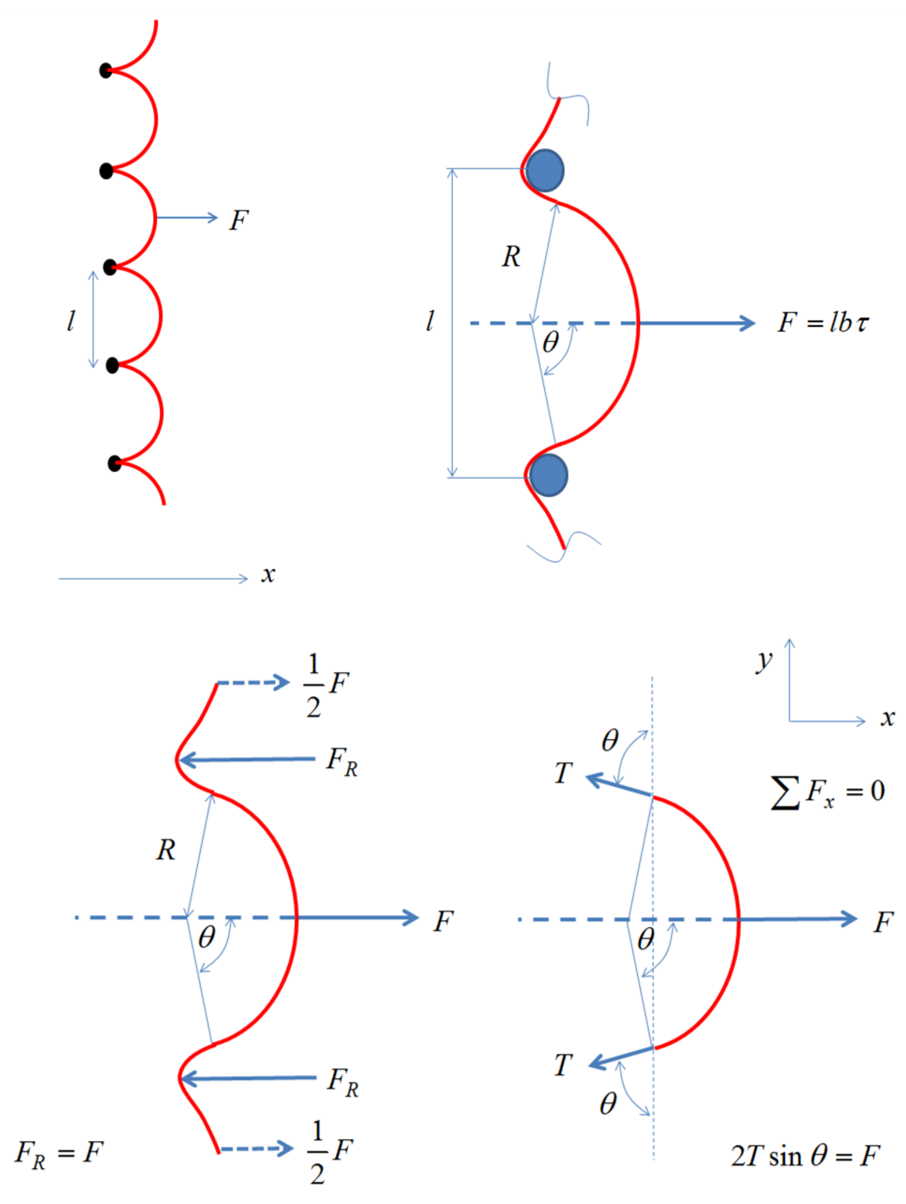

Figure 2-2 A schematic illustration of a dislocation segment pinned by local obstacles and two corresponding free body diagrams of the segment under equilibrium (after ref.[67])

Assuming that the dislocation line will only pass the obstacles when each obstacle is no longer able to bear the forces exerted by the segment on it, a critical condition can be defined by simply applying mechanical equilibrium. The derivation can be found elsewhere, for example in ref. [67].

From the general equation of force equilibrium:

$$\sum F_x = 0 \quad \text{2-1}$$

$$F = F_R \quad \text{2-2}$$

The force applied to the segment of dislocation can be assumed as:

$$F = \tau b l \quad \text{2-3}$$

where:

b = Burger vector

l = a spacing between two obstacles

By using a taut string analogy[67], the line tension of the dislocation can be approximated from the stored energy per unit length.

$$T \approx \frac{\mu b^2}{2} \quad \text{2-4}$$

where:

μ = shear modulus

The resistance force can be defined as:

$$F_R = 2T \sin\theta = \mu b^2 \sin\theta \quad \text{2-5}$$

From the equilibrium of forces, the stress exerted on each obstacle can be defined as a function of the line geometry.

$$\tau b l = \mu b^2 \sin\theta \quad \text{2-6}$$

$$\tau = \frac{\mu b}{l}\sin\theta \qquad \text{2-7}$$

The critical value can also readily be interpreted from Eq. 2-5.

$$\frac{(F_R)_{\max}}{\mu b^2} = \sin\theta \qquad \text{2-8}$$

It can be readily seen from Eq. 2-8 that the only limiting factor in the equation is ***sin*** θ, which is the dimensionless measure of the *obstacles strength*.

Thermodynamic equation of dislocation line overcoming obstacles model had been used to derive the key relationship of stress vs. temperature[68].

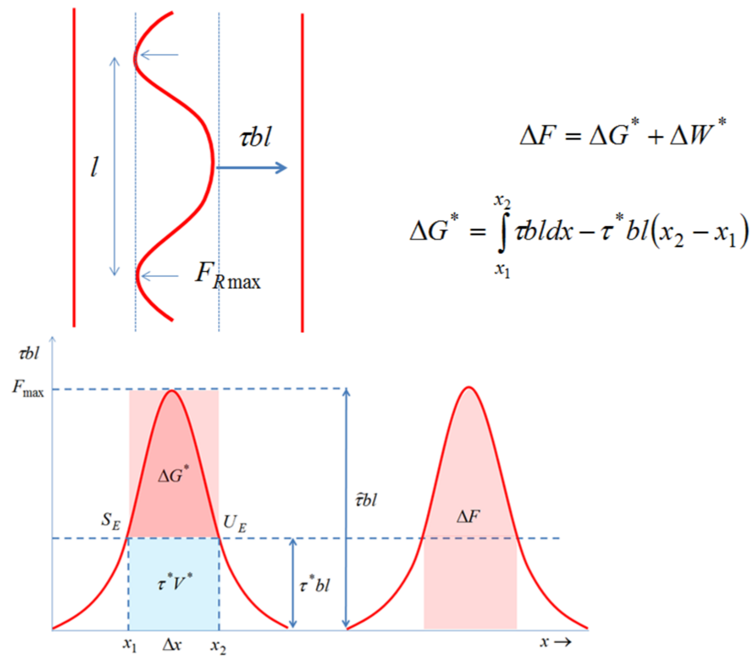

Figure 2-3 Thermally-activated dislocation glide resistance diagram

ΔG^* = Gibbs Free Energy of Activation, ΔF = Helmholtz Free Energy (= Obstacle Energy), W^* = Mechanical Work Done by the Applied Stress, and $\hat{\tau} bl$ = Mechanical Threshold Force at 0 K. (after ref.[68])

Thermodynamically, there is a certain amount of energy that a dislocation line must overcome to move from one (stable) equilibrium position (x_1) to another (unstable) equilibrium position (x_2). The *threshold* energy is illustrated by the area under force displacement curve in Figure 2-3. The Helmholtz *total free energy* (*ΔF*) is the sum of the *mechanical work* produced by the applied shear stress over an *activation volume* V^* (ΔW^*) and the Gibbs *free energy of thermal activation* (ΔG^*). Plastic deformation is governed all together by the mechanical and thermal components of this *energy barrier* (the *obstacle energy*). The activation energy is the thermal component of energy required to activate the dislocation line on top of the mechanical component.

At absolute zero, at which the thermal activation energy is non-existing, plastic deformation is totally governed by the mechanical work. At above 0 K, the plastic flow is depending on the probability that a system has an energy of ΔG^* (or larger) to successfully change its state by thermal activation. This *probability of success* refers to the Boltzmann Law from the very basic of thermodynamics[67,68].

$$P(\Delta G) \propto \exp \frac{-\Delta G}{kT} \qquad \text{2-9}$$

S*uccessful rate* of dislocation overcoming obstacles events is dependent on the *attempts frequency* and the *success probability* defined by Eq. 2-9. *Rate of activation*, therefore, can be expressed as the product of *a frequency factor* and *a* Boltzmann *factor*[68].

$$P_t = \upsilon_0 \exp \frac{-\Delta G}{kT} \qquad \text{2-10}$$

When the *strain-rate* at a given stress and temperature is dictated by *thermal release* and the *net of release* is approximated by the *forward activation rate*, an Arrhenius equation can be written as[68]:

$$P_t = \frac{\dot{\gamma}}{\gamma_0} = \upsilon_0 \exp\frac{-\Delta G}{kT} \qquad \text{2-11}$$

A dislocation kinetics equation then can be written in term of macroscopic strain-rate:

$$\frac{\dot{\gamma}}{\dot{\gamma}_0} = \exp\frac{-\Delta G}{kT} \qquad \text{2-12}$$

It can be seen from

Figure 2-3, that ΔG^* is a function of the applied stress τ^*. Idealizing the geometry of the resistance profile into a rectangular, the *activation energy* can be roughly estimated as:

$$\Delta G\left(\tau^*\right) = \Delta F\left[1 - \frac{\tau^*(T)}{\tau^*(0)}\right] \qquad \text{2-13}$$

For short-range obstacles, Eq. 2-13 can, then, be generalized by defining a phenomenology equation[68]:

$$\Delta G(\tau/\hat{\tau}) = g_0 \mu b^3 \left[1 - \left(\frac{\tau}{\hat{\tau}}\right)^p\right]^q \qquad \text{2-14}$$

where:

$g_0 =$ normalized activation energy

$\mu =$ shear modulus

$b =$ Burger vector

The empirical constants, $0 < p \le 1; 1 \le q \le 2$, are depending on the obstacle profile.

In addition to the short-range barriers, there exist long-range barriers in deformed crystal. Thermal activation is, however, far lesser than sufficient to help dislocation

dealing with this type of barriers. Interaction of dislocations with these barriers, therefore, is less sensitive to the temperature. Nevertheless, it depends indirectly on the temperature through the temperature-dependence of shear modulus. Conrad[69], based upon previous established theories, had reviewed extensively the a-thermal component of the flow stress. The basic concepts are summarized in Figure 2-4.

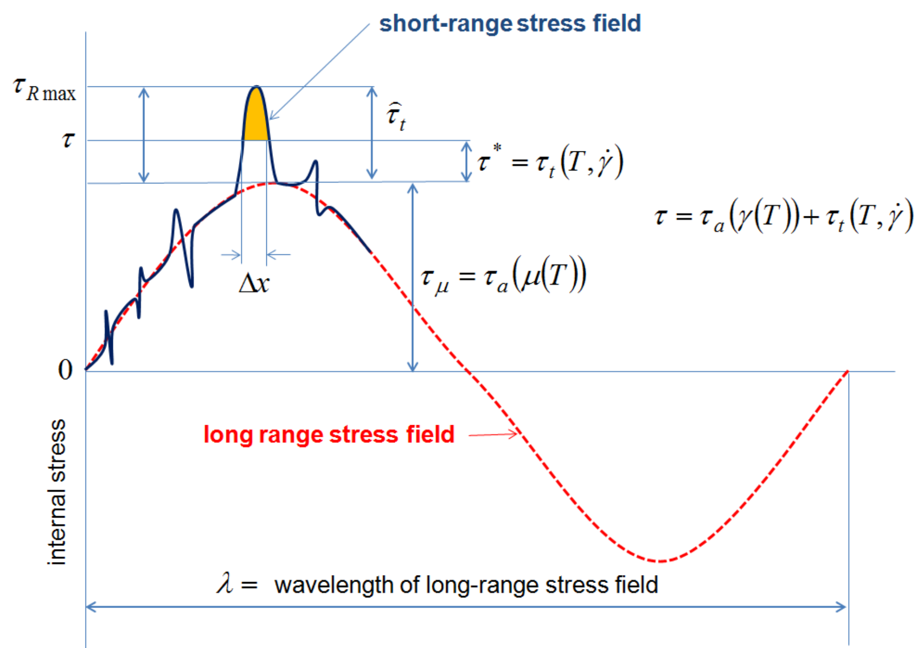

Figure 2-4 Schematic of long-range and short-range internal stress fields

(not in scale, after ref.[69])

From now on, the flow stress will be considered to be consisted of: (1) a-thermal component and (2) thermal component.

$$\tau = \tau_a + \tau_t \qquad 2\text{-}15$$

where:

$\tau =$ flow stress

$\tau_a =$ a-thermal component of flow stress that characterizes rate-independent interaction of dislocations with long range-barriers.

$\tau_t =$ thermal component of flow stress that characterizes rate-dependent interaction of dislocations with short-range obstacles.

General Models for the Temperature-dependence of Flow Stress

The earliest related physical model established in bulk structural materials was initiated from the study of the variation of flow stress of steel with strain rate[70]. The equivalence effects of strain rates and temperature on the relation of stress-strain was assumed and formulated in a single parameter involving the rate characteristics of materials itself associated with the heats of activation.

$$Z(\dot{\varepsilon}, T) = \dot{\varepsilon} \exp(Q/RT) \qquad 2\text{-}16$$

$$\sigma = \sigma(Z, \varepsilon) \qquad 2\text{-}17$$

Based on this assumption, a particular temperature-strain rate condition always has its equivalence at different temperature. This situation gives a practical benefit when such a condition is difficult to be achieved. One of the practical limitations of the Zener-Hollomon (Z-H) model is its range of use. Moreover, the ruling mechanism was not well explained in microscopic details.

Zerilli-Armstrong (Z-A) model[71] and mechanical threshold stress (MTS) model[68] are two important physical-mechanistic based models that were developed on the basis of dislocation plasticity theories. Dislocation plasticity models generally assume that the average velocity of microscopic dislocation motion, which is sequentially related

to the macroscopic strain rate, is dictated by a thermal activation process. The Gibbs free energy of activation is assumed to be dependent on the stress, in addition to the geometry of dislocations.

Zerilli and Amstrong[71] used a physical dimension, i.e. the area of activation or the mean value of it, to characterize the thermal activation process. It was revealed that a particular structure has its own dislocation characteristics by which the behavior is governed. Two constitutive equations have been developed to describe the thermal activation behavior of BCC and FCC materials from the first principles.

$$\sigma_{t,bcc} = c_1 \exp\left(-c_3 T + c_4 T \ln \dot{\varepsilon}\right) \qquad \text{2-18}$$

$$\sigma_{t,fcc} = c_2 \varepsilon^{\frac{1}{2}} \exp\left(-c_3 T + c_4 T \ln \dot{\varepsilon}\right) \qquad \text{2-19}$$

Kocks et.al.[45,68,72,73] developed a model based on the argument that *a threshold stress*, i.e. the flow stress at 0 K, $\hat{\tau}$, can be used as a reference stress. It was assumed that the thermally-activated flow stress τ_t can always be linked to the internal state parameter $\hat{\tau}$ by introducing a scaled factor $s(\dot{\gamma}, T)$ containing an Arrhenius expression.

A foundation for the MTS model was constructed by involving the scaling factor comprising strain-rate and temperature-dependencies[72].

$$\tau = \tau_a + \hat{\tau}_t s(\dot{\gamma}, T) \qquad \text{2-20}$$

where:

τ = flow stress.

τ_a = a-thermal component of flow stress that characterizes the rate-independent interaction of dislocations with long-range barriers.

τ_t = thermal component of flow stress that characterizes the rate-dependent interaction of dislocations with short-range obstacles.

$\hat{\tau}_t$ = thermal component of MTS that characterizes the rate-independent interaction of dislocations with short-range obstacles.

$s(\dot{\gamma},T)$ = strain-rate and temperature dependencies factor.

With this foundation equation, the problems can be theoretically condensed into (1) the form of the factor s and (2) the description of MTS. In short, the flow stress can be described as a function of (1) current structure, (2) strain-rate, and (3) temperature[72].

$$\tau = f(\hat{\tau}_t, \dot{\gamma}, T) \qquad \text{2-21}$$

Macroscopically, the relationship between stress, temperature, and strain rate is enveloped in the Gibbs free energy of activation. According to MTS theory, Gibbs free energy of activation ΔG when T = 0K also corresponds to the mechanical threshold and hence the internal state parameter (see Eq. 2-13 and Eq. 2-14). Eq. 2-12 can be re-written as Eq. 2-22 or Eq. 2-23.

$$\dot{\gamma} = \dot{\gamma}_0 \exp\left[-\frac{\Delta G(\tau/\hat{\tau})}{kT}\right] \qquad \text{2-22}$$

$$\dot{\gamma} = \dot{\gamma}_0 \exp\left[-\frac{\Delta G(s(\dot{\gamma},T))}{kT}\right] \qquad \text{2-23}$$

To reflect the dependence of Gibbs free energy of activation to the stress, the phenomenological description of the free activation energy, which has already been revealed in Eq. 2-14, can be re-written as:

$$\Delta G(s(\dot{\gamma},T)) = g_0 \mu b^3 \left[1-(s(\dot{\gamma},T))^p\right]^q \qquad \text{2-24}$$

where:

$p,q =$ constants that characterize the geometry of obstacles profile

Substituting Eq. 2-24 into Eq. 2-23, the scaling factor can now be re-written as:

$$s(\dot{\gamma},T)=\frac{\tau_t}{\hat{\tau}_t}=\left[1-\left[\frac{kT\ln(\dot{\gamma}/\dot{\gamma}_0)}{g_0\mu b^3}\right]^{\frac{1}{p}}\right]^{\frac{1}{q}} \qquad \text{2-25}$$

It can be seen from the relationshipship that the scaling factor is basically a semi-empirical constant that contains the thermal activation term. This stress-dependence terms, which can be approached from both first principles and phenomenology, may also be represented by either activation area or activation work.

The MTS model used flow stress as an internal state parameter, linking it to the microstructure in both response and structure evolution equations. A scaling factor, i.e. a function of temperature and strain rate, was introduced to link directly any flow stresses at thermally-activated region to the reference stress.

MTS models had been developed and used extensively to describe the relationship between observed macroscopic behaviors and microscopic states of materials subjected to a temperature change.

Nemat-Nasser et.al. developed MTS-based constitutive equations for FCC poly-crystals with particular reference to OFHC Cu[74,75] (e.g. Eq. 2-26) as well as BCC poly-crystals with particular reference to Ta[76,77] (e.g. Eq. 2-27).

$$\tau(\dot{\gamma},\gamma,T)=\tau^0\left\{1-\left(\frac{kT}{g_0}\left[\ln\frac{\dot{\gamma}}{\dot{\gamma}_0}+\ln\left(1+a(T)\gamma^{\frac{1}{2}}\right)\right]\right)^{\frac{1}{2}}\right\}^{\frac{3}{2}}\left(1+a(T)\gamma^{\frac{1}{2}}\right)+\tau_a^0\gamma^{n1} \qquad \text{2-26}$$

where:

$$\tau^0 = \frac{g_0}{b\lambda l_0}$$
$$\dot{\gamma}_0 = b\rho_m \omega_0 l_0$$
$$a(T) = a_0\left[1 - (T/T_m)^2\right]$$

$$\tau^{(\alpha a)} = \operatorname{sgn}\dot{\gamma}^{(\alpha a)}\left\{g^{(\alpha a)}\left(\gamma^{(\alpha a)}, d_G^{(\alpha a)}, \ldots\right)\tau_{al}^{(\alpha a)}\right\} + \hat{\tau}_0^{(\alpha a)} f\left(\gamma_1^{(\alpha a)}, T\right) \times \ldots$$
$$\ldots\left[1 - \left(-\frac{kT}{g_0^{(\alpha a)}}\ln\frac{\left|\dot{\gamma}^{(\alpha a)}\right| f\left(\gamma_1^{(\alpha a)}, T\right)}{\dot{\gamma}_0^{(\alpha a)}}\right)^{\frac{1}{q}}\right]^{\frac{1}{p}} \quad \text{2-27a}$$

for $T \leq T_c^{(\alpha a)}$

$$\tau^{(\alpha a)} = \operatorname{sgn}\dot{\gamma}^{(\alpha a)}\left\{g^{(\alpha a)}\left(\gamma^{(\alpha a)}, d_G^{(\alpha a)}, \ldots\right)\tau_{al}^{(\alpha a)}\right\} \quad \text{2-27b}$$

for $T > T_c^{(\alpha a)}$

Such a particular physical-based model was developed based mainly upon the established concept of dislocation kinetics along with systematic empirical observations from experimental data. Scope of the models was mainly in the range of temperature and strain rate when the phenomena of atomic transport were not dominant and the plastic deformation was basically mediated by dislocation motions[78]. The model assumed that the resistance to the motion dictates the flow stress. In general, the flow stress equations were constructed from the summation of (1) thermally-activated component, (2) a-thermal component, and (3) viscous-drag component. Specifically, Nemat-Nasser[78] also introduced strain as a load parameter dictating the change of dislocation density in a-thermal region. This parameter can be simplified by assuming a simple power law representation and averaging the value of reference shear modulus. In viscous region, a phenomenological constitutive equation with a material constant measured directly at very high strain rate and high temperature, were also introduced. A

single parameter representing an effective damping to dislocation motions was able to be specified. Later on, Nemat-Nasser[78] proposed three-dimensional model based on the same principles.

More applicative MTS models for key structural materials have also been established. Specific physical-based models for Steel, for example, were developed by Goto et.al.[79] (Eq. 2-28), Oussouaddi et.al.[80], and Banarjee[81] (Eq. 2-29).

$$\frac{\sigma}{\mu}=\frac{\sigma_a}{\mu}+\left[1-\left(\frac{kT}{g_0\mu b^3}\ln\frac{\dot{\varepsilon}_{0i}}{\dot{\varepsilon}}\right)^{\frac{1}{qi}}\right]^{\frac{1}{pi}}\cdot\left[1-\left(\frac{kT}{g_0\mu b^3}\ln\frac{\dot{\varepsilon}_{0\varepsilon}}{\dot{\varepsilon}}\right)^{\frac{1}{q\varepsilon}}\right]^{\frac{1}{p\varepsilon}}\cdot\frac{\hat{\sigma}_\varepsilon}{\mu_0} \qquad \text{2-28}$$

where:

$$\theta=\frac{\hat{\sigma}_\varepsilon}{d\varepsilon}=\theta_0\left\{1-\tanh\left(\alpha\frac{\hat{\sigma}_\varepsilon}{\hat{\sigma}_{\varepsilon S}}\right)\right\}+\theta_{IV}\ \tanh\left(\alpha\frac{\hat{\sigma}_\varepsilon}{\hat{\sigma}_{\varepsilon S}}\right)$$

$$\ln\left(\frac{\dot{\varepsilon}_{\varepsilon s0}}{\dot{\varepsilon}}\right)=-\frac{\mu b^3 g_{0\varepsilon s}}{kT}\ln\left(\frac{\hat{\sigma}_{\varepsilon s}}{\hat{\sigma}_{\varepsilon s0}}\right)$$

$$\mu=\mu_0-\frac{D}{\exp\left(\frac{T_0}{T}\right)-1}$$

$$\sigma\left(\varepsilon_p,\dot{\varepsilon},T\right)=\sigma_a+\left(s_i\sigma_i+s_e\sigma_e\right)\frac{\mu(p,T)}{\mu_0} \qquad \text{2-29}$$

Banerjee and Bhawalkar[82] developed a dedicated equation for Aluminum (Eq. 2-30).

$$\sigma\left(\sigma_e,\dot{\varepsilon},p,T\right)=\left[\tau_a+\tau_i\left(\dot{\varepsilon},T\right)+\tau_e\left(\sigma_e,\dot{\varepsilon},T\right)\right]\frac{\mu(p,T)}{\mu_0} \qquad \text{2-30}$$

Holmedal[83] generalized the MTS to accommodate applications in continuum and crystal plasticity. An elastic-plastic formulation had been developed to be implemented in a tensile/compression test involving tools modulus.

$$\tau_t = \frac{\mu}{\mu_0}\left(1-\left(\frac{kT}{(g_0/p)\mu b^3}\right)^{\frac{1}{q}} \ln\left(\frac{\dot{\gamma}_0}{\dot{\gamma}+\dot{\gamma}_{\min}}\right)\left|\ln\left(\frac{\dot{\gamma}_0}{\dot{\gamma}+\dot{\gamma}_{\min}}\right)\right|^{(1-q)/q}\right)^{\frac{1}{p}} \hat{\tau}_t \qquad \text{2-31a}$$

$$\tau_t = \frac{\mu}{\mu_0}\left(1-\left(1-\frac{pkT}{g_0\mu b^3} a\sinh\left(\frac{\dot{\gamma}}{2\dot{\gamma}_0}\exp\left(\frac{g_0\mu b^3}{pkT}\right)\right)\right)\times\left|1-\frac{pkT}{g_0\mu b^3} a\sinh\left(\frac{\dot{\gamma}}{2\dot{\gamma}_0}\exp\left(\frac{g_0\mu b^3}{pkT}\right)\right)\right|^{\frac{1-q}{q}}\right)^{\frac{1}{p}}$$

2-31b

The above modification allowed the MTS model to be fully used in continuum and polycrystal applications. Mathematical expression for the thermal stress component was presented in these two equations (2-31a and 2-131b)

Most recently, Cai et.al.[84] modified and combined the power law relations of Z-A and MTS model to predict the flow stress as a function of thermally-activated stress and temperature, over a large range of strain rate and temperature.

$$\sigma_t = q^{\frac{-1}{p}} \hat{\sigma}\left[(1+q)^{1-(kT/G_0)\ln(\dot{\varepsilon}/\dot{\varepsilon}_0)} - 1\right]^{\frac{1}{p}} \qquad \text{2-32}$$

Thermally-activated stress vanished when a critical temperature, T_c, was reached, i.e.

$\sigma_t = 0$, when $T \geq T_c = \left(\frac{G_0}{k}\right)\ln\left(\frac{\dot{\varepsilon}}{\varepsilon_0}\right)$

The equation can be re-written as:

$$\sigma_t = \hat{\sigma}\left\langle (q^{-1}+1)(\dot{\varepsilon}/\dot{\varepsilon}_0)^{(kT/G_0)\ln(1+q)} - q^{-1}\right\rangle^{\frac{1}{p}} \qquad \text{2-33}$$

where:

$\langle x \rangle$ is defined for $x \geq 0$ and 0 for $x < 0$

The new constitutive equation can also concurrently depict the change of activation volume with the thermally-activated stress and temperature.

Specific Issues and Models at Confined Dimension

Important developments and modifications of dislocation plasticity theories have been made to explain specific phenomena observed at confined dimension. Of the most important issues are the establishment of threading dislocations and the development of misfit dislocations.

In a confined single crystal thin film, a line of dislocation was assumed to be pinned by obstacles at surface/interface while force was being applied normal to it.

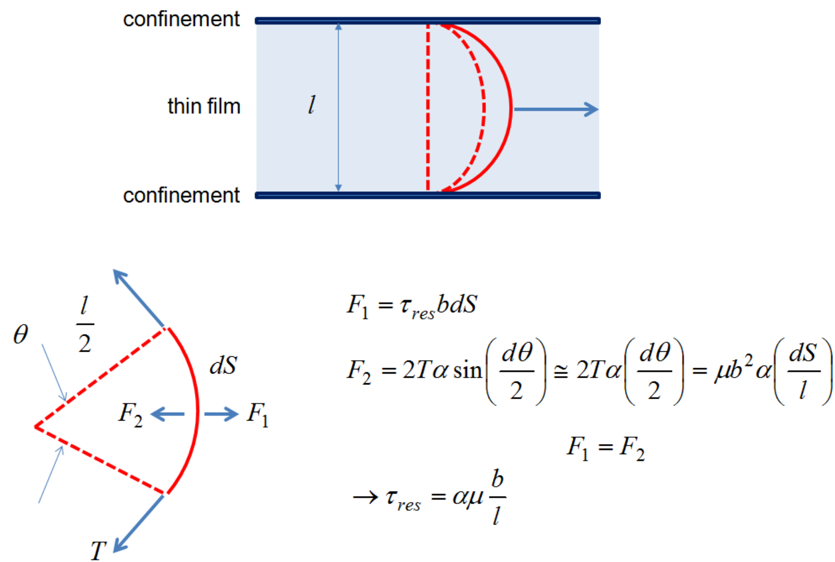

Figure 2-5 Dislocation line model at confined dimension and corresponding crss as predicted by force balance analysis

(after ref.[55])

Assuming a segment of dislocation line spanned in through-thickness direction, resolved shear stress can be theoretically calculated by employing a simple force balance analysis depicted in Figure 2-5[55]. A simple model was presented as[54]:

$$\tau_Y = \tau_0 + \frac{\alpha \mu b}{l} \qquad \text{2-34}$$

where:

α = a constant of magnitude 0.5-1.0.

Large discrepancies between the calculated (resolved) and observed stresses, however, were noticed, not only in free standing films but also in other metals on substrates. It was realized that the experimental data fitted in the equation only for the obstacle's spacing lower than the thickness while, in fact, no spacing lower by this distance was observed in the in situ TEM. Moreover, the yield equation was unable to describe the marked effects of grain boundaries. The most important drawback of this model, referring to Murakami[55], was the exclusion of line tension difference due to shear modulus dissimilarity.

Assuming the total density of dislocation was the sum of both *statically stored* and *geometrically necessary dislocations* that were responsible for additional stress, Ronay[51] developed a relationship for specifying a critical shear stress required to plastically deform a thin polycrystalline film on substrate. The model had included shear modulus and strain near surface.

$$\tau_Y = \tau_S + \frac{1}{\pi}\mu\left(\frac{b\gamma}{sl}\right)^{\frac{1}{2}} + m\mu\left(\frac{2b\gamma}{d}\right)^{\frac{1}{2}} \qquad \text{2-35}$$

where:

τ_S = increment of flow stress due to statically stored dislocations

γ = shear strain near the surface

s = a constant dependent on the orientation of primary slip system to the substrate

l = thickness of the film

m = Taylor orientation factor

d = grain diameter

The above equations had explained appropriately the unusual high yield stress of relatively soft thin film metals attached to rigid substrate as illustrated in Figure 2-6. It should be noticed that the relationship was only valid for a sufficiently low temperature in which the geometrically necessary dislocation arrays were assumed to be stable toward recovery. Moreover, Kuan and Murakami[54] suggested that it would be only suitable for the film thicker than 200nm since no geometrically necessary array of dislocations was observed below this thickness

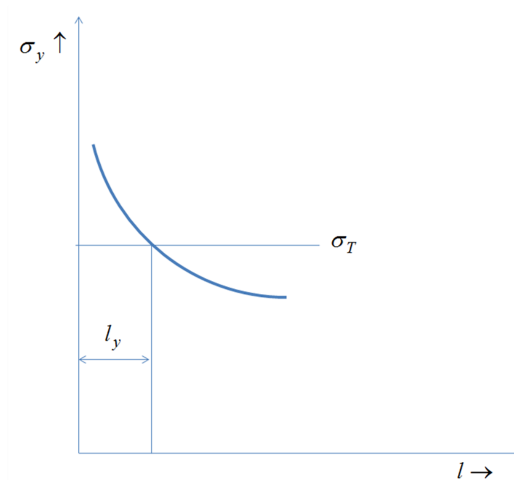

Figure 2-6 Schematic illustration of thickness-dependence of strength

(after ref.[51])

Another important concept established at confined dimension is the development of misfit dislocations at the film-substrate interface. Formation of misfit dislocations at the interface, its mechanism, criterion, and kinetics was comprehensively reviewed in ref.[58].

The concept provides a sound fundamental background to understand processes responsible for plastic deformation of thin films on rigid substrates.

Formation of misfit dislocations was explained in ref.[58]. Provided dislocations are there within the substrate, they will logically develop into epitaxial thin film before finally reach the free surface. The threading dislocation withstands force due to the lattice mismatch biaxial stress and glides in its slip plane. Since the dislocations located in the substrate were always constant in fraction, they would withstand less force in opposite direction. While stepping forward, the threading dislocation bows and leaves in its way a misfit dislocation. Figure 2-7 illustrates the development of misfit dislocations from threading dislocations. Quantitative treatment on the formation of this dislocation was revealed in ref.[56].

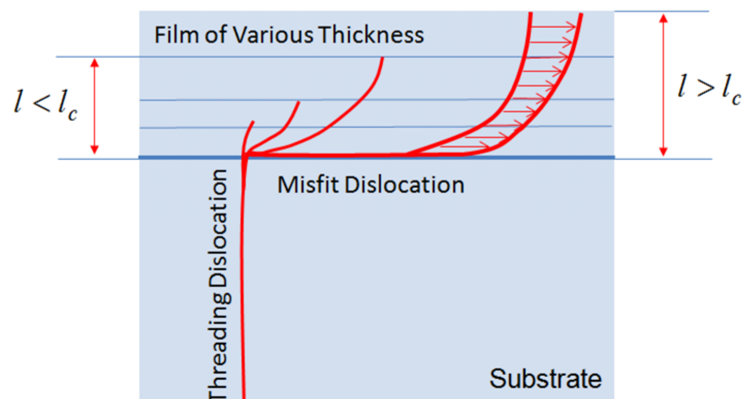

Figure 2-7 Bending of a threading dislocation in a strained film on a substrate

Note: above the critical thickness, the strain is sufficient to cause the dislocation to move (after ref.[58])

Applying the misfit dislocation model, following Freund[56], Nix[58] explained the mechanism of plastic deformation in thin films on substrates specifically the thickness-dependence of strength phenomena.

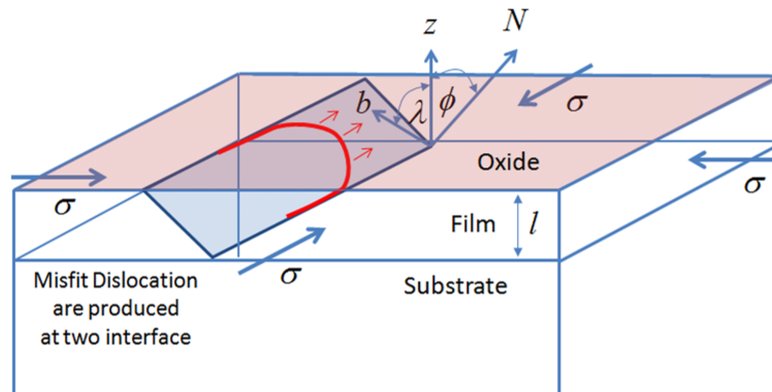

Figure 2-8 Dislocation motions in a film at confined dimension

(after ref.[58])

Referring to the geometry in Figure 2-8, work done by the biaxial stress while the dislocation stepping a unit distance forward can be written as:

$$W_{layer} = \frac{\cos\phi \cos\lambda}{\sin\phi}\sigma b l \qquad \text{2-36}$$

where:

subscript "layer" indicates the work done by the stress in the film

σ = biaxial stress in the film

b = Burger vector

l = thickness

The energies of the two dislocations left at near the interface can be expressed as:

$$W_{disl} = \frac{b^2}{4\pi(1-\upsilon)}\left[\frac{2\mu_f \mu_s}{(\mu_f + \mu_s)}\ln\left(\frac{\beta_s l}{b}\right) + \frac{2\mu_f \mu_c}{(\mu_f + \mu_c)}\ln\left(\frac{\beta_c t}{b}\right)\right] \quad 2\text{-}37$$

where:

μ_f, μ_s, μ_c = the elastic shear modulus of the film, substrate, and confinement respectively

l, t = thicknesses of film and confinement respectively

υ = Poisson's ratio

β = a numerical constant in the order of unity

The condition for moving dislocation is defined as:

$$W_{layer} \geq W_{disl} \quad 2\text{-}38$$

The minimum biaxial stress required to step the dislocation forward, therefore, can be obtained by simply equating Eq. 2-36 and Eq. 2-37.

$$\sigma_{crit} = \frac{\sin\phi}{\cos\phi\cos\lambda}\frac{b}{2\pi(1-\upsilon)l} \times \left[\frac{\mu_f \mu_s}{\mu_f + \mu_s}\ln\left(\frac{\beta_s l}{b}\right) + \frac{\mu_f \mu_c}{\mu_f + \mu_c}\ln\left(\frac{\beta_c t}{b}\right)\right] \quad 2\text{-}39$$

It can readily be seen from the expression, which has been derived for a single crystal thin film on substrate, that yield strength is dependent inversely on the thickness. The effect of confinement was accommodated by the second term in the bracket. The expression, however, did not involve the existence of any obstacles and friction stresses impeding the movement of dislocation.

It had been shown briefly in Figure 2-7 that there exists a critical thickness of film below which the strain is insufficient to move the dislocation. In simplest way, it can be said that the critical thickness evaluates the energy required to form a misfit dislocation with the energy of lattice mismatch released as it is formed. When the thickness is smaller than the critical thickness, the net driving force is negative, and hence a misfit

dislocation cannot be formed spontaneously. On the contrary, when the thickness is greater than the critical thickness, the net driving force is positive and thus it can be formed spontaneously[57]. Not only does the critical thickness have a technological application in designing dislocation-free device, it also provides a fundamental ground to understand the mechanism of plastic deformation in thin film.

Thermodynamically, the thickness was defined based on a general idea that a sufficient amount of energy is required to develop a unit length of misfit dislocation and this energy is supplied by the work done by dislocation as it moves a unit distance.

Critical thickness can be generally defined by applying an equilibrium theory[56].

$$\frac{l_c}{\ln\left(\frac{\beta l_c}{b}\right)} = \frac{\mu b}{4\pi(1-\upsilon)M\varepsilon} \qquad \text{2-40}$$

where:

$M\varepsilon$ = biaxial stress in the film

M = biaxial modulus

ε = biaxial elastic strain that must be imposed on the film to bring the lattice of the film into coincidence with that of the substrate

l_c = critical thickness

More exact form of Eq. 2-40 can be derived for a particular orientation. Nix[58], for example, had derived an exact solution for the case of FCC crystal with the (001) orientation focusing on dislocations movement on the octahedral {111} planes (See Figure 2-9). ϕ and λ define the angles specifying the {111} slip plane normal and Burger vector respectively. The derivation involved both edge and screw dislocation model. The result was expressed as:

$$\frac{l_c}{\ln\left(\frac{\beta l_c}{b}\right)} = 1.9 \frac{b}{4\pi(1-\upsilon)\sigma} \frac{2\mu_f \mu_s}{(\mu_f + \mu_s)} \qquad \text{2-41}$$

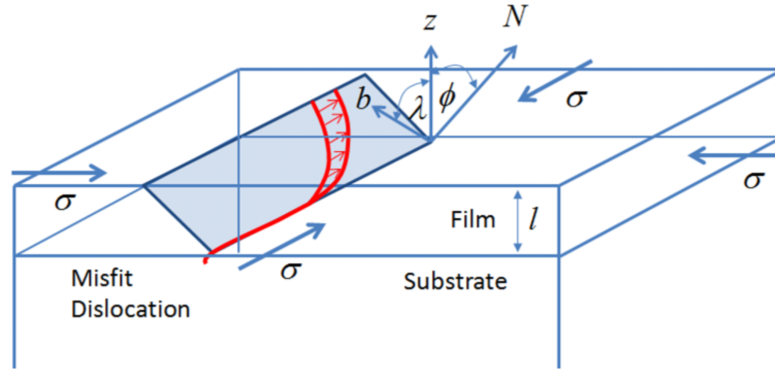

Figure 2-9 Illustration of misfit dislocation movement in thin film on substrates (after ref.[58])

Furthermore, Nix[59] developed simpler plasticity models for thin film by assuming a threading dislocation segment of a pure edge dislocation on a slip plane normal to the film plane and a pure screw misfit dislocation deposited behind its trial. The so called screw dislocation model was employed chiefly to make the interactions simpler in evaluating the effect of a single and multiple obstacle(s) as well as the effect of rigid passivation and substrate on the movement of dislocation and hence strengthening mechanism and strength.

Nix[59] employed a method of image to find the energy of a misfit dislocation by calculating the work required to step the true dislocation forward from very near surface to the interface. The interaction force between the dislocation and its image was involved in the calculation resulting in the following relations.

$$\tau_{channel} bl = W_{misfit} = \int_b^l f ds = l \int_b^l \frac{\mu b^2}{4\pi s} ds = \frac{\mu b^2}{4\pi} \log\left(\frac{l}{b}\right) \qquad \text{2-42}$$

$$\tau_0 = \frac{\mu b}{4\pi l}\log l \qquad 2\text{-}43$$

Eq. 2-43 was subsequently used as a reference value for the strengthening effects due to the effects of elastic modulus, confinement, and dislocation interactions. It was shown analytically that both confinements and obstacles had very significant roles in the mechanism of strengthening and strain hardening.

The effects of local barriers had been adopted in the model through the interaction of a dislocation line with single, dipole, and multiple dislocation obstacles as illustrated in Figure 2-10[59].

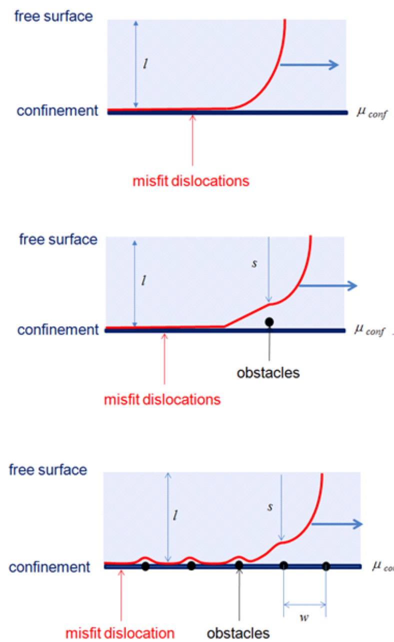

Figure 2-10 Schematic illustrations of a dislocation line passed through a film on substrate

(after ref.[59])

Nix's model, which assumed the interaction of a moving dislocation with equally spaced multiple obstacles, had very well explained the very high rates of strain hardening. Repelling misfit dislocations by the obstacles was assumed to give additional increase to the predicted value.

In addition to the dislocation line obstacles interactions, Kraft and Gao[86] had revealed two other scenarios for strain hardening. The possible scenarios involve the deposition of the interfacial dislocations of the channeling dislocations and the repeating emission of dislocation loop by the source located at the interior. They are all illustrated in Figure 2-11.

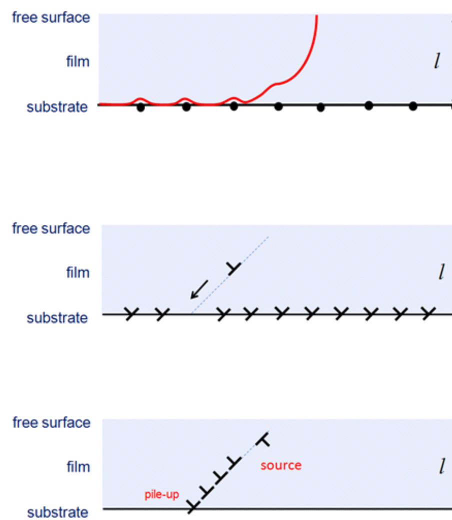

Figure 2-11 Schematic illustrations of possible dislocations configuration associated with strain hardening

(after ref.[86])

In summary, it is generally sound to assume that a threading dislocation will only step ahead when the motion releases a sufficient amount of energy to form a misfit dislocation. As a consequence, there exists a threshold (critical) stress related to the movement of dislocation. The critical stress varies with the reciprocal thickness of the film as represented by a general relationship. The presence of a confinement will require another dislocation to be created. On the other hand, obstacles may have already established at the interface, which may be left by the former moving dislocations. All together give raise in energy for dislocation glide, and hence the flow stress.

The above models were developed for the case of a single dislocation line in a single crystalline film involving interaction with other dislocations. Kraft et.al.[61] had pointed out that they were not necessarily applicable for polycrystalline films because of difference underlying assumptions. It was revealed that the steady state assumption of steady movement of threading might be halted by the grain boundary. Baker[85] assumed that the effect of grain boundary in thin film was similar to that in bulk materials except for the geometry. This boundary particularly hindered the threading dislocation from long-range movement. The fact that it happened in a very narrow channel provided a reasonable answer on why much higher stress level was achieved.

In fact, the reciprocal thickness-dependence of yield stress had been observed in a polycrystalline thin film metal at much higher stress level than that was predicted by the previous model. With respects to the earlier model, therefore, it was generally sound to assume that, if dislocations were constrained in an individual grain then a segment of dislocation had to be created at both the grain boundaries and the material interface. Thompson[87] had derived a relationship for polycrystalline thin films to describe the dependence of yield stress on reciprocal thickness and diameter of grain.

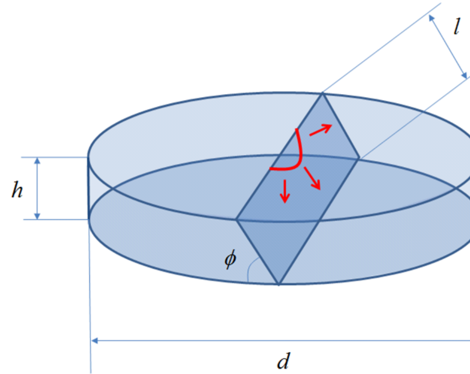

Figure 2-12 A cylindrical disc model of thin film grain

(after ref.[87])

A cylindrical disc of thickness h representing a single grain (Figure 2-12) was employed to derive a model equation for a polycrystalline thin film:

$$\sigma_y = \left(\frac{W_{dis}\sin\phi}{b\cos\lambda\cos\phi}\right)\left(\frac{2}{d\sin\phi}+\frac{1}{l}\right) \quad 2\text{-}44$$

where:

W_{dis} = energies per unit lengths of the respective dislocation segments

λ = the angle between Burger vector of the normal to the plane of slip

It can be seen that the model had explicitly included grain size strengthening in addition to the thickness and crystallographic orientation. Underestimation of stress was just as expected due to the failure in accommodating the interactions of dislocations[87].

The model of “dislocation line channeling” as well as “additional dislocations formation” and “pre-existing network of dislocations” at near confined surface had been proven by some results of in-situ TEM observations, with particular reference to the single crystal thin film on a single crystalline substrate.

From the observations of Pb thin film on substrate, it was previously revealed that the dislocation glide was confined in each grain by grain boundary and materials interfaces (surface oxide and substrate)[54]. One of the strong evidences was obtained from epitaxial Al on a single crystal substrate[88]. Similar facts was also reviewed in ref.[89] and even added in ref.[90]. Figure 2-13 presented an advanced threading dislocation with a dislocation segment left in its trial. Interaction between the channeling and interface dislocations was associated with the stand-off of the dislocation from the interface. Pre-existing networks of dislocations were observed at the interface as a consequence of film/substrate lattice mismatch. It was assumed that they effectively operated as the sources of new dislocations. Dehm et.al.[90] demonstrated the emission of dislocation half-loops from the interface during heating (Figure 2-14).

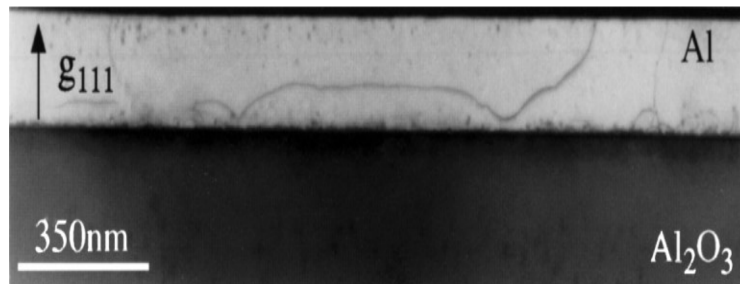

Figure 2-13 Cross-sectional TEM image of a 350nm thick epitaxial Al film deposited on a single crystal (0001) alpha-Al_20_3 substrate.

(after ref.[88])

Figure 2-14 Cross sectional TEM image of a 350nm thick epitaxial Al film deposited on a single crystal (0001) alpha-Al_2O_3 substrate during heating.

(after ref.[90])

The TEM images of both cross-sectional and plan-view observations were quite opposite in polycrystalline materials. In-situ cross-sectional observations of 450nm thick polycrystalline Cu film on Si substrate with an amorphous-SiN_x diffusion barrier during heating cycle (Figure 2-15), for example, did not show evidence of both the deposition of interfacial dislocation segments and the hindrance of dislocation by the interface[88]. It was also revealed that the interface acted as the sink for dislocations rather than the source that hindered the motion of dislocation. Plan-view observations demonstrated comparable results[88]. When the grain size was at the order of thickness, it was generally assumed that dislocation did not channel[86].

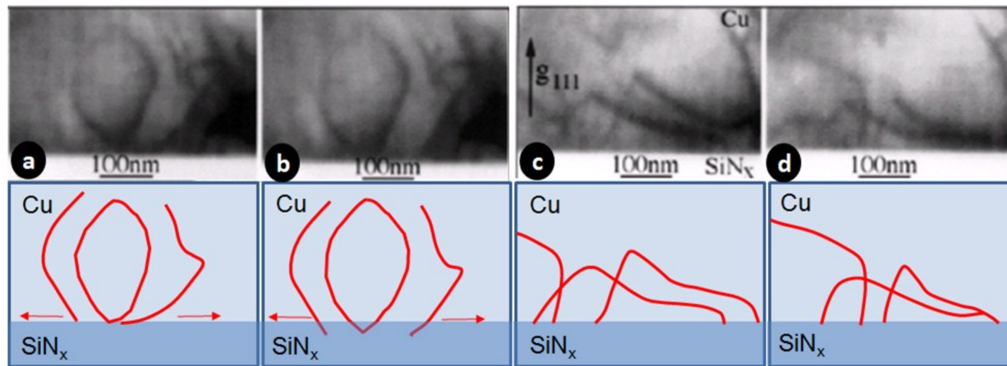

Figure 2-15 Dynamic cross sectional TEM images during heating cycle of a 450nm thick polycrystalline Cu on a Si substrate with a-SiNx diffusion barrier

(after ref.[88])

It was observed that dislocations slipped on a plane inclined to the interface had generated slip traces or dislocations lines at the interface[89]. The contrast of the slip traces in the TEM images, however, was particularly fading when they were irradiated below their threshold damage. The fading of the contrast in association with the strain field indicated the core spreading of the interfacial dislocation[89]. This spreading, which is schematically illustrated in Figure 2-16, is a characteristic phenomenon at the interface of crystalline/amorphous, at which the substrate has no simple crystallographic relation with the film and hence can be considered as continuum[86].

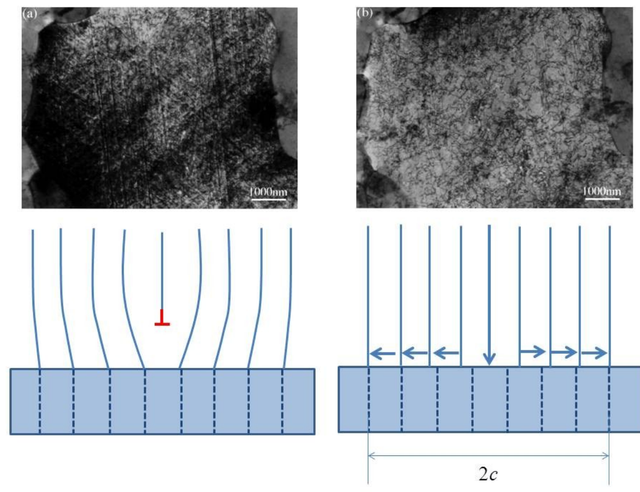

Figure 2-16 Schematic illustration of dislocation core spreading

(after ref.[89] and ref.[86])

It was believed that the metal film/amorphous interlayer interface pulled dislocations to the ground[91]. In general, the characteristics of the interface between film and substrate play very significant roles in determining dislocation glide in a thin film on substrate. When the interfacial bonding is sufficiently stiff to constrain dislocation segment from the escape, interfacial dislocation segments will be deposited. On the contrary, when the interfacial bonding is weak, interfacial dislocation segments hardly ever drag long segments of interfacial dislocations[92

The facts that dislocations behaved differently in polycrystalline had challenge the established assumptions and models of work hardening. One of the possible scenarios, as has been previously discussed, is to assume the “bulk-like” behavior of film, meaning that the flow stress is controlled by the pinning of internal dislocation whose density increase with the decrease of the thickness. On the other hand, it was also known that the number of events decreased with the decrease in thickness film[91].

To this point the effects of temperature had not been included except those through the temperature-dependence of elastic modulus. While the thin film is being subjected to the temperature change, different phenomena were observed (see Figure 2-17). In general, dislocations were longer and more mobile at elevated temperature. At lower temperature, dislocation tangles were assumed to be formed. While the dislocation is moving continuously at higher temperature, the motion was described as jerky at lower temperature.

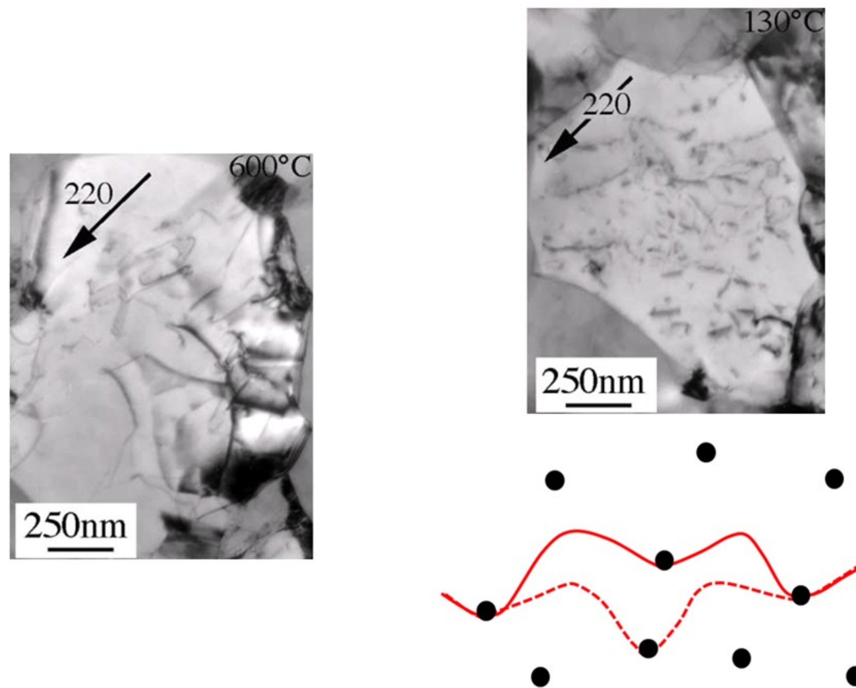

Figure 2-17 Plan-view TEM images of Cu grains at 600°C and 130°C

Longer and more mobile dislocation at higher temperature (left)

Dislocation tangles and jerky motion at lower temperature (right)

(after ref.[88])

The jerky motion represented the step by step discontinuous process of thermally-activated dislocation movement. At lower temperature, dislocations were pinned by obstacles, which are assumed as forest of dislocations. At most of the time, it was believed that dislocations did not mobile. At some point, a segment of dislocation were able overcome the obstacles and then rapidly swept through an area depending on the density of obstacle. Kobrinsky and Thompson[93] had identified this phenomena as a solid evidence for the thermally-activated motion of dislocations overcoming obstacles. This argument specifically refers to the fact that the segments of dislocations, whose lengths were comparable to the thickness, were not observed at low temperature ($T<150^{o}C$).

Moreover, Kobrinsky and Thompson[93] had also revealed an activation volume as a clear evidence of thermally-activated obstacles-controlled dislocation mechanism. Activation volume of FCC thin films, which had been reported smaller than the typical values for bulk corresponding metals, was reasonable in thermally-activated dislocation-mediated, obstacle-controlled mechanism. In the case of the diffusion-controlled creep mechanism, the expected value would be in the cubic order, at least one order of magnitude higher than the observed value. In general, the dominant mechanism of plasticity in thin film could be identified by the activation volume.

Based on the qualitative and quantitative evidence from TEM observations, Kobrinsky and Thompson[93] strongly believed that thermally-activated obstacle-controlled dislocation-mediated plasticity was the dominant flow mechanism in Ag thin film. The conclusion was expected to be preserved for FCC thin film, including Cu and Au.

Efforts have been done to apply the established concepts of thermodynamics and dislocation plasticity in thin film on substrate. Along with Kobrinsky and

Thompson[93], Flinn et.al.[2,7], Volkert et.al.[14], Witvrouw et.al.[15,22]. Proost et.al.[17], and Gruber et.al.[37] had tried to explain the temperature-dependence of stress phenomena in thin film on substrate by applying the theory of thermally-activated obstacles-controlled dislocation-mediated plasticity, which have been established in bulk metals.

Applying a simple model and a square approximate assumption (see Eq. 2-12 and Eq. 2-13) one can generally write:

$$\dot{\gamma}_P = \dot{\gamma}_0 \exp\left(\frac{-\Delta F}{kT}\right)\left\{1-\frac{\tau}{\hat{\tau}}\right\} \qquad \text{2-45}$$

From this well known relation, Flinn et.al.[7], had derived a critical stress for a given strain-rate and temperature:

$$\sigma = \hat{\sigma}\cdot\{1-T/T_F\} \qquad \text{2-46}$$

where:

$T_F = \Delta F \cdot \ln(\dot{\varepsilon}_P/\dot{\varepsilon}_0)/k$

= a (hypotethical) temperature at which the flow stress would go to zero.

ΔF = the Free energy required to overcome obstacles in the absence of applied stress.

From this fundamental equation Flinn et.al.[7] had derived a general relation for stress relaxation data of thin film on substrate. In this case, a total strain, which is the sum of elastic and plastic component, is generated by the difference of thermal expansion.

$$\varepsilon_T = \varepsilon_E + \varepsilon_P \qquad \text{2-47}$$

$$\varepsilon_T = \Delta\alpha \cdot \Delta T \qquad \text{2-48}$$

Heating and cooling a thin metal plate on substrate at some rate, it is sound to assume:

$$\dot{\varepsilon}_T = \dot{\varepsilon}_E + \dot{\varepsilon}_P \quad \text{2-49}$$

In the case of a thin plate (assuming strong (111) texture), the elastic component strain can be directly related to stress by:

$$\sigma = \varepsilon_E \cdot E/(1-\upsilon) \quad \text{2-50}$$

Re-writing Eq.2-45, differentiating Eq.2-50, and combining them, will result in:

$$\dot{\varepsilon}_T - \dot{\varepsilon}_E = \dot{\varepsilon}_0 \exp\left(\frac{-\Delta F}{kT}\right)\left\{1-\frac{\sigma}{\hat{\sigma}}\right\} \quad \text{2-51}$$

$$\dot{\sigma} = \dot{\varepsilon}_E \cdot E/(1-\upsilon) \quad \text{2-52}$$

Combining Eq.2-51 and Eq. 2-52 yields:

$$-\dot{\sigma} = [E/(1-\upsilon)] \cdot \dot{\varepsilon}_0 \exp\left(\frac{-\Delta F}{kT}\right)\left\{1-\frac{\sigma}{\hat{\sigma}}\right\} \quad \text{2-53}$$

Integration of the equation results in a general stress-time relationship:

$$\sigma = B\{\ln(B/R) - \ln[t + (B/R) \cdot \exp(-\sigma_0/B)]\} \quad \text{2-54}$$

where:

$B = kT\hat{\sigma}/\Delta F$

$R = [E/(1-\upsilon)] \cdot \dot{\varepsilon}_0 \cdot \exp(-\Delta F/kT)$

σ_0 = initial stress

Although the relationship was derived for Aluminum thin film on substrate, Flinn[2] revealed that the model could be employed for Copper thin film with minor modification.

Volkert et.al.[14] also derived a comparable equation for Al thin film:

$$\sigma = \frac{-kT\hat{\sigma}}{\Delta F} \ln\left[\exp\left(\frac{-\Delta F\sigma_0}{kT\sigma}\right) + A' e^{\Delta F/kT} \frac{\Delta F}{kT\hat{\sigma}} t\right] \quad \text{2-55}$$

Similar relationship had also been derived and used by Proost et.al.[17] and Witvrow et.al.[15,22] for Al-based alloy thin film:

$$\sigma = \frac{-kT}{a} \ln\left[\exp\left(\frac{-a\sigma_0}{kT} \right) + \frac{ac}{kT} t \right] \qquad \text{2-56}$$

where:

$$a = \Delta F / \left(\sqrt{3} \hat{\sigma} \right)$$
$$c = \left[\left(\dot{\gamma}_0 / 2\sqrt{3} \right) \left(E / (1 - \upsilon) \right) \right] \exp\left(-\Delta F / kT \right)$$

The above equations have been used to describe the isothermal stress relaxation of thin film on substrate. Moreover, it can also be used to characterize a film as well as to predict stress[7]. The fact that the relationship was able to describe the relationship had also confirmed that the ruling mechanism at low temperature and high stress was dislocation glide overcoming obstacles.

Volkert[14], assumed that the behavior of Al thin film could be appropriately described by the same parameter used in bulk Al. Fits of data had indicated that the possible contribution of other mechanisms was only below 5%. At higher temperature Volkert[14] suggested dislocation climb and diffusion mechanism with the transition region in between glide-controlled and climb-controlled region to play more important roles. At lower stress, it was reasonable to assume that dislocation could not move easily and hence diffusion was more significant.

Minor alloyment has added some complications associated with precipitation and grain growth[15]. The number of atoms in precipitate and misfit parameter of the (semi) coherent precipitates with respect to the matrix influenced the threshold stress. The kinetics of dislocation might also affected by its structure and distribution.

The threshold stress might be quantitatively correlated to obstacles spacing and dislocation density[37].

Study on polycrystalline Au thin films had revealed low and constant value of total obstacles energy[37]. The reasons for these phenomena involved the condition of surface and the change of deformation mechanism from full to partial dislocations. Similar phenomena were reported to be found in both single crystalline Au and polycrystalline Cu. The evidences supported the assumption of thermally-activated dislocation slip.

Assuming the correlation between the threshold stress and either obstacle spacing or dislocation density, however, the strong size effects cannot be explained clearly. To deal with it, Gruber et.al.[37] proposed another mechanism contributed to the effects. They assumed that the combined thickness and temperature-dependence of strength might come from the activation of impeded dislocation source followed by the thermal activation of dislocation glide. Moreover, Gruber et.al.[37] revealed that thermally-activated could not appropriately explain the strong temperature-dependence of the yield stress in Au films on polyimide. To deal with it, they adopted the mechanism of diffusional creep and derived a constitutive equation accordingly. This quantitative approach however was rather speculative since no observable evidences of diffusional creep were available.

It has been briefly discussed that at higher temperature, other mechanisms may come to appear together with obstacle-controlled dislocation glide. Thouless et.al.[13] agreed that at some point it might be oversimplified to rely on a single dominant mechanism while describing stress vs. temperature behavior. Mechanisms described by Frost and Ashby[52,94-97] had been employed to analyze the behavior of Copper thin film on Si substrate. Quite similarly, Koike et.al.[21] had employed deformation map to

analyze the ruling mechanisms in Aluminum alloy thin film on Si substrate subjected to thermal cycling. A straight forward approach was proposed assuming that the creep properties can be described by those established in bulk. Assuming a steady state condition, (1) a-thermal and thermally-activated yield, (2) power law creep, (3) grain boundary diffusion creep, and (4) lattice diffusion creep mechanisms were assumed to come into play.

Thouless et.al.[13] proposed important modifications in the diffusion-controlled regimes with regards to grain boundary and lattice diffusion mechanisms, in which symmetrical stress assumptions were typically employed in the model. Since mass transport phenomena in thin film should occur between the grain boundaries and the free surface rather than between two neighboring grain boundaries, the Coble and Nabarro-Herring equation should be slightly modified. The modified equation for plastic deformation rate involved (1) grain boundary diffusion as well as (2) additional path between the surface and grain boundary. No modification was suggested in the obstacle-controlled dislocation glide regime as well as lattice diffusion and core diffusion controlled climb regime. From the analysis of a Cu thin film on Si wafer[13] it was concluded that thermally-activated dislocation motion overcoming obstacles was dominant mechanism at intermediate temperature. Grain boundary diffusion was dominant at higher temperature ($>0.4T_{hom}$) whereas lattice diffusion could be neglected. A-thermal dislocation glide mechanism was assumed to occur only at the lowest temperature regime and highest stress.

Vinci et.al.[16] had modified slightly the plastic strain rate equations developed by Thouless et.al.[13] on the basis of Ashby Frost deformation map. Vinci et.al.[16,99] had revealed that the lack of dependency of the equations on the internal-state variables is due the simplifying assumption of steady state deformation in which the internal variable

were determined by the external variable of stress and temperature. They suggested that the assumption was only valid at high temperature in bulk material and might not be true at all for a material at confined dimension, with particular reference at very small strain over the temperature and heating rate related to the most common applications.

Keller et.al.[18,23] developed a mechanism-based interpretation of the stress-temperature behavior of unpassivated thin Copper film which could accommodate film thickness effect. Two modifications have been made. The first modification involved the variation of dislocation densities, activation energies, and stress exponent. The second one included the effect of limited interfacial diffusion on the creep mechanism governed by grain boundary diffusion. Important conclusions had been drawn. Firstly, grain boundary diffusional creep was assumed to be totally inactive. Secondly, power law creep mechanism seemed to be dominated. It was also noticed that the steady state condition might not be applicable in thin film and the micro-mechanism of dislocations might substantially differed from that in bulk.

Prior to the efforts to apply and modify the creep equations in thin film on substrates, Brotzen et.al.[98] had studied the creep behavior of free-standing metallic thin films commercially used in electronic packaging industries. Creep data were obtained from a specially designed creep experiment. Activation energies for secondary creep in thin films were reported to vary substantially from those in bulk corresponding materials. The phenomena were assumed to relate with the small grain size of metallizations. The exponential stress relation was more recommended to describe the results within the temperature and stress of interest rather than the stress power expression. Furthermore, activation volume and dislocation density were able to be evaluated from the creep curve.

Chapter 3

Method

General Procedure and Approach

General procedure for physical modeling of materials is summarized in Figure 3-1[63].

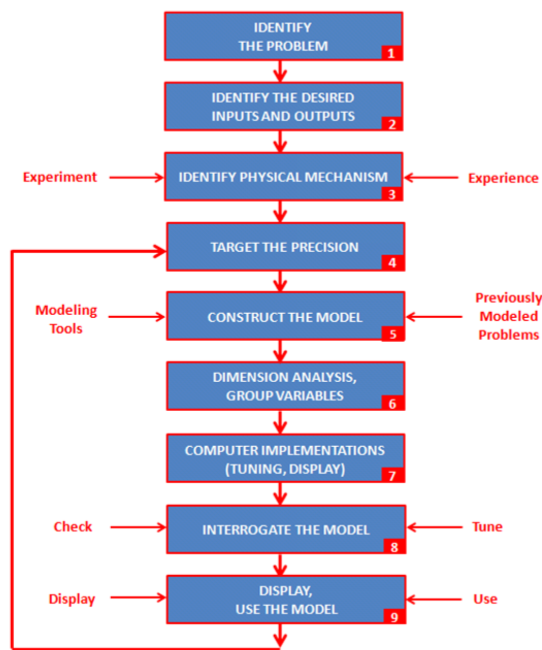

Figure 3-1 General flow chart for physical modeling of material (after ref.[63])

An approach called *model-inspired phenomenology*[64,65] is adopted in the study. Firstly, simple physically sound mathematical models are developed from the established principles. Secondly, the models are fitted into published experimental data in order to evaluate them and retrieve key parameters.

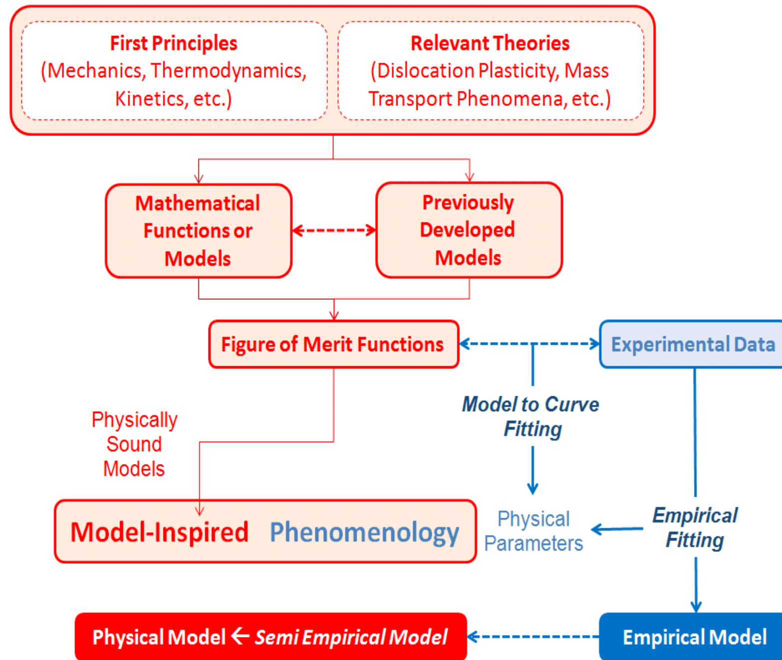

Figure 3-2 Model-inspired phenomenology approach

Assumptions

Based on the previous works related to the intended applications, the problem is limited in the range of temperature and strain rate when diffusion is neither existence nor significant. Within the scope, it is assumed that the temperature-dependence of flow stress is, as a rule, dictated by the flow kinetics of dislocations overcoming obstacles.

Model Descriptions

The physical-mechanistic foundation of the model was derived from Eq. 2-20.

$$\sigma(T) = A + B \cdot C(\dot{\varepsilon}, T) \quad (3\text{-}1)$$

where:

A = a constant parameter related to the a-thermal mechanism of dislocation movement

B = a constant parameter related to the internal state parameter

$C(\dot{\varepsilon},T)$ = an Arrhenius type parameter related to the thermal activation of dislocation movement.

First figure-of-merit function (Proposed Model I) is a simple linear function of *x'*, where *x'* is a reciprocal of *x*:

$$f(x) = a + bx' \qquad 3\text{-}2$$

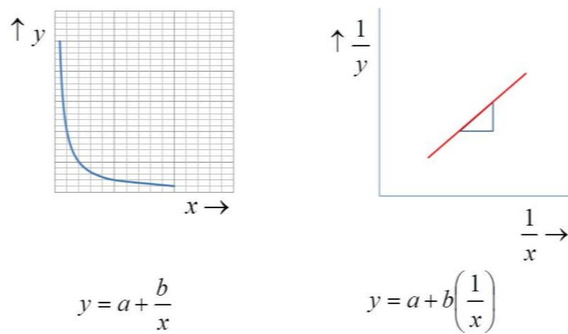

Figure 3-3 Proposed model I

Second merit function (Proposed Model II) is a first degree inverse polynomial (hyperbola) function:

$$f(x) = \frac{x}{ax+b} \qquad 3\text{-}3$$

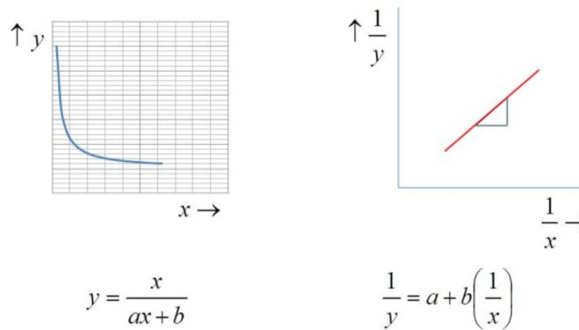

Figure 3-4 Proposed model II

Third merit function (Proposed Model III) is inspired by a function commonly used to describe such temperature-dependence physical properties as Arrhenius equation[100] and Clausius-Clapeyron equation[101].

The model is expressed in a type III exponential function.

$$f(x) = \exp\left(a - \frac{b}{x}\right) \quad \text{3-4}$$

Linearization of the function produces a log-reciprocal function.

$$\ln f(x) = a - \frac{b}{x} \quad \text{3-5}$$

The reverse version of the function was known as Schumacher's equation[102]

$$f(x) = \exp\left(a + \frac{b}{x}\right) \text{ or } \ln f(x) = a + \frac{b}{x} \quad \text{3-6}$$

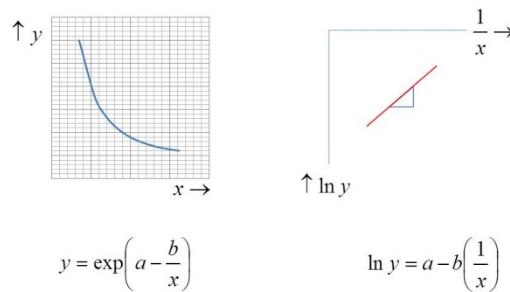

Figure 3-5 Proposed model III

Data Collection and Preparation

Data are collected and selected from the published literatures listed in Table 1-1.

Normalization of the data with relevant physical properties (Table 3-1) was performed in advance to reveal the real variables and allow fair direct comparison.

Table 3-1 Data for materials[97]

Data for Pure Metals	Melting Temperature	Shear Modulus at 300K $\mu x10^{-11}$ (dyn/cm2)	T-dependence of Shear Modulus (1/m)(dμ/dt) x 10^4 (/K)
Aluminum	933	2.54	5.4
Copper	1356	4.21	3.97
Gold	1336	2.48	3.18

Linearization of non-linear models was performed to allow the analysis of parameters. Analysis of parameters is performed by the least square method. Essentially, it is one of the statistical approaches which measures a probability distribution of hypothesis based on the Bayes' theorem that relates the conditional probabilities of two items.

Analysis

A figure-of-merit function with the highest probability will be estimated through a linear method described in this section.

Linear curve $y = a + bx$ is fitted into sets of data points (x_i, y_i). The best fitting curve has the least square error[103].

$$\Pi = \sum_{i=1}^{n}(y_i - f(x_i))^2 = \sum_{i=1}^{n}(y_i - (a + bx_i))^2 = \min \qquad 3\text{-}7$$

where:

x_i, y_i are all given and a, b are unknown coefficients.

Least square error is obtained when the unknown coefficients give rise to first derivatives zero[103].

$$\frac{\partial \Pi}{\partial a} = 2\sum_{i=1}^{n}\left(y_i - \left(a + bx_i\right)\right) = 0$$

$$\frac{\partial \Pi}{\partial b} = 2\sum_{i=1}^{n}\left(y_i - \left(a + bx_i\right)\right) = 0 \qquad \text{3-8}$$

$$\sum_{i=1}^{n} y_i = a\sum_{i=1}^{n} 1 + b\sum_{i=1}^{n} x_i$$

$$\sum_{i=1}^{n} x_i y_i = a\sum_{i=1}^{n} x_i + b\sum_{i=1}^{n} x_i^2 \qquad \text{3-9}$$

Eq. 3-9 can be solved simultaneously to obtain parameter a and b (Eq. 3-10)

$$a = \frac{\left(\sum_{i=1}^{n} y\right)\left(\sum_{i=1}^{n} x^2\right) - \left(\sum_{i=1}^{n} y\right)\left(\sum_{i=1}^{n} xy\right)}{n\sum_{i=1}^{n} x^2 - \left(\sum_{i=1}^{n} x\right)}$$

$$b = \frac{n\sum_{i=1}^{n} xy - \left(\sum_{i=1}^{n} x\right)\left(\sum_{i=1}^{n} y\right)}{\sum_{i=1}^{n} x^2 - \left(\sum_{i=1}^{n} x\right)^2} \qquad \text{3-10}$$

Alternatively, Eq. 3-8 can be solved using a matrix operation.

$$\left(\mathbf{A}^{\mathbf{T}}\mathbf{A}\right)X = \begin{bmatrix} 1 & 1 & 1 & \dots & 1 \\ x_1 & x_2 & x_3 & \dots & x_n \end{bmatrix} \begin{bmatrix} 1 & x_1 \\ 1 & x_2 \\ 1 & x_3 \\ \vdots & \vdots \\ 1 & x_n \end{bmatrix} \begin{bmatrix} a \\ b \end{bmatrix} \qquad \text{3-11}$$

$$\mathbf{A}^{\mathbf{T}}\mathbf{b} = \begin{bmatrix} 1 & 1 & 1 & \dots & 1 \\ x_1 & x_2 & x_3 & \dots & x_n \end{bmatrix} \begin{bmatrix} y_1 \\ y_2 \\ y_3 \\ \vdots \\ y_n \end{bmatrix} \qquad \text{3-12}$$

The least square equations (Eq. 3-9) can be represented by:

$$\left(\mathbf{A}^{\mathbf{T}}\mathbf{A}\right)\mathbf{X} = \mathbf{A}^{\mathbf{T}}\mathbf{b} \qquad \text{3-13}$$

Along with the best-value of *fit parameters*, *fit statistics* are assessed including: (1) standard error of y-estimate, (2) correlation index (coefficient of determination), (3) standard error of coefficients, (4) F-statistics, (5) number of degree of freedom, and (6) sum of squares of the regression and residuals.

Standard error of y-estimate is calculated by:

$$S_{y.x} = \sqrt{\frac{\sum_{i=1}^{n}(y_i - y(x_i))^2}{df}} \qquad 3\text{-}14$$

where:

$df = n - 2$

The standard error is used to specify *confidence limit* about the y-estimate curve.

Correlation index, r, can be calculated by:

$$r = \frac{\sum_{i=1}^{n} w_i(x_i - \bar{x})(y_i - \bar{y})}{\left[\sum_{i=1}^{n} w_i(x_i - \bar{x})^2\right]^{\frac{1}{2}}\left[\sum_{i=1}^{n} w_i(y_i - \bar{y})^2\right]^{\frac{1}{2}}} \qquad 3\text{-}15$$

Coefficient of determination (*r-squared*) is calculated by:

$$r^2 = 1 - \frac{\sum_{i=1}^{n} w_i(y_i - y(x_i))^2}{\sum_{i=1}^{n} w_i(y_i - \bar{y})^2} \qquad 3\text{-}16$$

where:

$$\bar{y} = \frac{\sum_{i=1}^{n} y_i}{n}$$

Standard errors of coefficients (intercept a and slope b) are calculated by:

$$se(b)=\sqrt{\frac{\sum_{i=1}^{n} w_i\left(y_i-(a+bx_i)\right)^2}{n-2}}\frac{1}{\sqrt{\sum_{i=1}^{n} w_i\left(x_i-\bar{x}\right)^2}} \qquad \text{3-17}$$

$$se(a)=\sqrt{\frac{\sum_{i=1}^{n} w_i\left(y_i-(a+bx_i)\right)^2}{n-2}}\sqrt{\left(\frac{1}{\sum_{i=1}^{n} w_i}+\frac{\bar{x}^2}{\sum_{i=1}^{n} w_i\left(x_i-\bar{x}\right)^2}\right)} \qquad \text{3-18}$$

$(1-\alpha)\times 100\%$ *confidence limit* for the mean y is defined by:

$$y=bx\pm t\left(\frac{\alpha}{2},n-2\right)\sqrt{\frac{\sum_{i=1}^{n} w_i\left(y_i-(a+bx_i)\right)^2}{n-2}}\sqrt{\frac{1}{\sum_{i=1}^{n} w_i}+\frac{\left(x-\bar{x}\right)^2}{\sum_{i=1}^{n} w_i\left(x_i-\bar{x}\right)^2}} \qquad \text{3-19}$$

Non-linear regression analysis are performed for three or more parameters model. Levenberg-Marquardt iteration algorithm is applied in the fitting process. Global and independent fit are used as necessary.

Chapter 4

Results

Normalized data of temperature-dependence of flow stress in bulk and thin film metals from Table 1-1 are plotted in Figure 4-1, 4-2, and 4-3 corresponding to proposed model I, II, and III respectively.

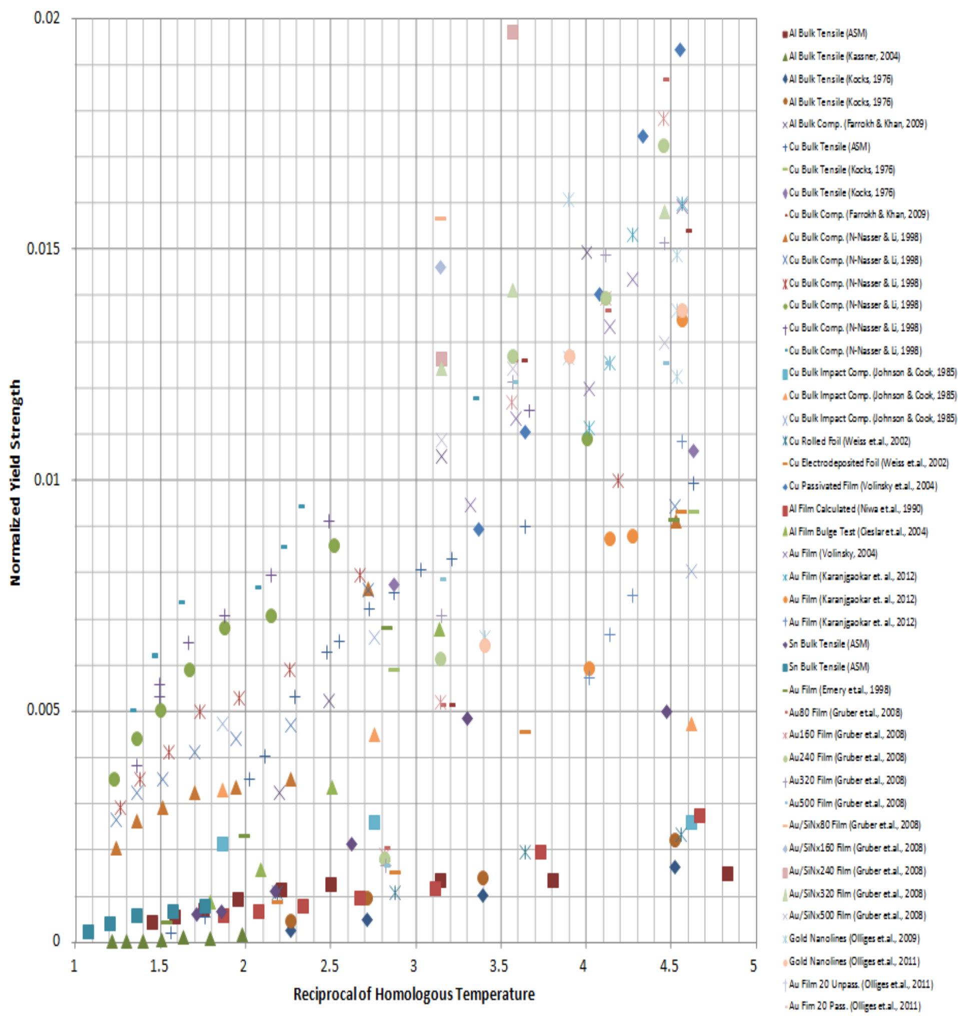

Figure 4-1 Data plot corresponding to proposed model I

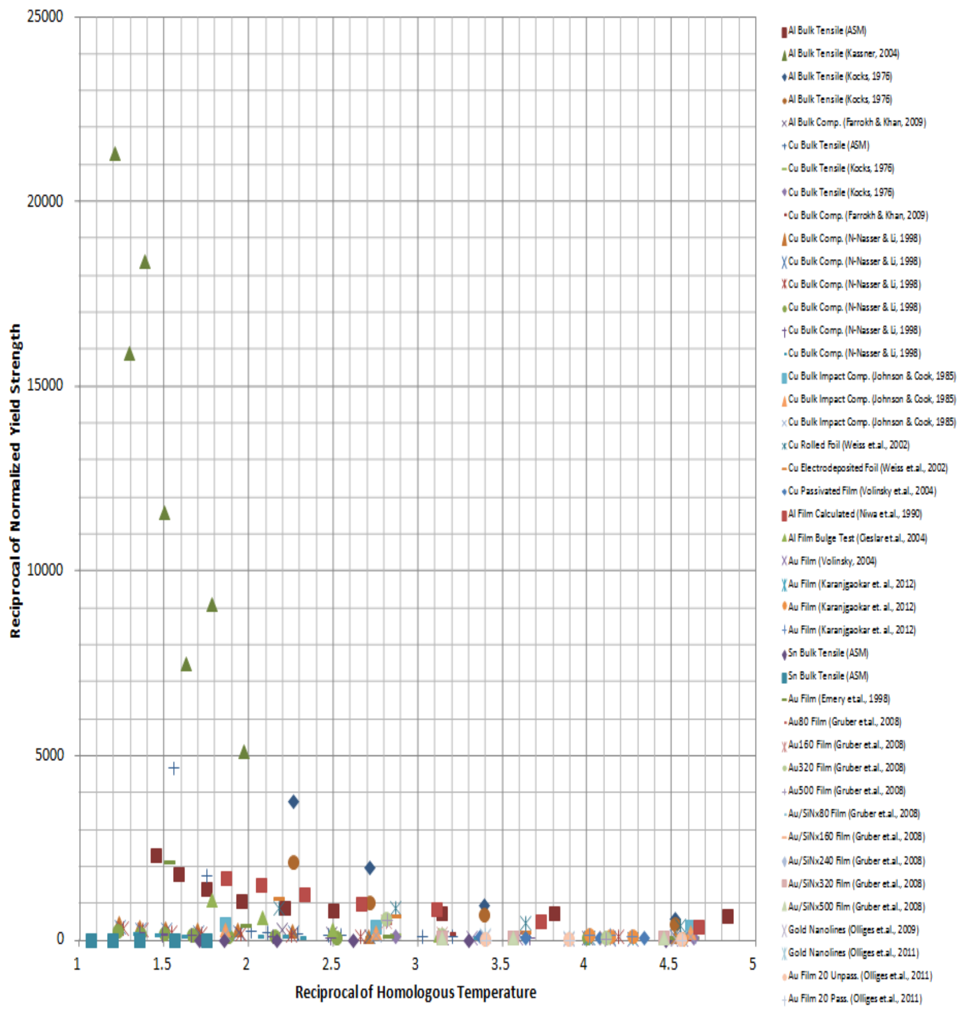

Figure 4-2 Data plot corresponding to proposed model II

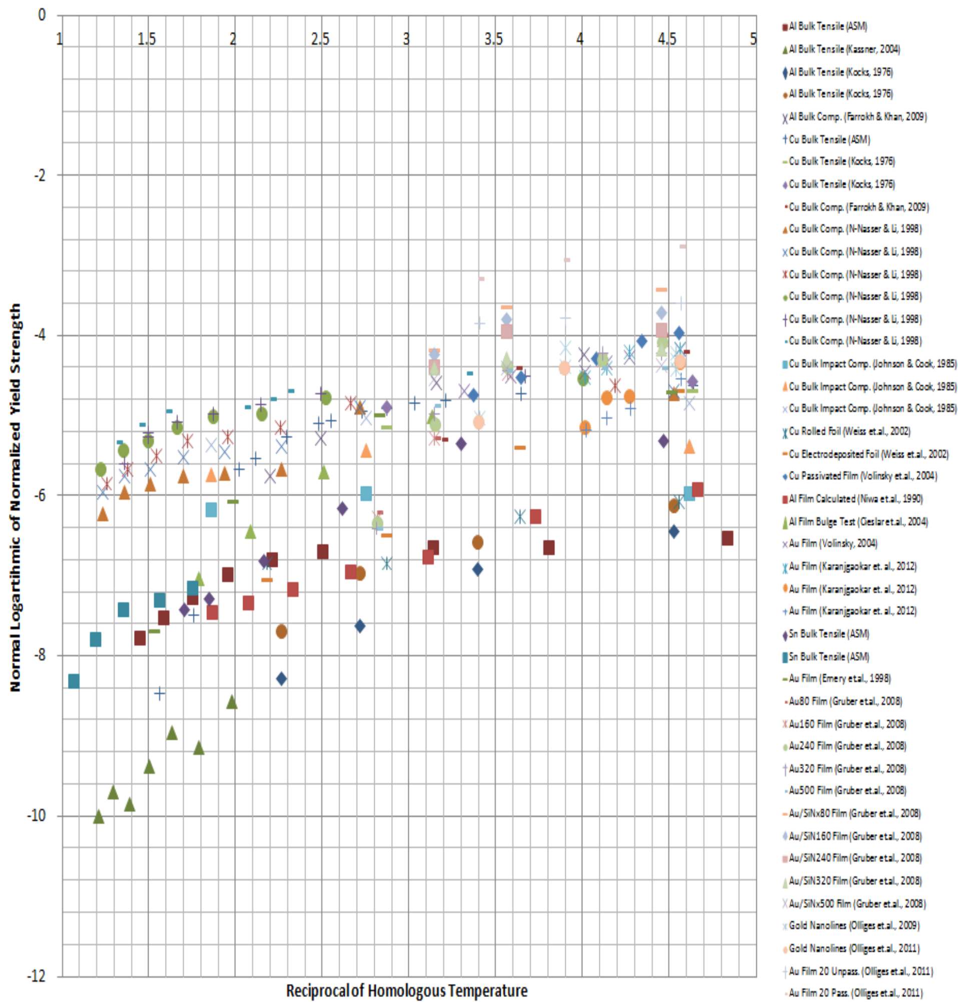

Figure 4-3 Data plot corresponding to proposed model III

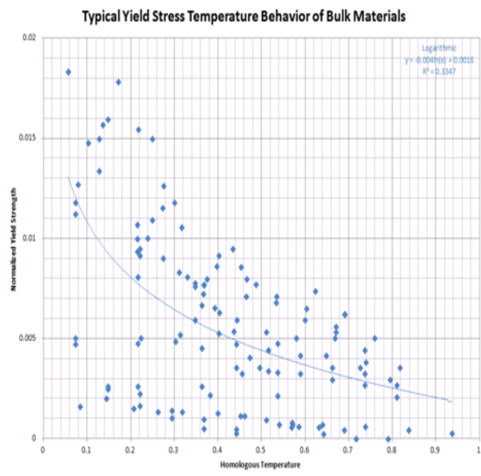

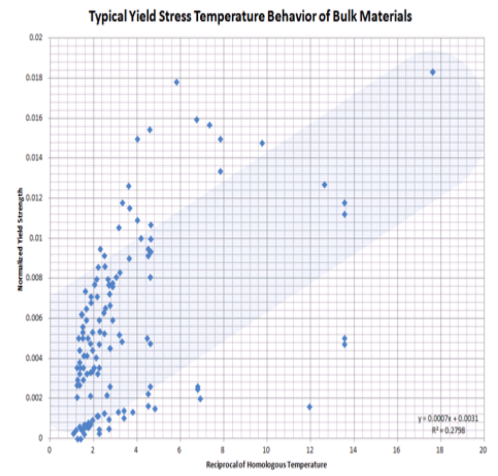

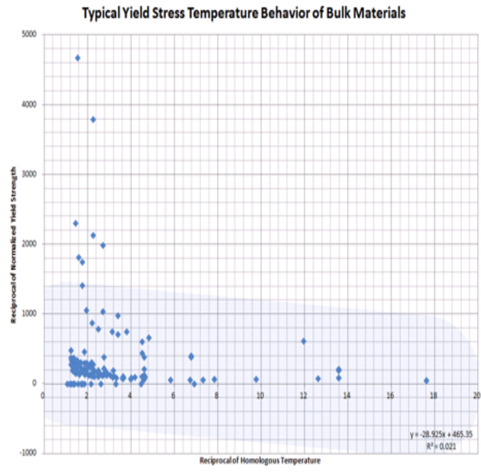

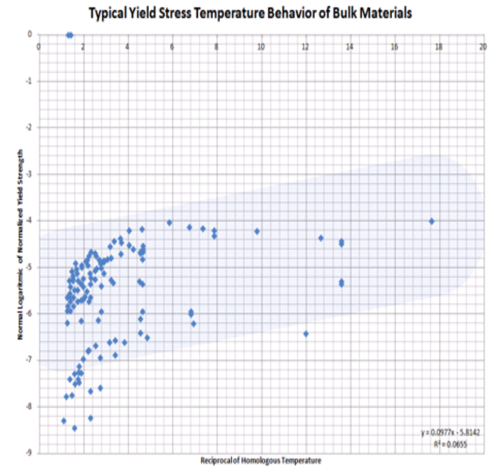

Figure 4-4 Preliminary analysis of bulk materials

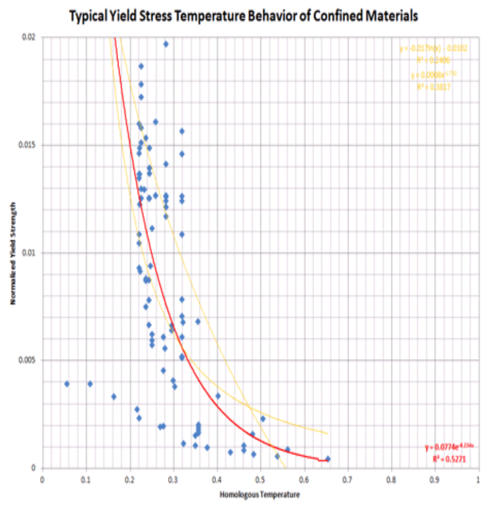

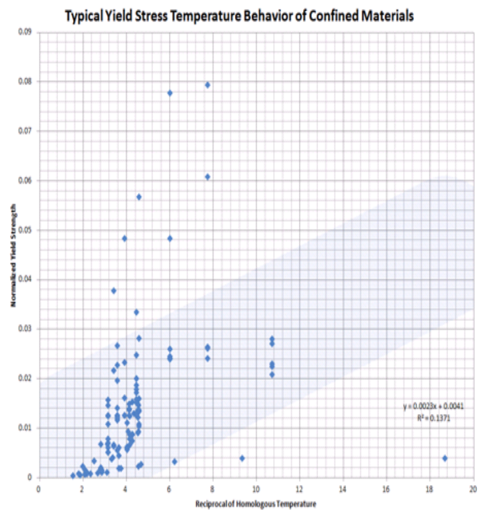

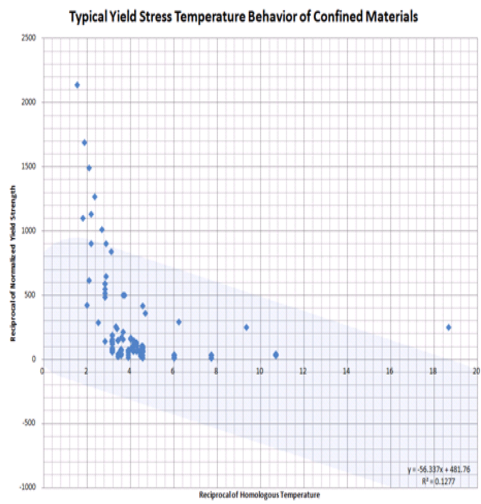

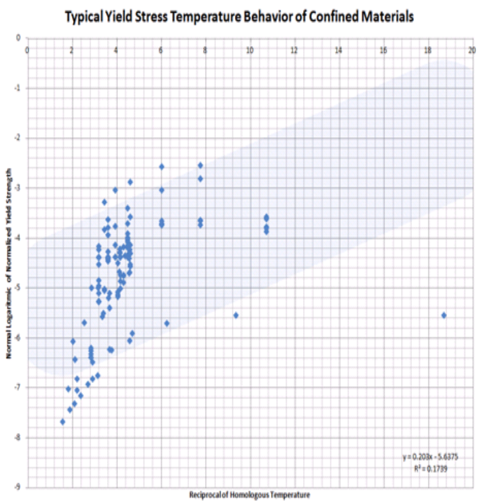

Figure 4-5 Preliminary analysis of confined materials

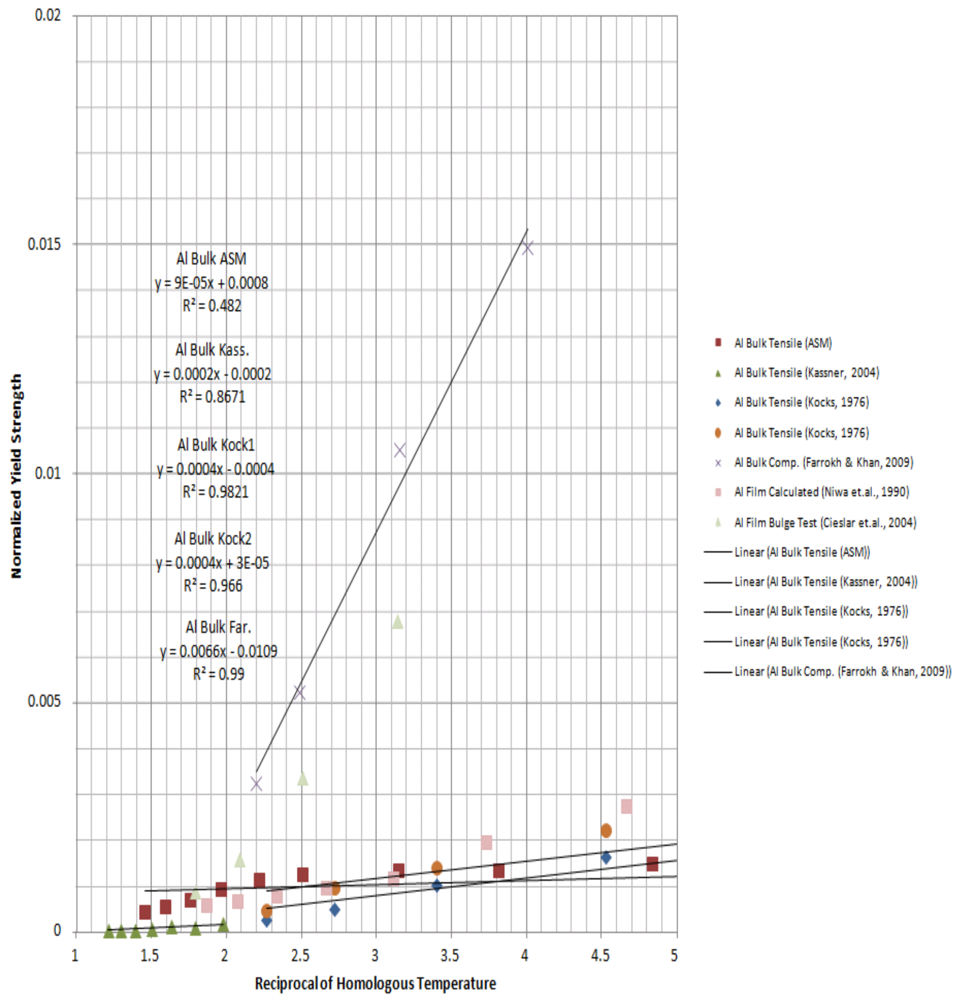

Figure 4-6 Linear plot of Al bulk materials corresponding to proposed model I

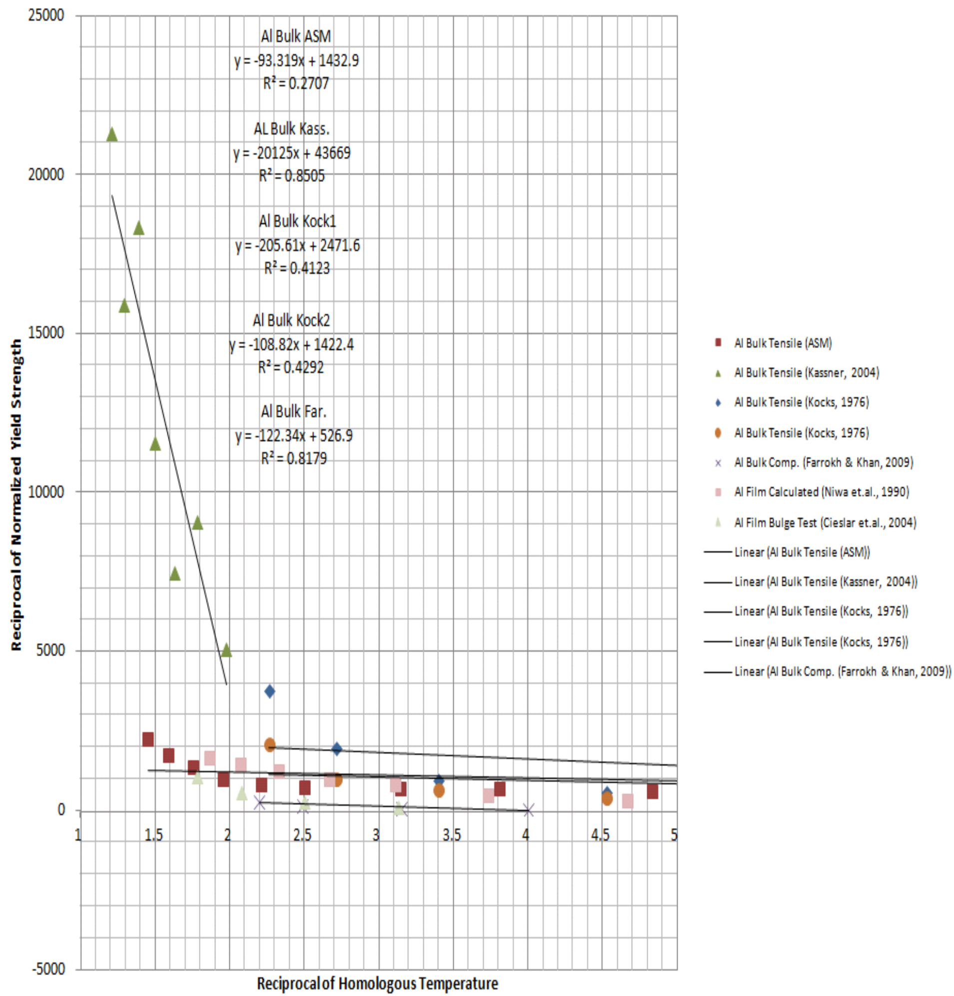

Figure 4-7 Linear plot of Al bulk materials corresponding to proposed model II

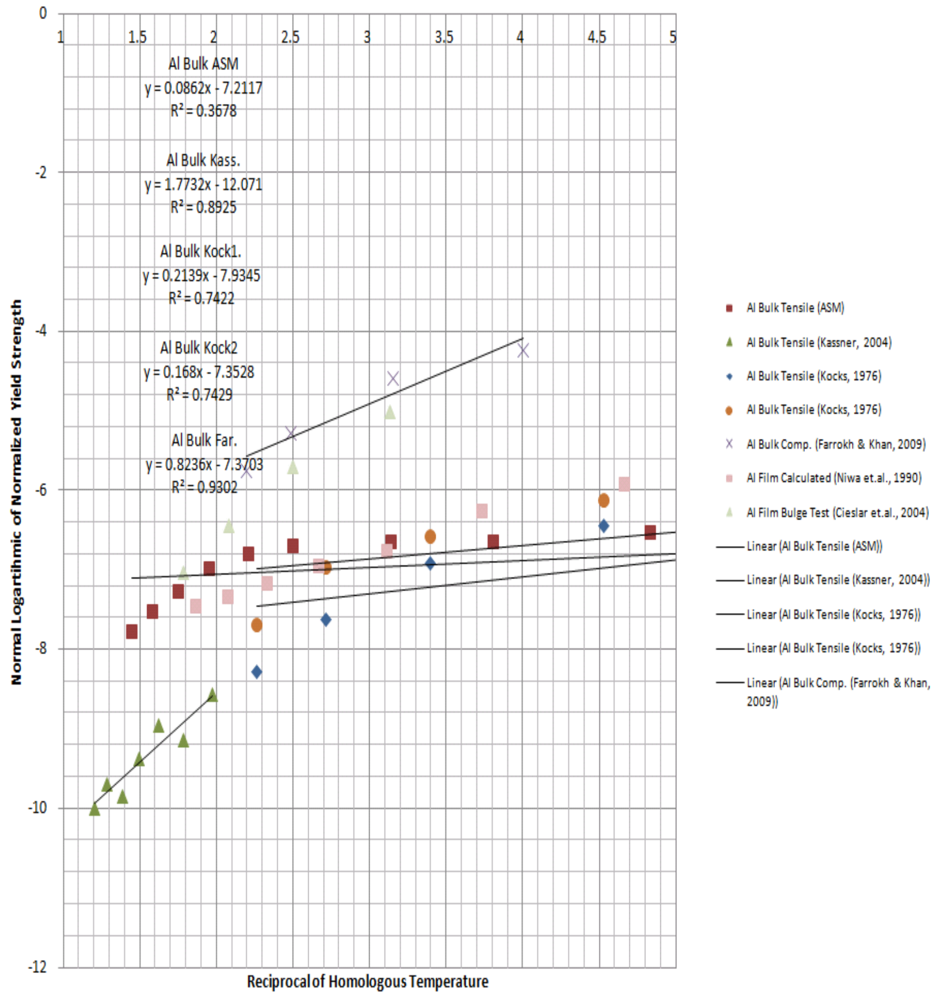

Figure 4-8 Linear plot of Al bulk materials corresponding to proposed model III

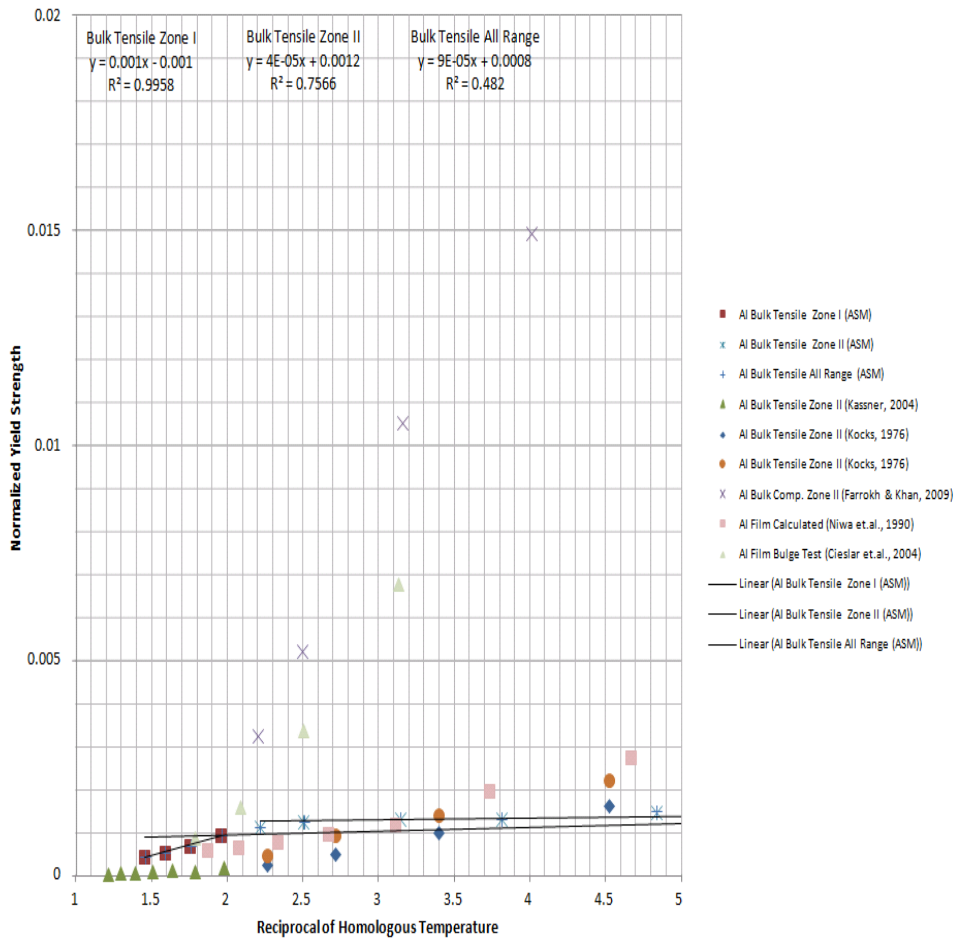

Figure 4-9 Linear plot of Al bulk materials in Zone I and Zone II corresponding to proposed model I

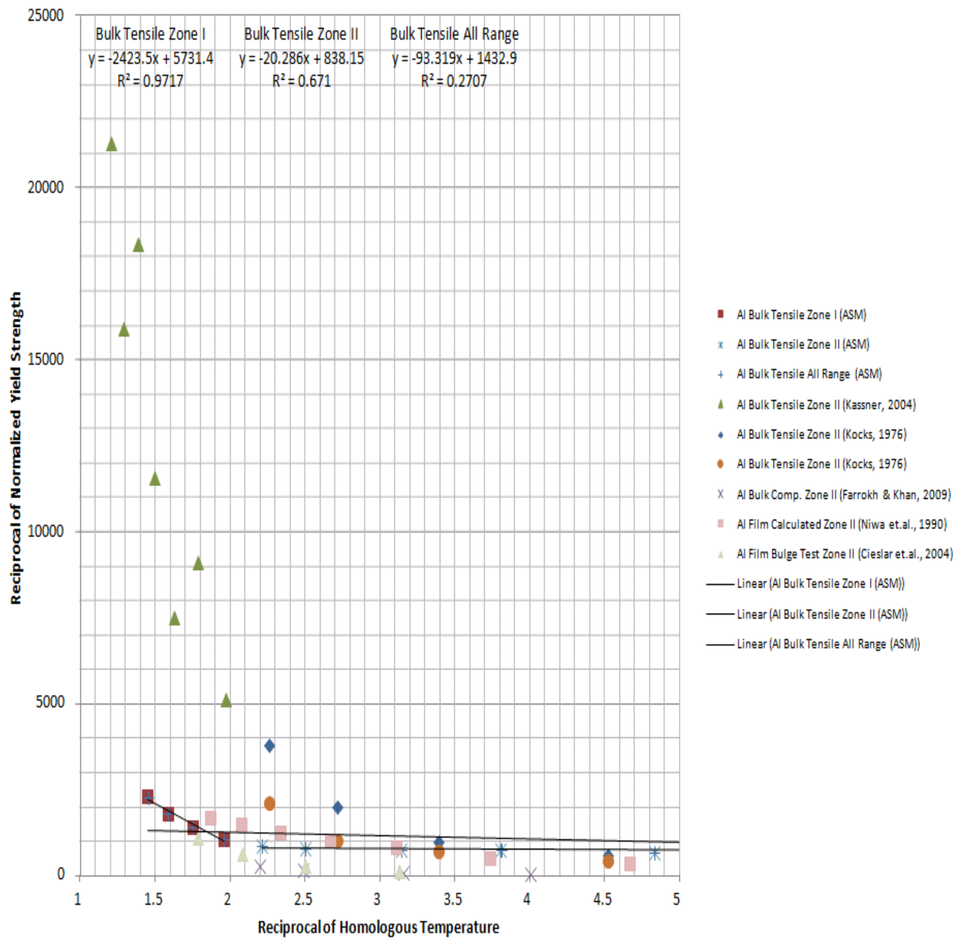

Figure 4-10 Linear plot of Al bulk materials in Zone I and Zone II corresponding to proposed model II

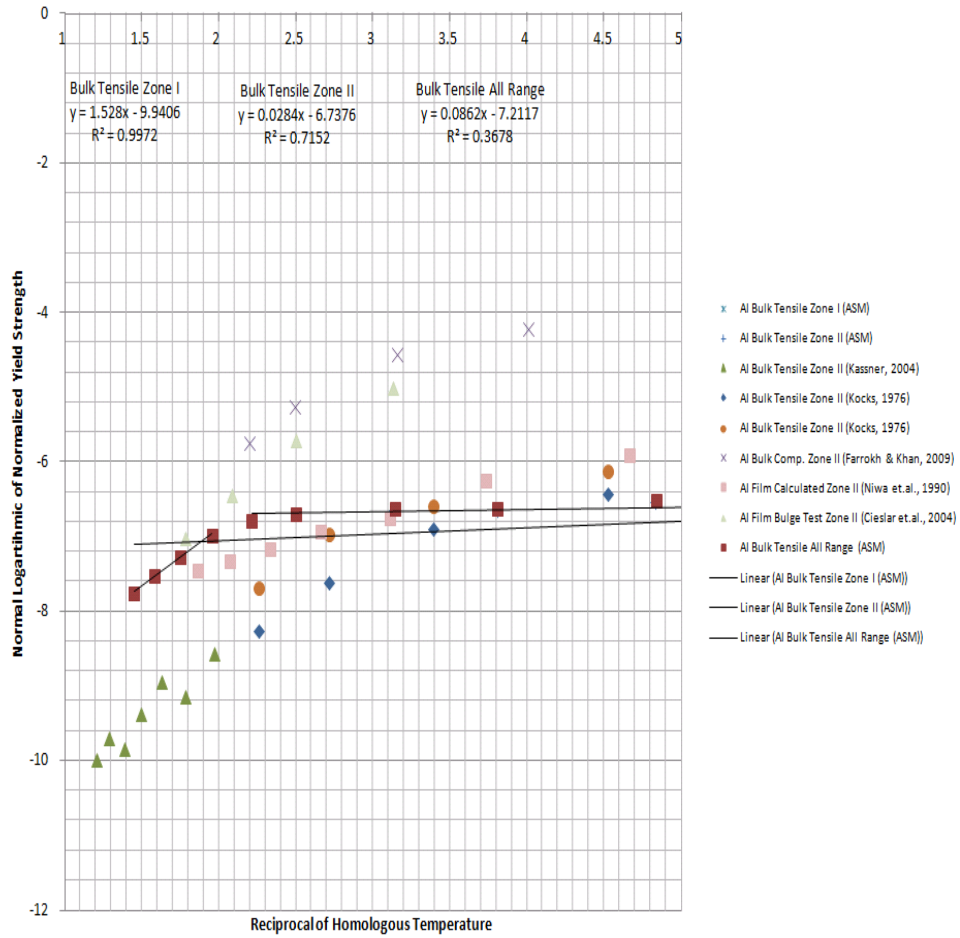

Figure 4-11 Linear plot of Al bulk materials in Zone I and Zone II corresponding to proposed model III

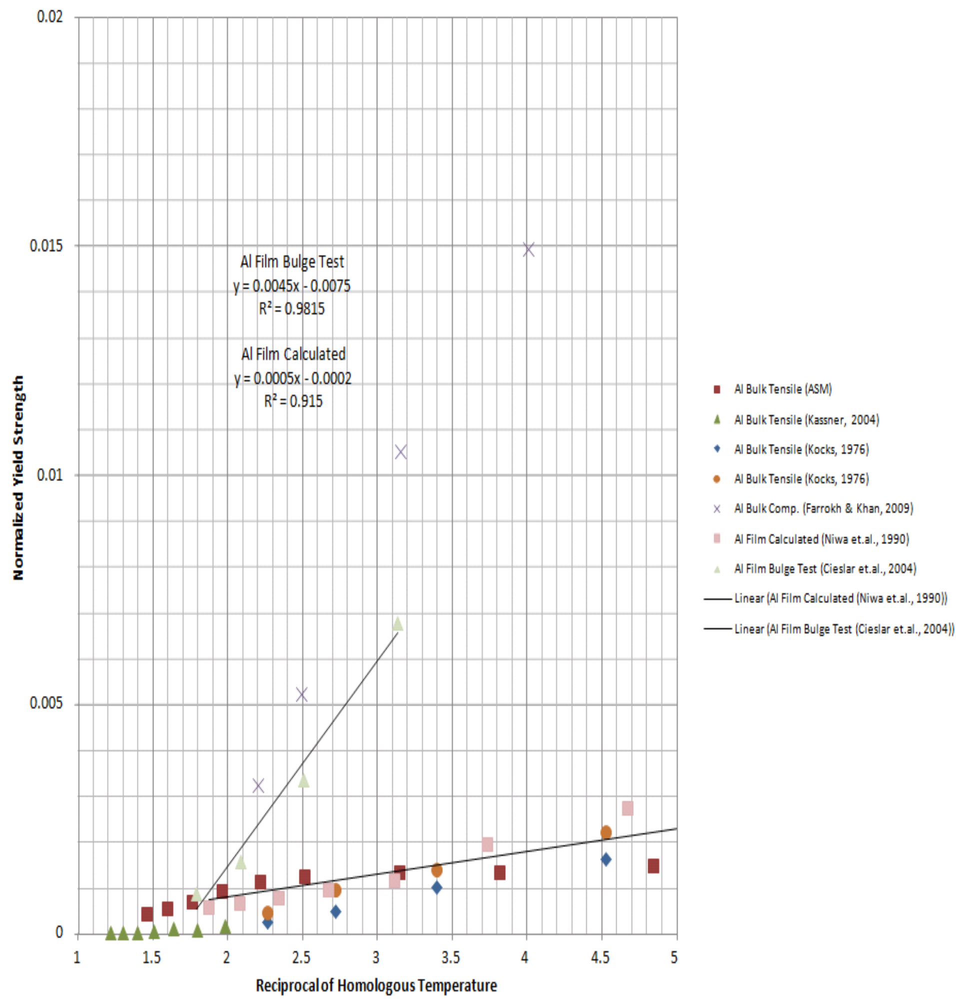

Figure 4-12 Linear plot of Al confined materials corresponding to proposed model I

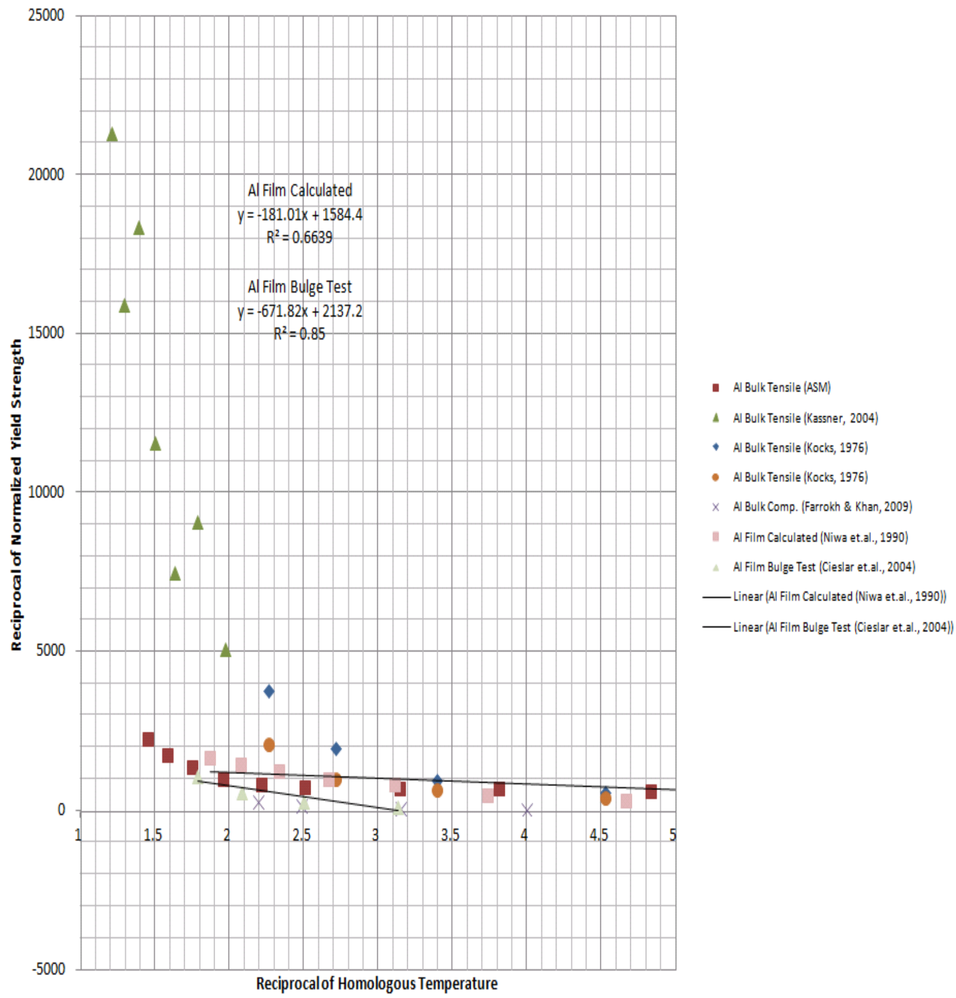

Figure 4-13 Linear plot of Al confined materials corresponding to proposed model II

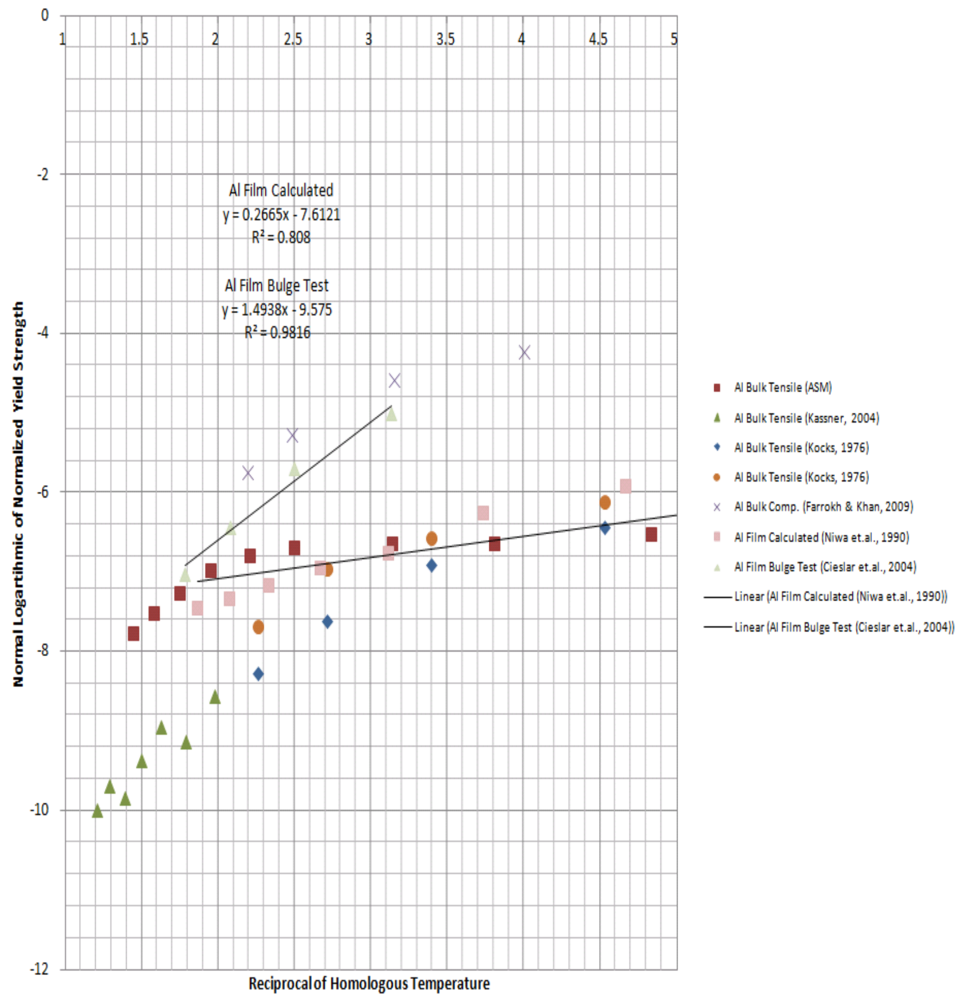

Figure 4-14 Linear plot of Al confined materials corresponding to proposed model III

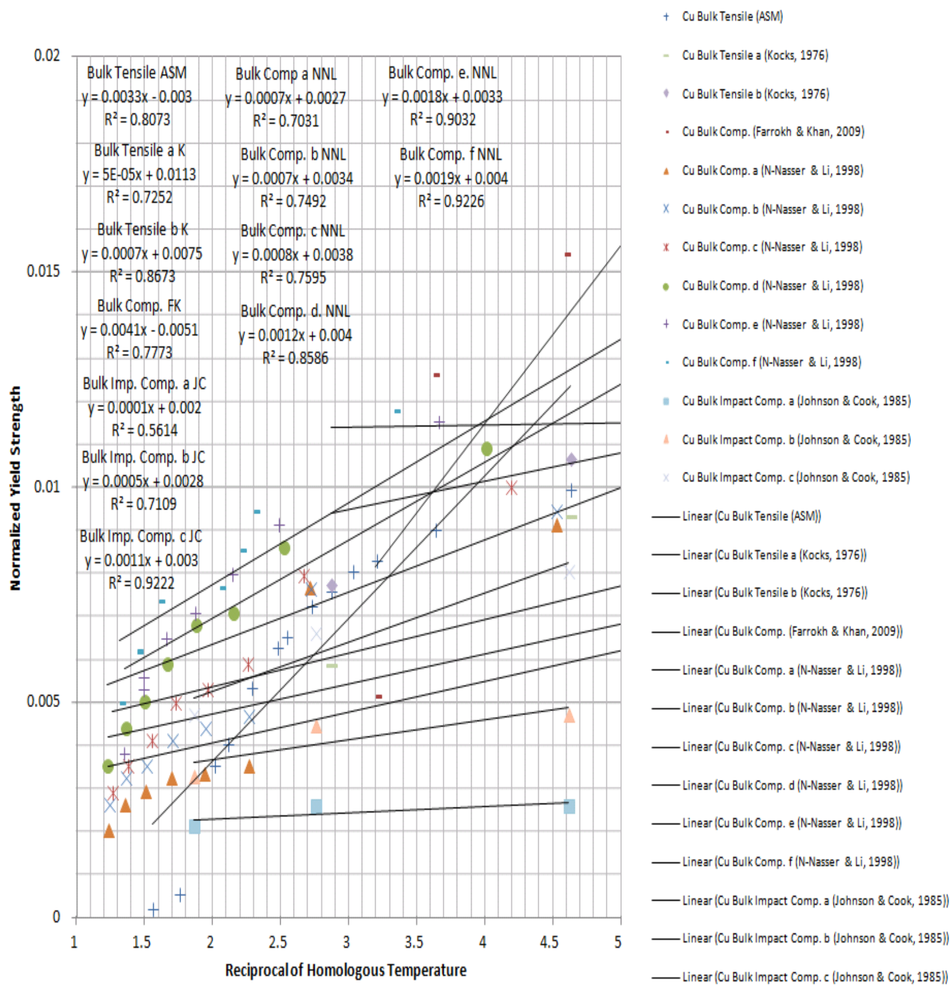

Figure 4-15 Linear plot of Cu bulk materials corresponding to proposed model I

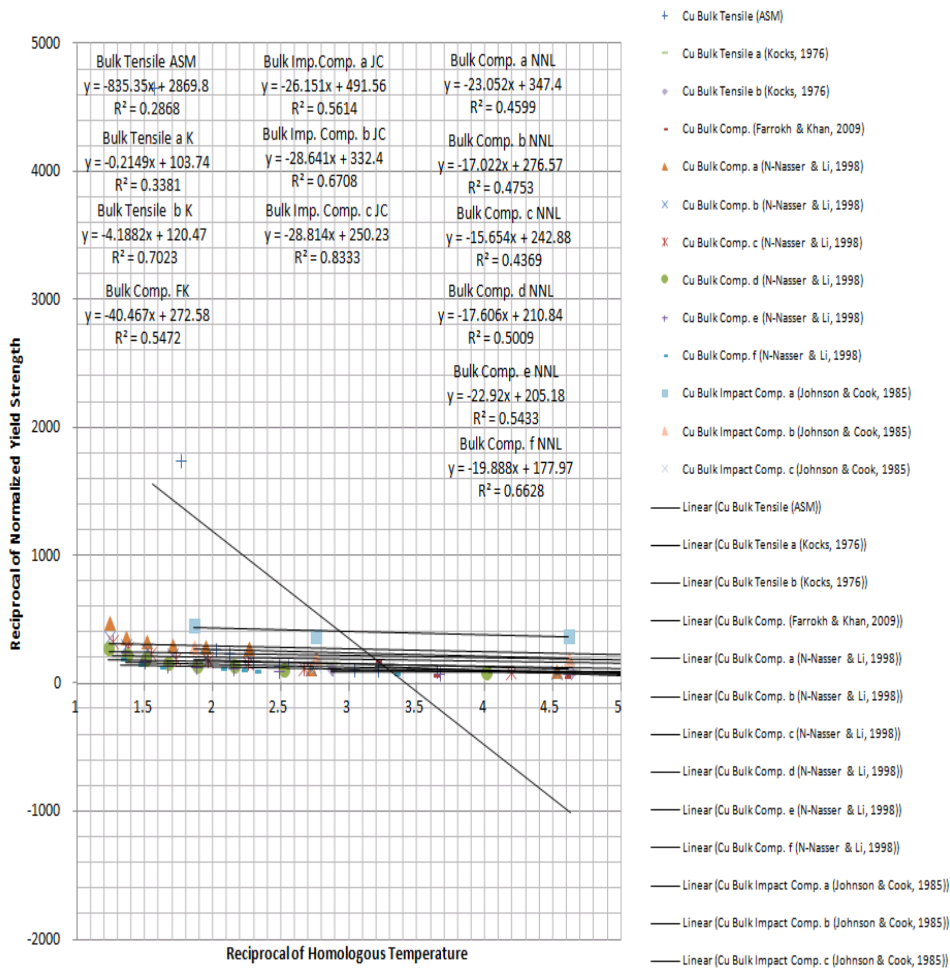

Figure 4-16 Linear plot of Cu bulk materials corresponding to proposed model II

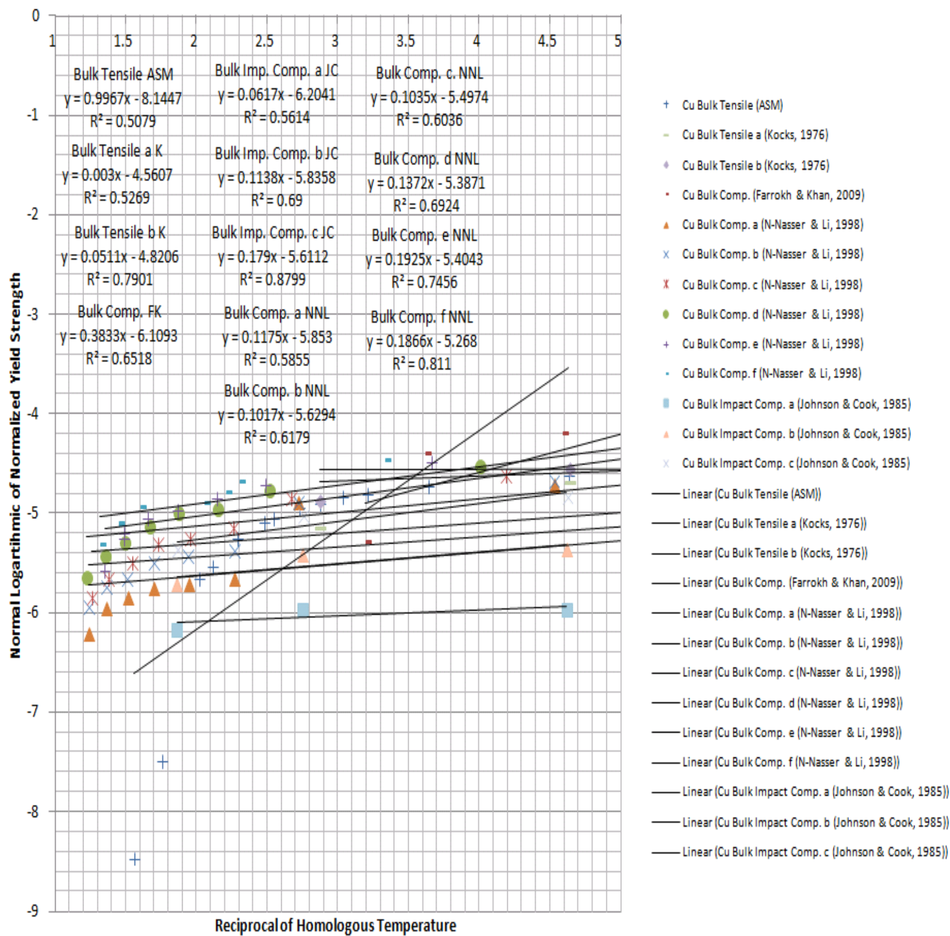

Figure 4-17 Linear plot of Cu bulk materials corresponding to proposed model III

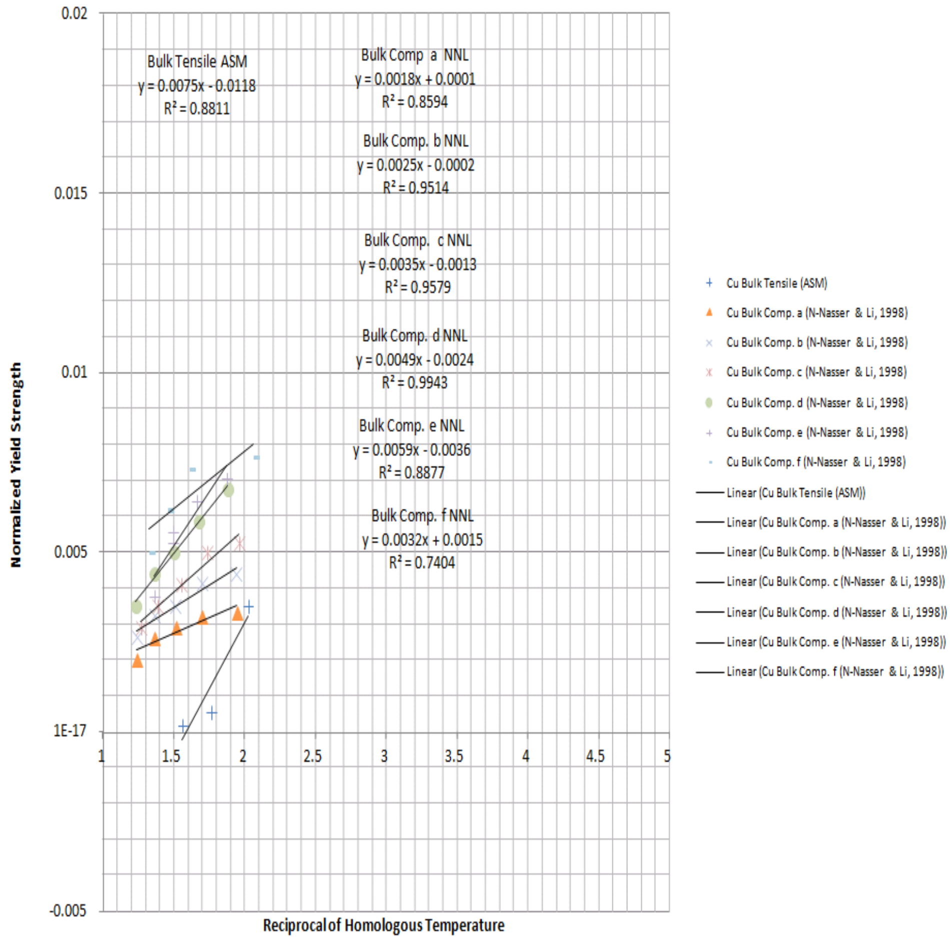

Figure 4-18 Linear plot of Cu bulk materials in Zone I corresponding to proposed model I

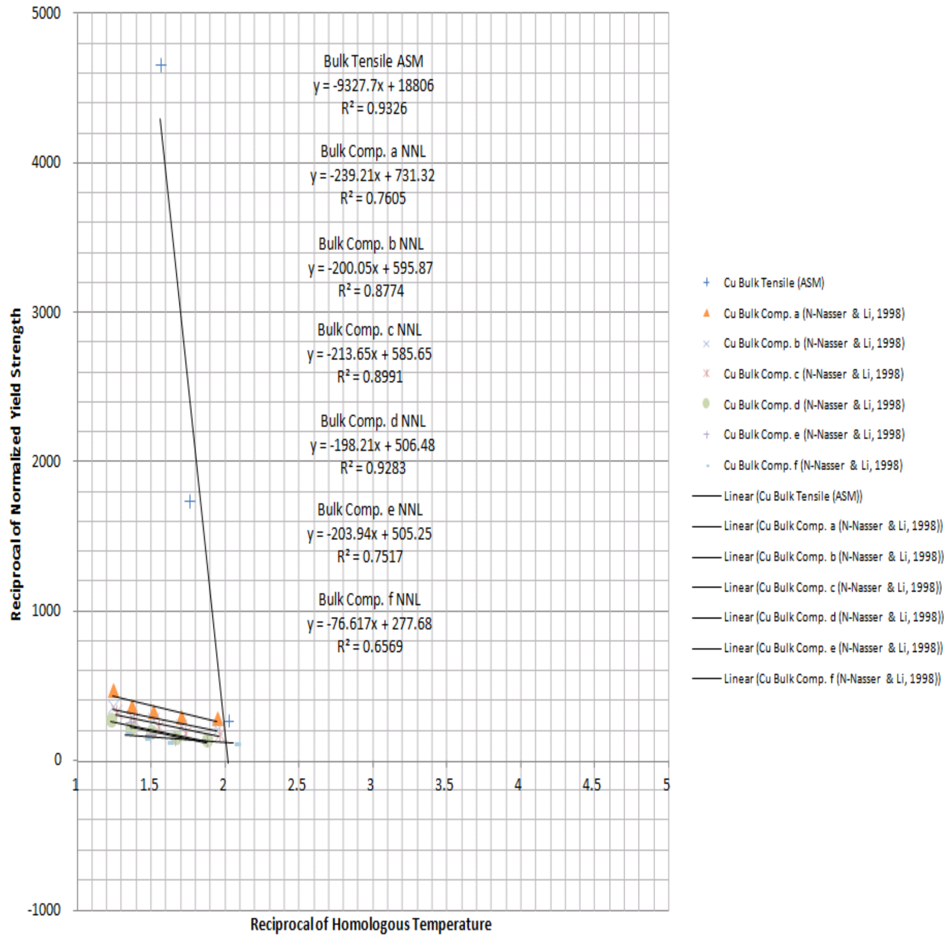

Figure 4-19 Linear plot of Cu bulk materials in Zone I corresponding to proposed model II

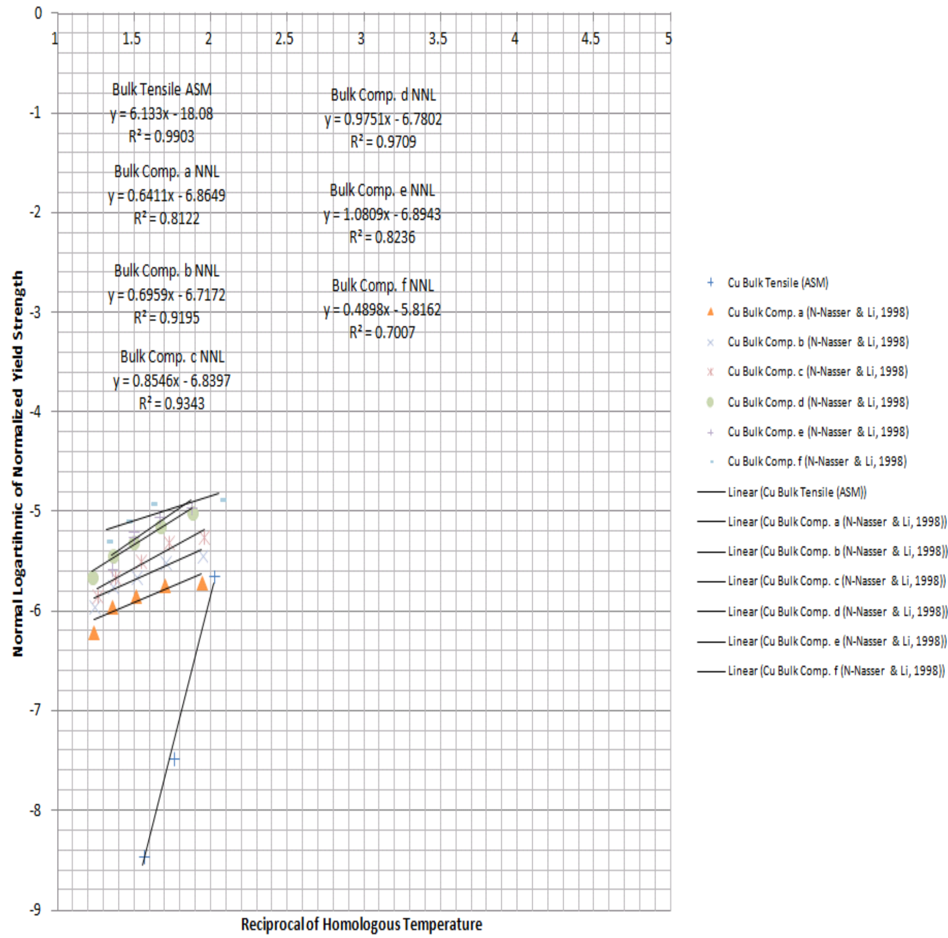

Figure 4-20 Linear plot of Cu bulk materials in Zone I corresponding to proposed model III

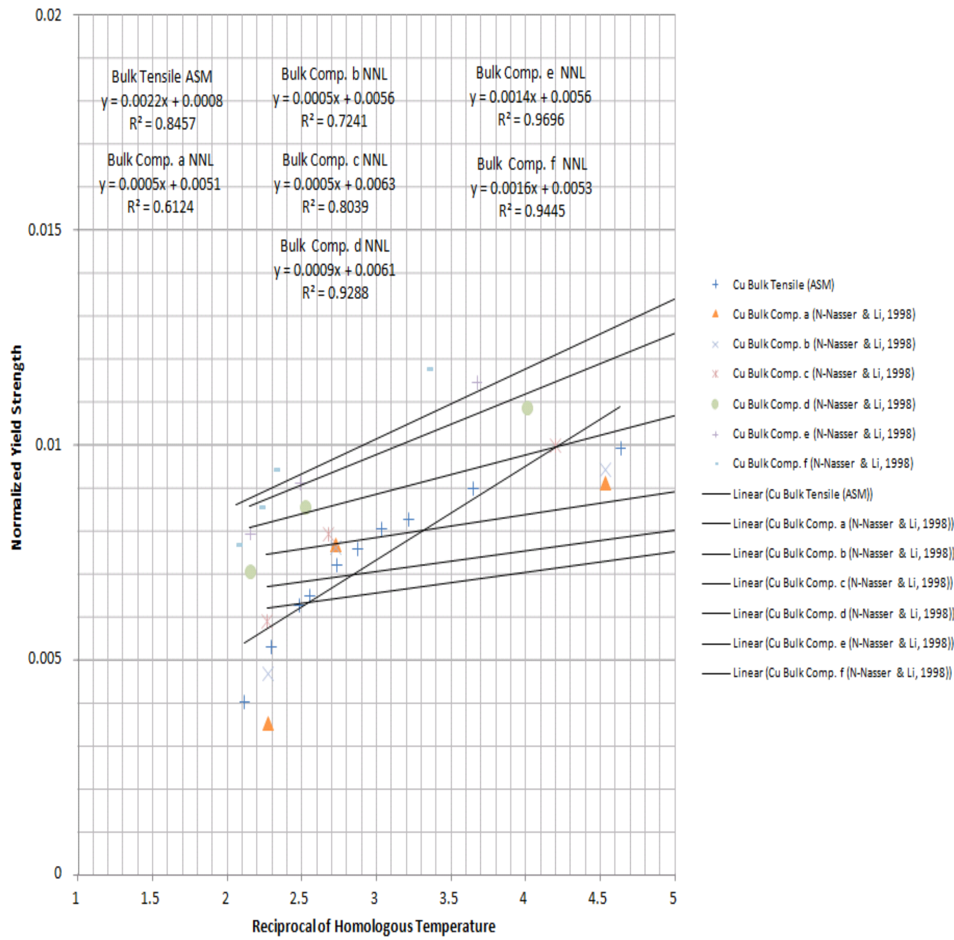

Figure 4-21 Linear plot of Cu bulk materials in Zone II corresponding to proposed model I

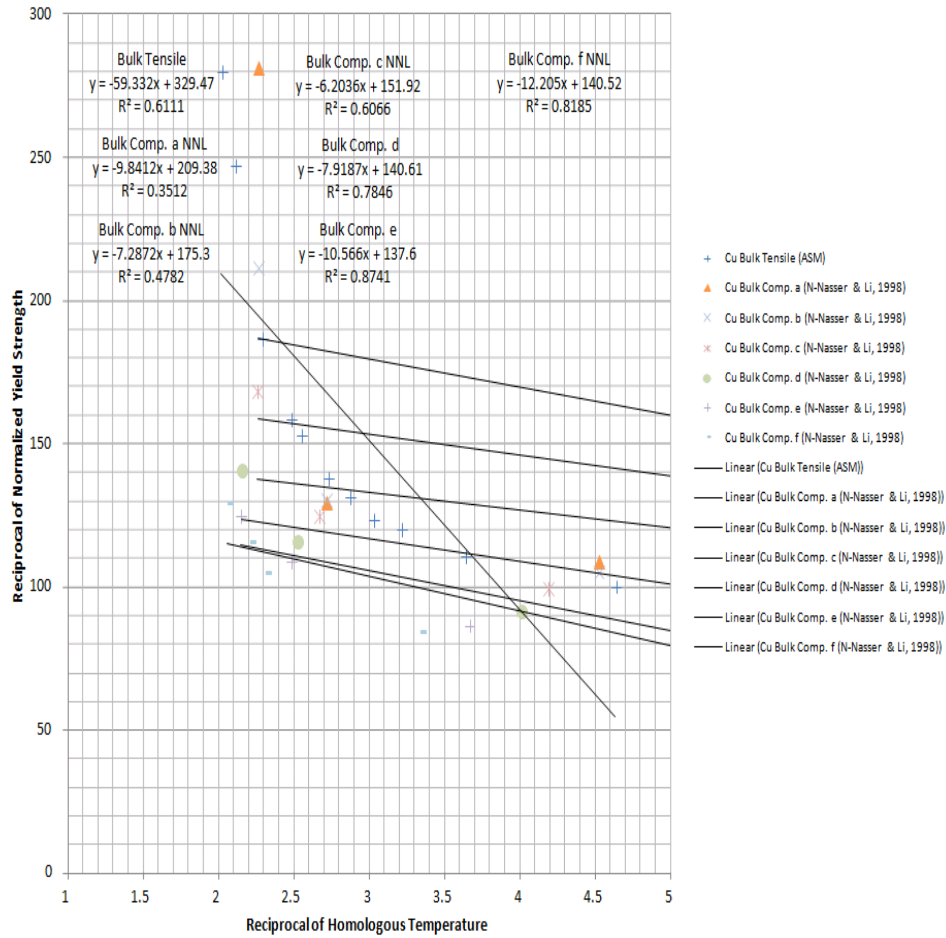

Figure 4-22 Linear plot of Cu bulk materials in Zone II corresponding to proposed model II

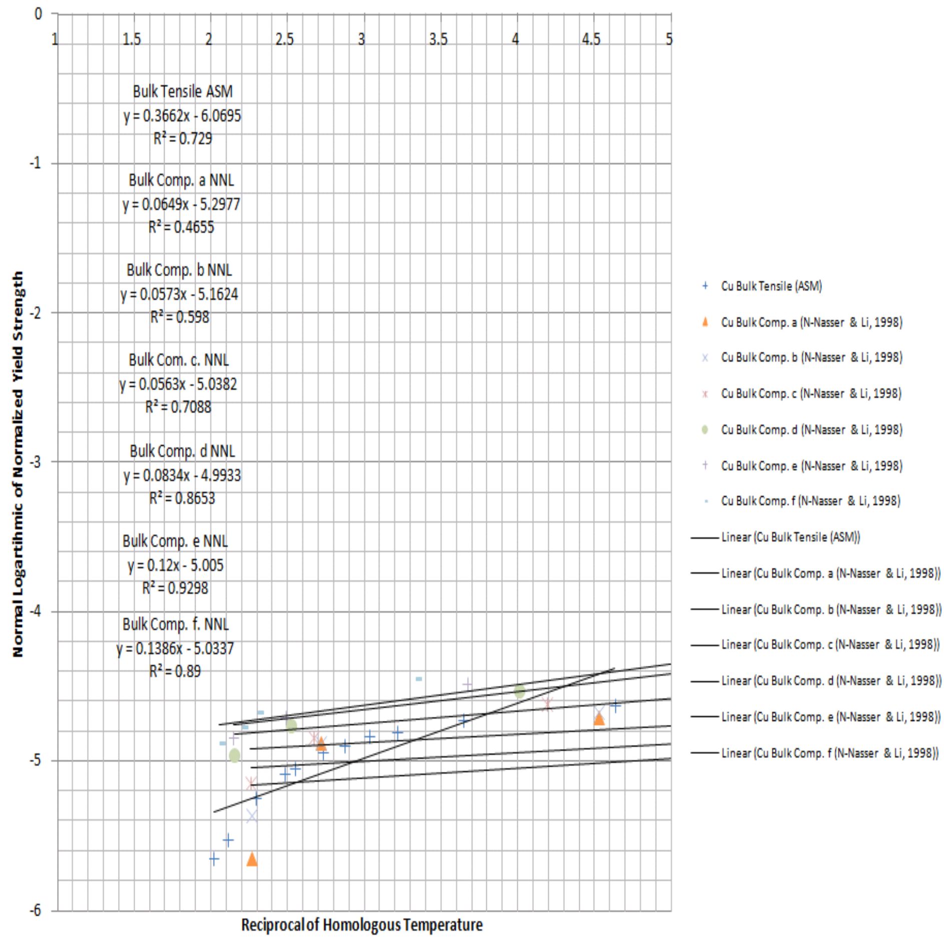

Figure 4-23 Linear plot of Cu bulk materials in Zone II corresponding to proposed model III

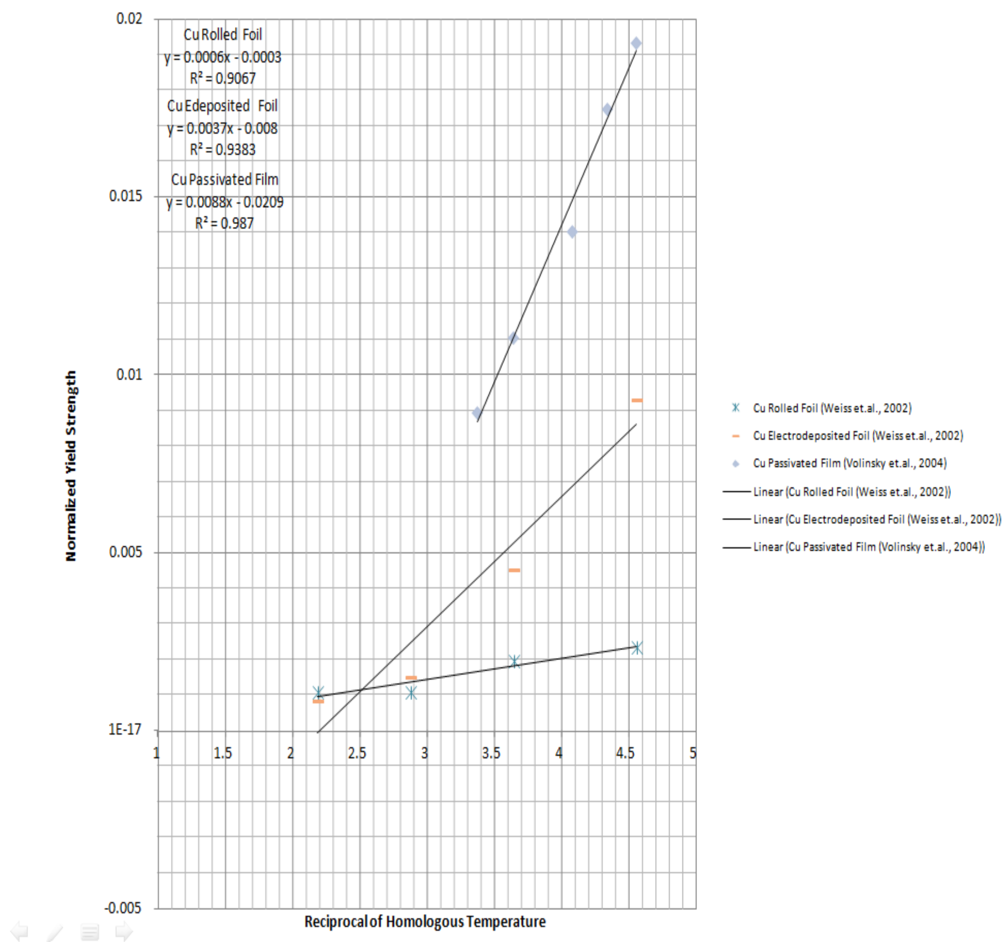

Figure 4-24 Linear plot of Cu confined materials corresponding to proposed model I

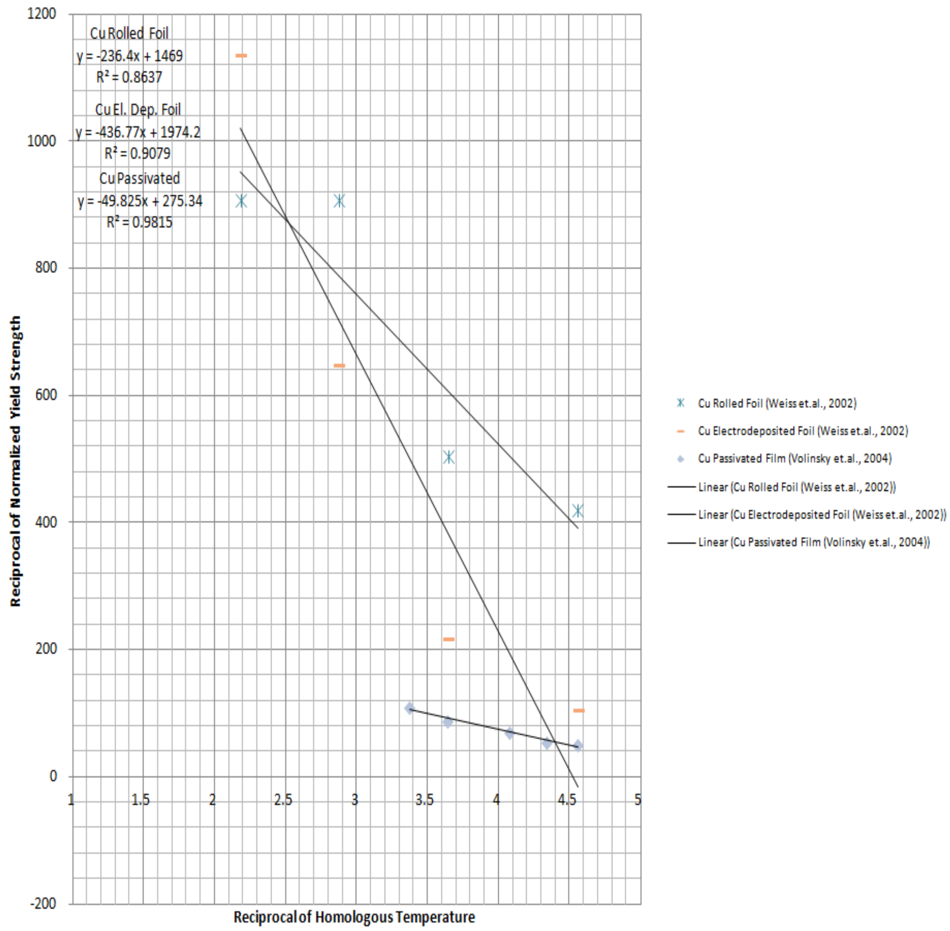

Figure 4-25 Linear plot of Cu confined materials corresponding to proposed model II

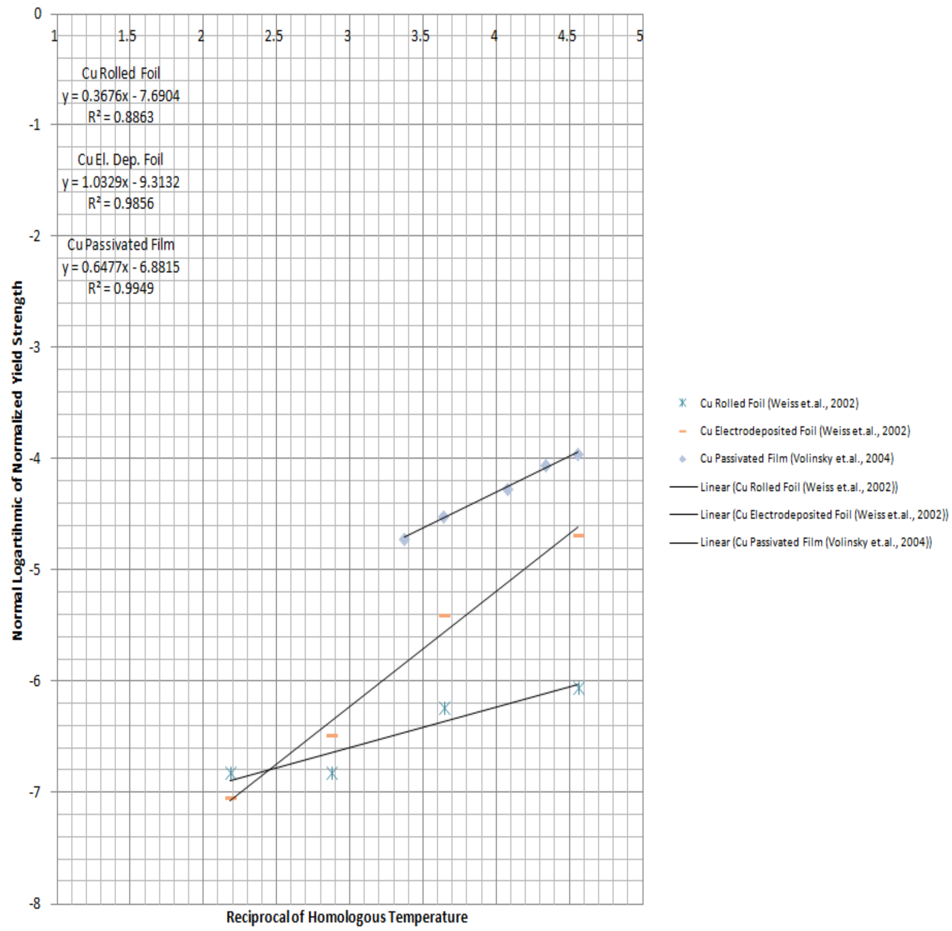

Figure 4-26 Linear plot of Cu confined materials corresponding to proposed model III

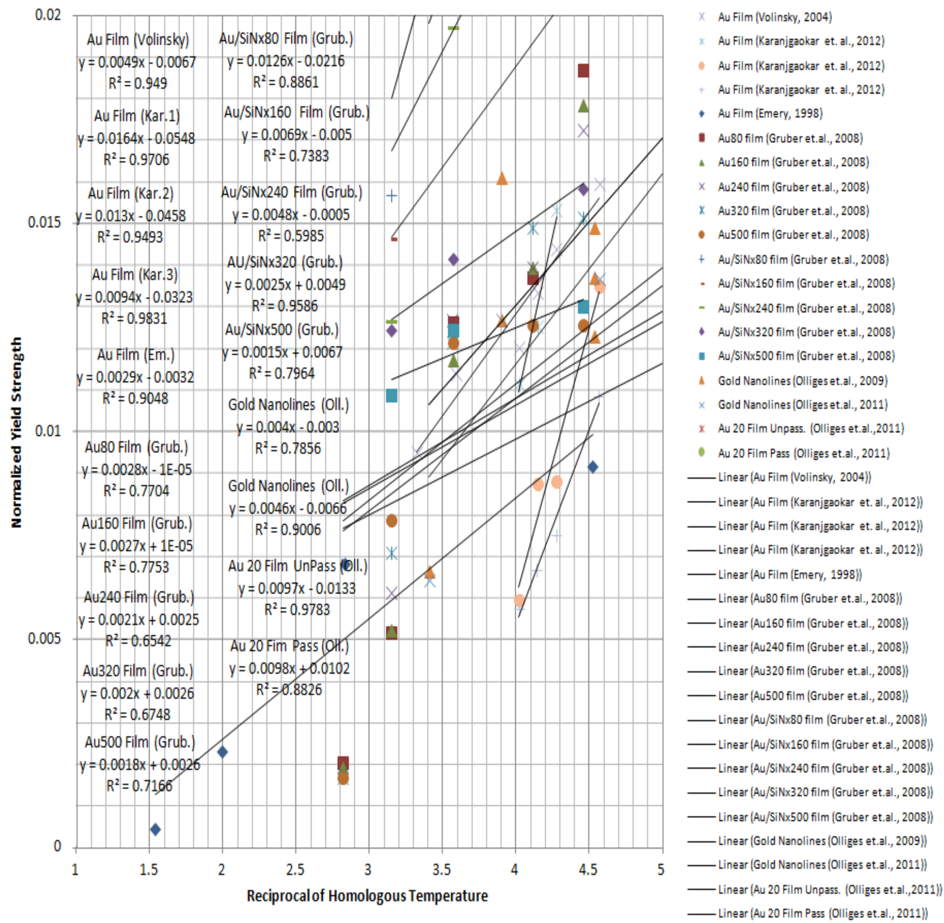

Figure 4-27 Linear plot of Au confined materials corresponding to proposed model I

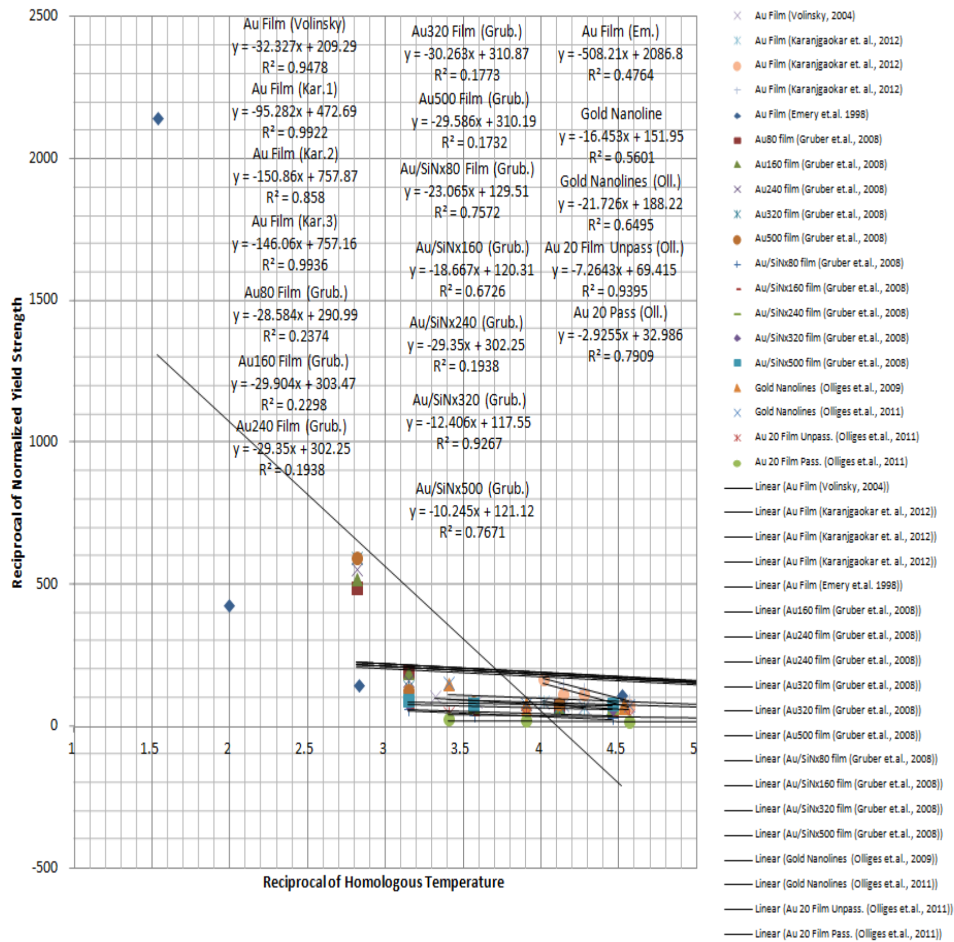

Figure 4-28 Linear plot of Au confined materials corresponding to proposed model II

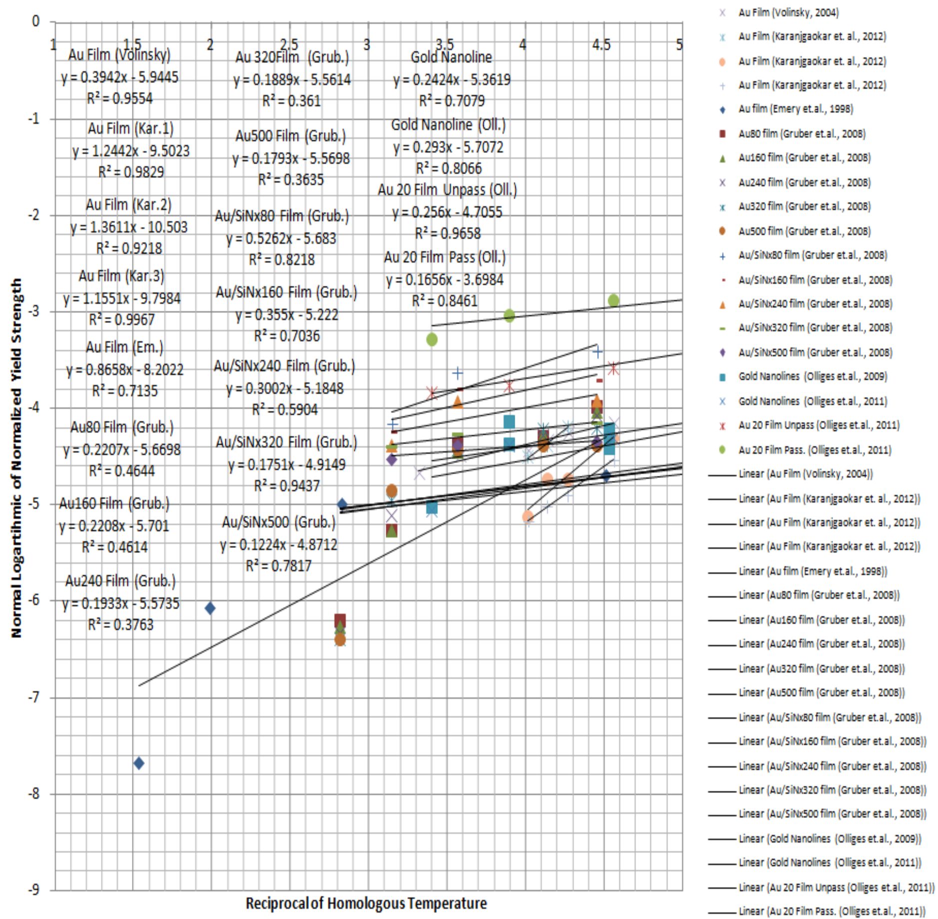

Figure 4-29 Linear plot of Au confined materials corresponding to proposed model III

Table 4-1 Linear regression analysis (least-squares fit to straight line) of Bulk Al and Cu

Material	Model	Zone I	Zone II	All Range
Al Bulk Tensile (ASM)	I	y = 0.001x - 0.001 R^2 = **0.9958**	y = 4E-05x + 0.0012 R^2 = **0.7566**	y = 9E-05x + 0.0008 R^2 = **0.482**
	II	y = -2423.5x + 5731.4 R^2 = **0.9717**	y = -20.286x + 838.15 R^2 = **0.671**	y = -93.319x + 1432.9 R^2 = **0.2707**
	III	y = 1.528x - 9.9406 R^2 = **0.9972**	y = 0.0284x - 6.7376 R^2 = **0.7152**	y = 0.0862x - 7.2117 R^2 = **0.3678**
Cu Bulk Tensile (ASM)	I	y = 0.0075x - 0.0118 R^2 = **0.8811**	y = 0.0022x + 0.0008 R^2 = **0.8457**	y = 0.0033x - 0.003 R^2 = **0.8073**
	II	y = -9327.7x + 18806 R^2 = **0.9326**	y = -59.332x + 329.47 R^2 = **0.6111**	y = -835.35x + 2869.8 R^2 = **0.2868**
	III	y = 6.133x - 18.08 R^2 = **0.9903**	y = 0.3662x - 6.0695 R^2 = **0.729**	y = 0.9967x - 8.1447 R^2 = **0.5079**
Bulk Comp. a (NNL)	I	y = 0.0018x + 0.0001 R^2 = **0.8594**	y = 0.0005x + 0.0051 R^2 = **0.6124**	y = 0.0007x + 0.0027 R^2 = **0.7031**
	II	y = -239.21x + 731.32 R^2 = **0.7605**	y = -9.8412x + 209.38 R^2 = **0.3512**	y = -23.052x + 347.4 R^2 = **0.4599**
	III	y = 0.6411x - 6.8649 R^2 = **0.8122**	y = 0.0649x - 5.2977 R^2 = **0.4655**	y = 0.1175x - 5.853 R^2 = **0.5855**
Bulk Comp. b (NNL)	I	y = 0.0025x - 0.0002 R^2 = **0.9514**	y = 0.0005x + 0.0056 R^2 = **0.7241**	y = 0.0007x + 0.0034 R^2 = **0.7492**
	II	y = -200.05x + 595.87 R^2 = **0.8774**	y = -7.2872x + 175.3 R^2 = **0.4782**	y = -17.022x + 276.57 R^2 = **0.4753**
	III	y = 0.6959x - 6.7172 R^2 = **0.9195**	y = 0.0573x - 5.1624 R^2 = **0.598**	y = 0.1017x - 5.6294 R^2 = **0.6179**
Bulk Comp. c (NNL)	I	y = 0.0035x - 0.0013 R^2 = **0.9579**	y = 0.0005x + 0.0063 R^2 = **0.8039**	y = 0.0008x + 0.0038 R^2 = **0.7595**
	II	y = -213.65x + 585.65 R^2 = **0.8991**	y = -6.2036x + 151.92 R^2 = **0.6066**	y = -15.654x + 242.88 R^2 = **0.4369**
	III	y = 0.8546x - 6.8397 R^2 = **0.9343**	y = 0.0563x - 5.0382 R^2 = **0.7088**	y = 0.1035x - 5.4974 R^2 = **0.6036**
Bulk Comp. d (NNL)	I	y = 0.0049x - 0.0024 R^2 = **0.9943**	y = 0.0009x + 0.0061 R^2 = **0.9288**	y = 0.0012x + 0.004 R^2 = **0.8586**
	II	y = -198.21x + 506.48 R^2 = **0.9283**	y = -7.9187x + 140.61 R^2 = **0.7846**	y = -17.606x + 210.84 R^2 = **0.5009**
	III	y = 0.9751x - 6.7802 R^2 = **0.9709**	y = 0.0834x - 4.9933 R^2 = **0.8653**	y = 0.1372x - 5.3871 R^2 = **0.6924**
Bulk Comp. e (NNL)	I	y = 0.0059x - 0.0036 R^2 = **0.8877**	y = 0.0014x + 0.0056 R^2 = **0.9696**	y = 0.0018x + 0.0033 R^2 = 0.9032
	II	y = -203.94x + 505.25 R^2 = **0.7517**	y = -10.566x + 137.6 R^2 = **0.8741**	y = -22.92x + 205.18 R^2 = **0.5433**
	III	y = 1.0809x - 6.8943 R^2 = **0.8236**	y = 0.12x - 5.005 R^2 = **0.9298**	y = 0.1925x - 5.4043 R^2 = **0.7456**
Bulk Comp. f (NNL)	I	y = 0.0032x + 0.0015 R^2 = **0.7404**	y = 0.0016x + 0.0053 R^2 = **0.9445**	y = 0.0019x + 0.004 R^2 = **0.9226**
	II	y = -76.617x + 277.68 R^2 = **0.6569**	y = -12.205x + 140.52 R^2 = **0.8185**	y = -19.888x + 177.97 R^2 = **0.6628**
	III	y = 0.4898x - 5.8162 R^2 = **0.7007**	y = 0.1386x - 5.0337 R^2 = **0.89**	y = 0.1866x - 5.268 R^2 = **0.811**

Table 4-2 Linear regression analysis (least-squares fit to straight line) of confined Al data

Material	Model	Slope (b) ± se(b)	Intercept (a) ± se(a)	Rsq (R^2)
Al Foil (Calculated)	I	+0.00009±0.000031	0.001419±0.0004152	0.4907
	II	--27.850±13.9655	983.036±185.1011	0.3065
	III	+0.04492±0.018258	-6.73851±0.241992	0.4022
Bulge Test, Inert Gas Al Foil t=1100nm (Sputtered)	I	+0.0045±0.00044	-0.0075±0.00106	0.9815
	II	-671.82±199.527	+2137.2±484.43	0.85
	III	+1.4938±0.14482	- 9.575±0.3516	0.9816

Table 4-3 Linear regression analysis (least-squares fit to straight line) of confined Cu data

Material	Model	Slope (b) ± se(b)	Intercept (a) ± se(a)	Rsq (R^2)
Strain Rate: 10^{-4}/s Cu Foil t=35000nm (Rolled)	I	+0.0006±0.00014	-0.0003±0.00047	0.9067
	II	-236.4±66.41	+1469±227.6	0.8637
	III	+0.3676±0.09312	-7.6904±0.31915	0.8863
Strain Rate: 10^{-4}/s Cu Foil t=35000nm (Electrodeposited)	I	+0.0037±0.00066	-0.008±0.0022	0.9383
	II	-436.77±98.395	+1974.2±337.24	0.9079
	III	+1.0329±0.08841	- 9.3132±0.30303	0.9856
Strain Rate: 4 x 10^{-3}/s Cu Film t=3200nm (Sputtered, Pt-Passivated)	I	+0.009±0.00058	-0.0209±0.00233	0.9870
	II	-49.8254±3.9499	+275.345±15.8771	0.9815
	III	+0.647725±0.02690	-6.88147±0.10814	0.9949

Table 4-4 Linear regression analysis of confined Au data >500nm

Material	Model	Slope (b) ± se(b)	Intercept (a) ± se(a)	Rsq (R^2)
Strain Rate: 4 x 10^{-3}/s Au Film t=2700nm (Sputtered)	I	+0.0049±0.00057	-0.0067± 0.00227	0.9490
	II	-32.33±3.794	+209.29±15.188	0.9478
	III	+0.3942±0.04260	-5.9445±0.17054	0.9554
Strain Rate: 5 x10^{-4}/s Au Film t=2100nm (Thermal Evaporated)	I	+0.0029±0.00067	-0.0032±0.00196	0.9048
	II(*)	-508.21±376.7378	+2086.8±1109.37	0.4764
	III(*)	+0.8658±0.387979	-8.2022±1.14247	0.7135
Strain Rate: 4-5 x10^{-2}/s Au Film t=850nm (Sputtered)	I	+0.0164±0.00276	-0.0548±0.01175	0.9706
	II(***)	-95.282±16.5864	+472.69±70.528	0.9922
	III	+1.2442±0.21278	-9.5023±0.90476	0.9829
Strain Rate: 5-7 x10^{-4}/s Au Film t=850nm (Sputtered)	I	+0.013±0.0021	-0.0458±0.00901	0.9493
	II	-150.84±43.398	+757.87±184.535	0.858
	III	+1.3609±0.28022	-10.503±1.1916	0.9218
Strain Rate: 5-6 x10^{-5}/s Au Film t=850nm (Sputtered)	I	+0.0094±0.00088	-0.0323±0.00372	0.9831
	II(***)	-146.04±8.261	+757.16±35.126	0.9936
	III	+1.155±0.0473	-9.7984±0.20118	0.9967

Table 4-5 Linear regression analysis of confined Au data <500nm

Material	Model	Slope (b) ± se(b)	Intercept (a) ± se(a)	Rsq (R^2)
Strain Rate: 5.2 $x10^{-5}$/s Au Film t=500nm (Magnetron Sputtered)	I	0.0018±0.00057	0.0026±0.00315	0.7166
	II	29.586±32.3259	310.19±177.901	0.1732
	III	0.1793±0.11864	-5.5698±0.65293	0.3635
Strain Rate: 5.2 $x10^{-5}$/s SiNx/Au/SiNx Film t=500nm (Magnetron Sputtered)	I	0.0015±0.00074	0.0067±0.00279	0.7964
	II	10.245±5.6452	121.12±21.240	0.7671
	III	0.1224±0.06467	-4.8712±0.24331	0.7817
Strain Rate: 5.2 $x10^{-5}$/s Au Film t=320nm (Magnetron Sputtered)	I	0.002±0.0007	0.0026±0.00383	0.6748
	II	-30.263±32.5922	310.87±179.3664	0.1773
	III	0.1889±0.12564	-5.5614±0.69144	0.3610
Strain Rate: 5.2 $x10^{-5}$/s SiNx/Au/SiNx Film t=320nm (Magnetron Sputtered)	I(**)	0.0025±0.00052	0.0049±0.00194	0.9586
	II(**)	12.406±3.4883	117.55±13.125	0.9267
	III(**)	0.1751±0.04278	-4.9149±0.16097	0.9437
Strain Rate: 5.2 $x10^{-5}$/s Au Film t=240nm (Magnetron Sputtered)	I	0.0021±0.00076	0.0025±0.00418	0.6542
	II	-29.35±29.930	302.25±164.713	0.1938
	III	0.1933±0.12440	-5.5735±0.68462	0.3763
Strain Rate: 5.2 $x10^{-5}$/s SiNx/Au/SiNx Film t=240nm (Magnetron Sputtered).	I	0.0048±0.00397	-0.0005±0.01492	0.5985
	II	-18.9475±16.01284	130.3396±60.24891	0.5834
	III	0.3002±0.25006	-5.1848±0.94084	0.5904
Strain Rate: 5.2 $x10^{-5}$/s Au Film t=160nm (Magnetron Sputtered)	I	0.0027±0.00073	-0.00001±0.004006	0.7753
	II	-29.904±27.3696	303.47±150.624	0.2298
	III	0.2208±0.11925	-5.701±0.65628	0.4614
Strain Rate: 5.2 $x10^{-5}$/s SiNx/Au/SiNx Film t=160nm (Magnetron Sputtered)	I	0.0069±0.00412	-0.005±0.0155	0.7383
	II	-18.667±13.0250	120.31±49.007	0.6726
	III	0.355±0.230408	-5.222±0.8669	0.7036
Strain Rate: 5.2 $x10^{-5}$/s Au Film t=80nm (Magnetron Sputtered)	I	0.0028±0.00076	-0.00001±0.004200	0.7704
	II	-28.584±25.6158	290.99±140.972	0.2374
	III	0.2207±0.11849	-5.6698±0.65209	0.4644
Strain Rate: 5.2 $x10^{-5}$/s SiNx/Au/SiNx Film t=80nm (Magnetron Sputtered)	I(**)	0.0126±0.00452	-0.0216±0.01701	0.8861
	II	-23.065±13.0605	129.51±49.141	0.7572
	III	0.5262±0.24503	-5.683±0.9219	0.8218
Strain Rate: 3-8 $x10^{-6}$ Gold Nanolines h=20nm (2009)	I	0.004±0.0007	-0.003±0.0038	0.7856
	II	-16.453±4.8606	151.95±26.658	0.5601
	III	0.2424±0.05191	-5.3619±0.28469	0.7079
Strain Rate: 3-8 $x10^{-6}$ Gold Nanolines h=20nm (2011)	I(**)	0.0046±0.00088	-0.0066±0.00470	0.9006
	II	-21.726±9.2141	188.22±49.322	0.6495
	III	0.293±0.0829	-5.7072±0.44347	0.8066
Strain Rate: 3.3-3.9 $x10^{-5}$ Au Film t=20nm (Sputtered, Unpass.)	I(**)	0.0097±0.00084	-0.0133±0.00448	0.9783
	II(**)	-7.2643±1.06413	69.415±5.6961	0.9395
	III(**)	0.256±0.0278	-4.7055±0.14889	0.9658
Strain Rate: 3.1-3.9 $x10^{-5}$ Au Film t=20nm (Sputtered, Passivated 0.7μ)	I(**)	0.0098±0.00205	0.0102±0.01100	0.8826
	II	-2.9255±0.86849	32.986±4.64887	0.7909
	III	0.1656±0.040775	-3.6984±0.21826	0.8461

Chapter 5

Discussion

Preliminary Examination

Typical (averaged) behavior of the experimental data of confined materials plotted in Figure 1-1 is depicted in Figure 5-1. It should be noted that all experimental data used to develop the models are particularly the representation of behaviors within the space of interest ($2<(T_M/T)<25$). It can be seen from Figure 5-1 that the confined materials behave averagely as it had been predicted by the first principles discussed in Chapter 2. Within the range of arguments, it is generally sound and reasonable to assume a single physical-mechanistic model to describe and predict the behavior. The behavior can be described as a *non-linear decrease* of flow stress with the increase of temperature and the phenomena can be assumed to be predominantly driven by *a thermally-activated dislocation-mediated obstacles-controlled* local mechanism.

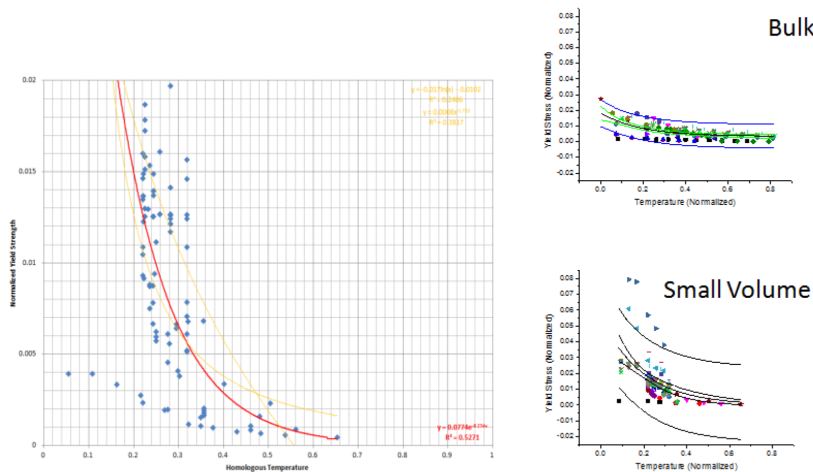

Figure 5-1 Typical (averaged) behavior of confined materials

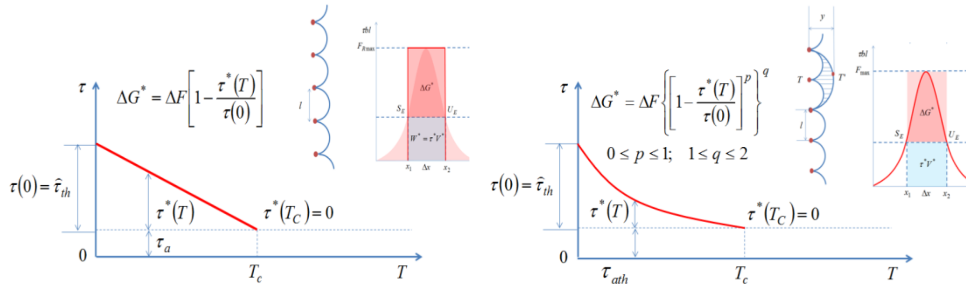

Figure 5-2 Idealized and real description of the behavior

(after ref.[105,106])

The *plateau-like stress* described in Figure 5-1 and Figure 5-2 is a very important physical mechanistic phenomenon, from which the foundation for the model was initially constructed[105,106]. Another important feature with regard to the foundation of the model is the *mechanical threshold stress*, which is experimentally defined as the flow stress at absolute zero and used as the internal state parameter.

Normalizations of both dependent and independent variables provide important advantages in the development of a physical model in addition to the possibility of a fair direct global comparison. Normalization of yield stress by shear modulus along with the normalization of temperature with melting temperature would effectively remove the effect of temperature-dependent modulus[107]. Furthermore, while preserving a scale of temperature in Celcius, the homologous temperature may also be readily linked to the evolution of the structure and internal parameters. Such a normalized plot of stress-temperature data had been widely used in the construction of a deformation mechanism map, in which relationships are well displayed and from which physical mechanisms are readily identified[94,95,97].

Plotting the normalized stress against the reciprocal of the normalized temperature provides further benefits. A reciprocal relationship enables the linearization of the merit functions that were constructed from the first principles. With respect to the deformation mechanism map, it usefully alters the demarcation line between two regions of different mechanisms from a curve to a straight line. It results in a much simpler relationship. Langdon and Mohamed[108,109] have explored such a significant advantage and developed a simple new method of reconstructing deformation mechanism map based on it. The typical behavior of the confined material within the space of interest (2<(T_M/T)<25) can be idealized by a straight line in the zone II in Figure 5-3.

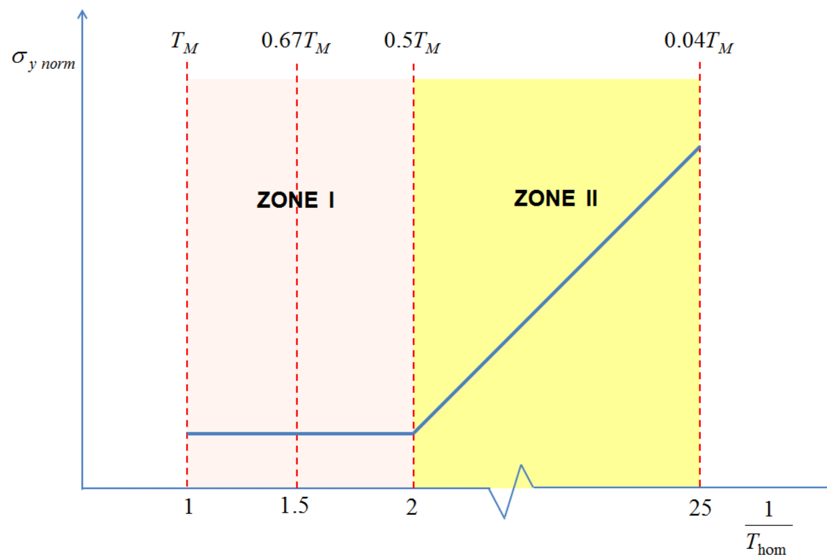

Figure 5-3 A reciprocal of homologous temperature plot representing the temperature-dependence of mechanical behavior in typical metals.

Three physically sound mathematical merit functions had been proposed in attempt to describe and predict the behavior of confined materials in the space of interest. Results of least square analysis (Table 4-2, 4-2, 4-3, 4-4) indicates that in most

cases the proposed models can be used to describe the temperature-dependent flow stress of metals interconnect at confined dimension. The strong correlations can be quantitatively identified from the high values of R^2 (R^2>0.85) for confined Al and Cu, which are 0.85 to 0.9816 (Table 4-2) and 0.8637 to 0.9949 (Table 4-3) respectively. For confined Au thicker than 500 nm (Table 4-4), the correlation factor is >0.85 for all sets of data with an exception (marked by (*)). For confined Au thinner than 500 (Table 4-5) the correlation factors for proposed model I, II, III are <0.85 except for 2 particular sets of data, which is >0.92 for all proposed models and two data associated with model I, which are 0.8861 and 0.8826 (all are marked by (**)). Another important picture captured from the least square analysis is the fact that the behavior of confined Au thinner than 500nm are consistently better represented by Model I.

It is generally accepted that a value of R^2 higher than 0.9 indicates strong correlation between x axis and y axis. In average, proposed model II has the lowest correlation factors with all sets of experimental data except two particular sets of them (marked by (***)). The facts that the correlation factors of Au below 500nm are very low for the majority of collected data give an initial indication that there exist different or additional mechanisms. Therefore, different proposed models may need to be formulated to describe and predict the behavior more accurately.

In general, it seems that the experimental data of confined metals exhibit more converged pattern compared to that of bulk. General comparison of all collected data shows that the typical (averaged) behaviors of bulk materials are closer to a logarithmic function whereas those of the confined materials are more appropriately described by an exponential function (Figure 4-4 and Figure 4-5). The facts that a particular merit function is more suitable in a particular situation support the idea that there present special characteristics and mechanisms.

Non-linear regression analysis of the concatenated data of small volume and bulk Cu, for example, has come to the conclusion that the two groups of experimental data are statistically different at 0.05 significant level (Figure 5-4).

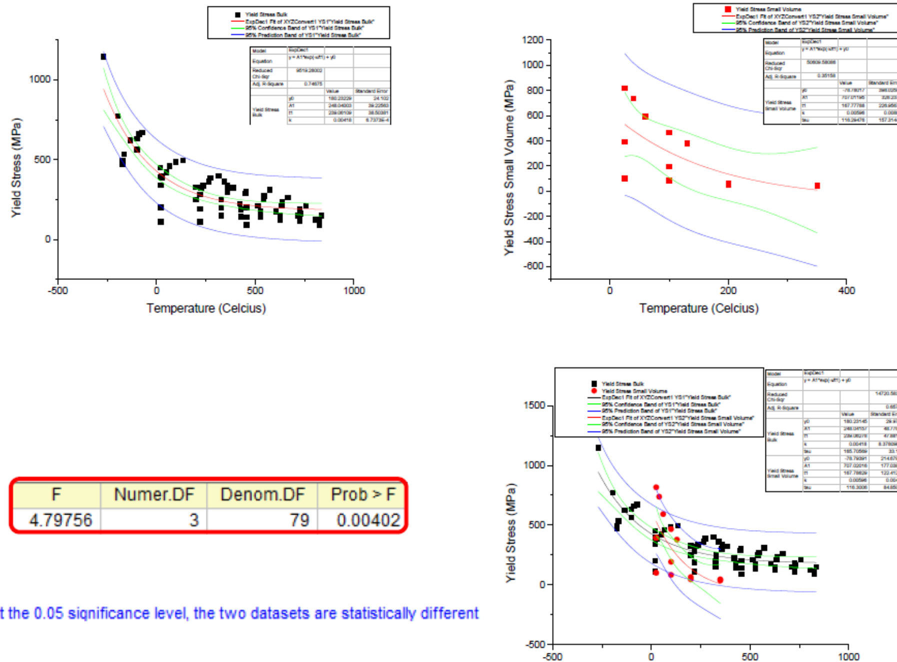

Figure 5-4 Comparison of bulk and small volume datasets of Cu

Moreover, it can be seen from the experimental data of bulk materials, measured at wider range of temperature, that the data cannot be continuously fitted into a single model with a single set of parameters. Points, at which the slopes change, can be readily recognized from the linearized plots of normalized data. Indeed, it may be directly interpreted as a boundary between two different mechanisms or comparable mechanisms with different set of parameters. Assuming a temperature of $0.5T_M$ as a demarcation between two zones of different mechanisms, the data have been fitted unconnectedly (Figure 4-9-Figure 4-11 and Figure 4-18-Figure 4-23). It has been

demonstrated that the correlation coefficients would increase when a model fitting is performed intermittently in the different defined zones. In such a particular situation, composite fitting are generally more reasonable. From which, a similar model with different parameters is much easier to be defined.

More comprehensive least square analysis of such data (Table 4-1) has revealed some additional facts. It can be seen from the available data for bulk Au and Cu that, in tension the behavior in zone I was better represented by Model III whereas in compression it was better described by Model I. In zone II, the space of interest, all bulk data are consistently better fitted in Model I. As a comparison, the experimental data of confined materials are by the same token fitted in either Model I or Model III. General exception was observed in confined Au thinner than 500nm, whose behavior are more appropriately described by Model I similar to that of bulk materials.

Models of the confined materials, fitted into the experimental data, are depicted in Figure 5-5-Figure 5-13.

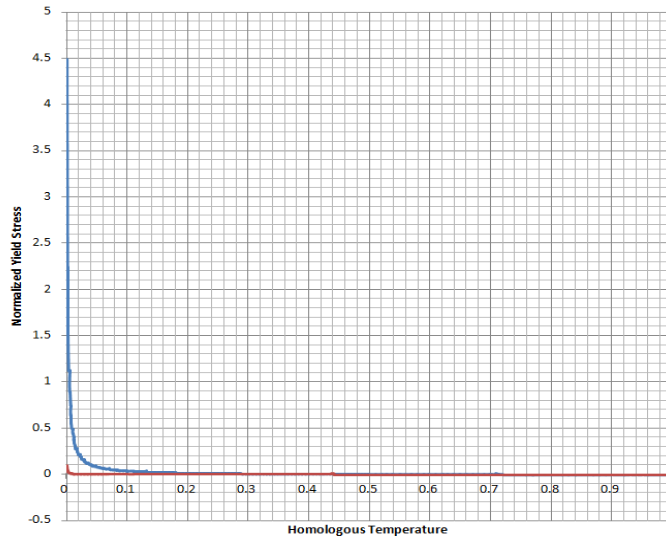

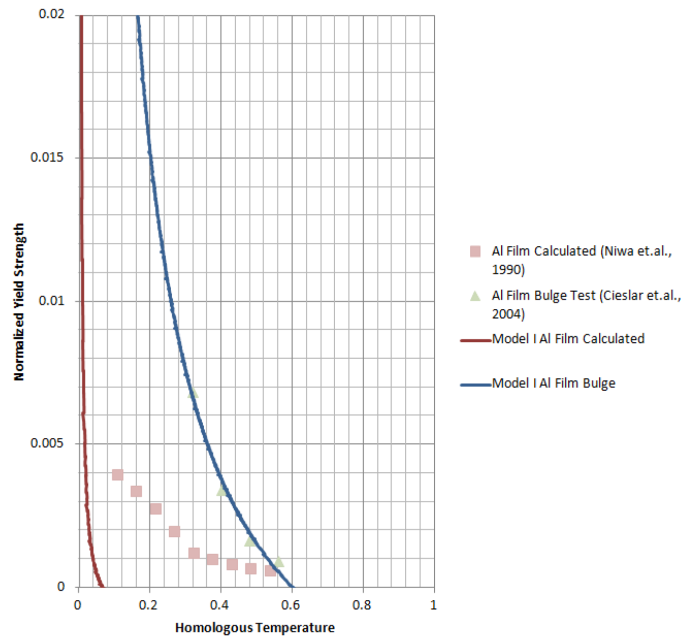

Figure 5-5 Model I fitted to the experimental data of confined Al

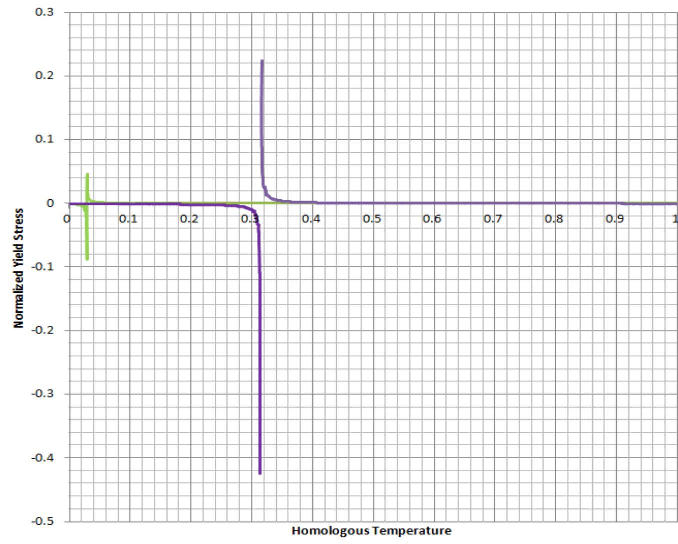

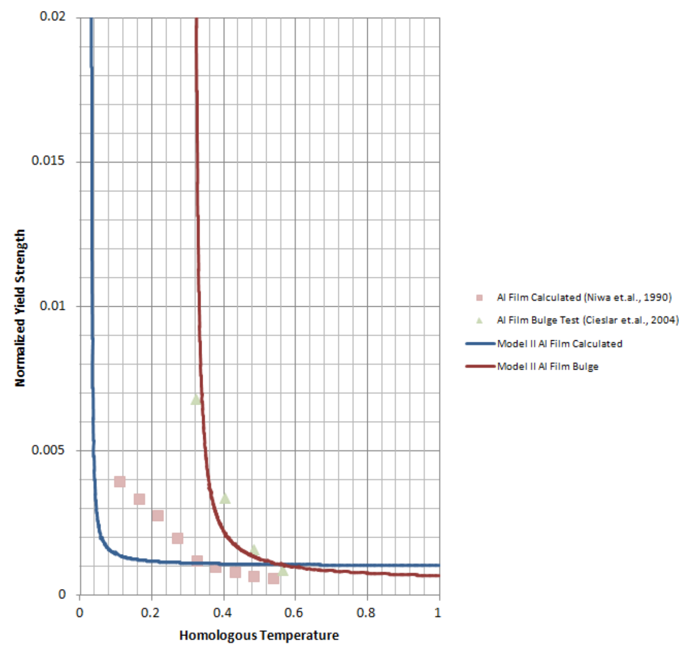

Figure 5-6 Model II fitted to the experimental data of confined Al

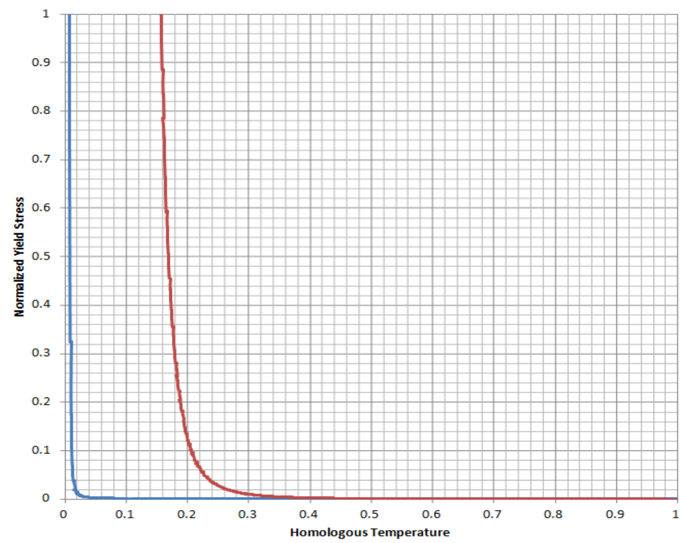

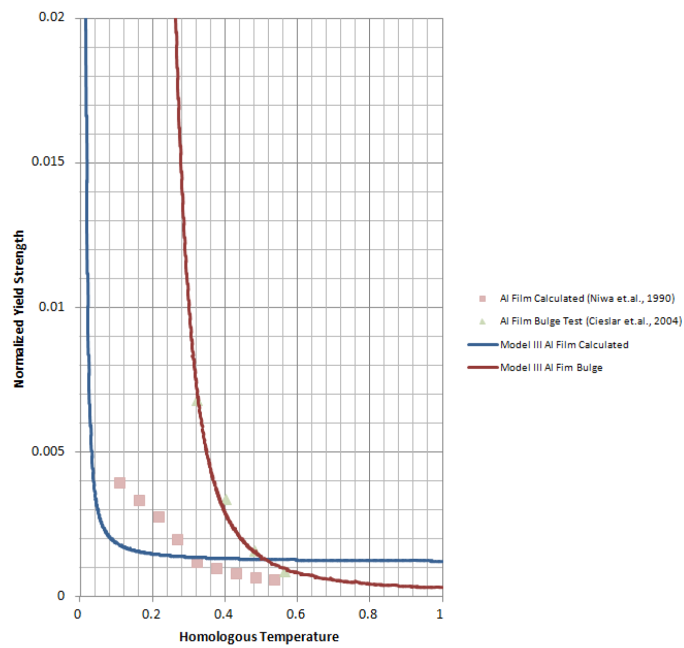

Figure 5-7 Model III fitted to the experimental data of confined Al

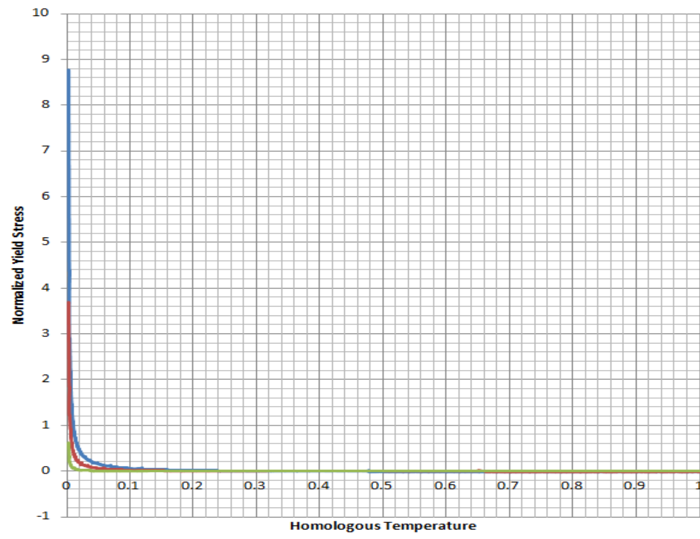

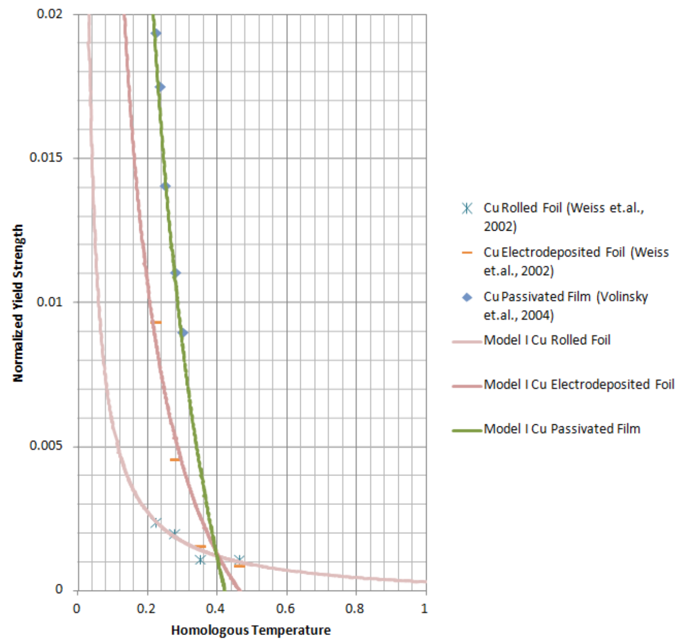

Figure 5-8 Model I fitted to the experimental data of confined Cu

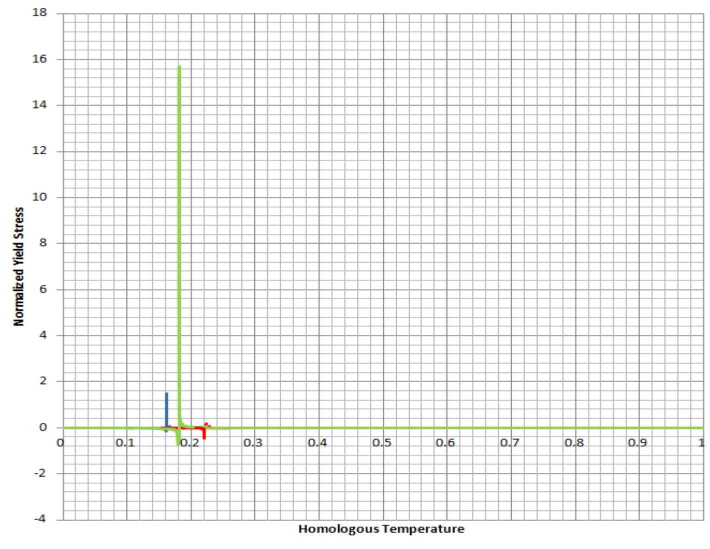

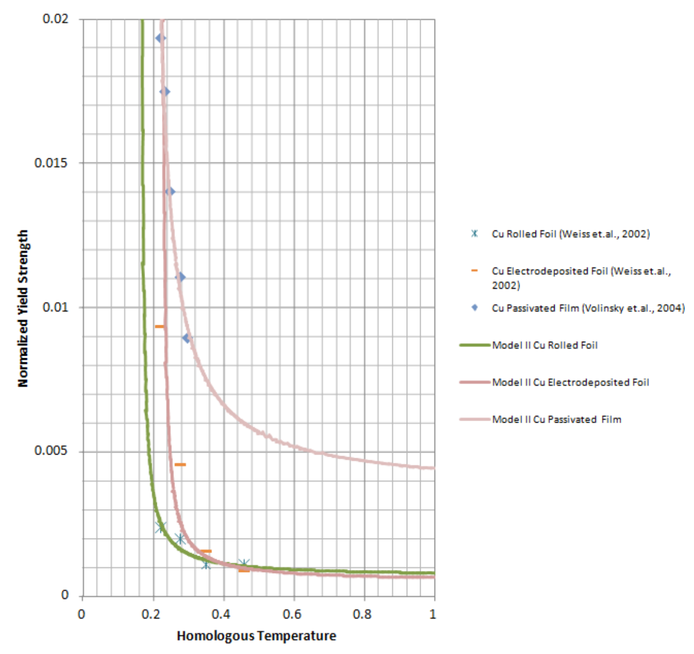

Figure 5-9 Model II fitted to the experimental data of confined Cu

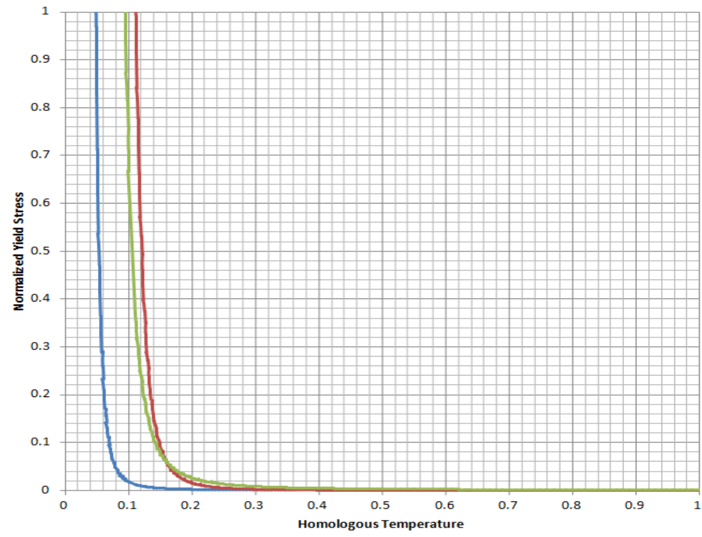

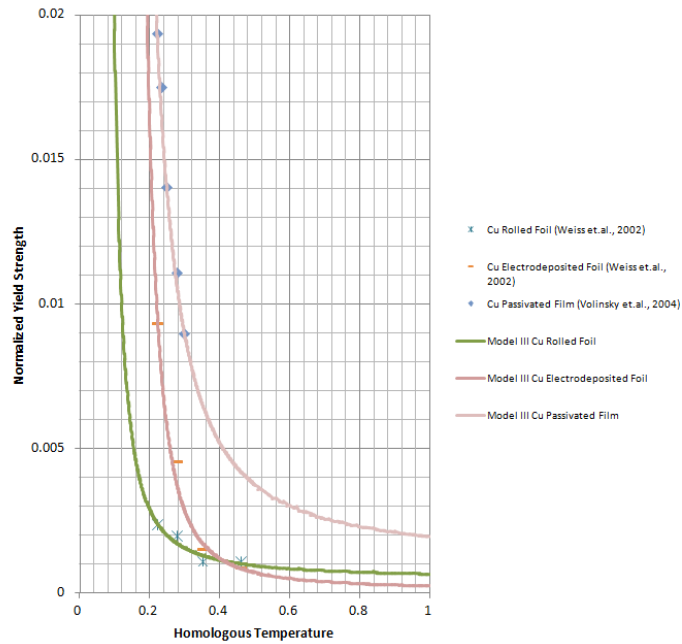

Figure 5-10 Model III fitted to the experimental data of confined Cu

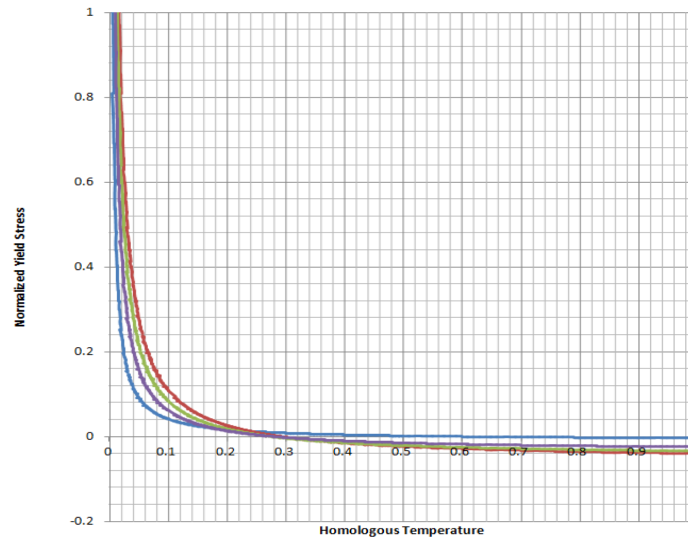

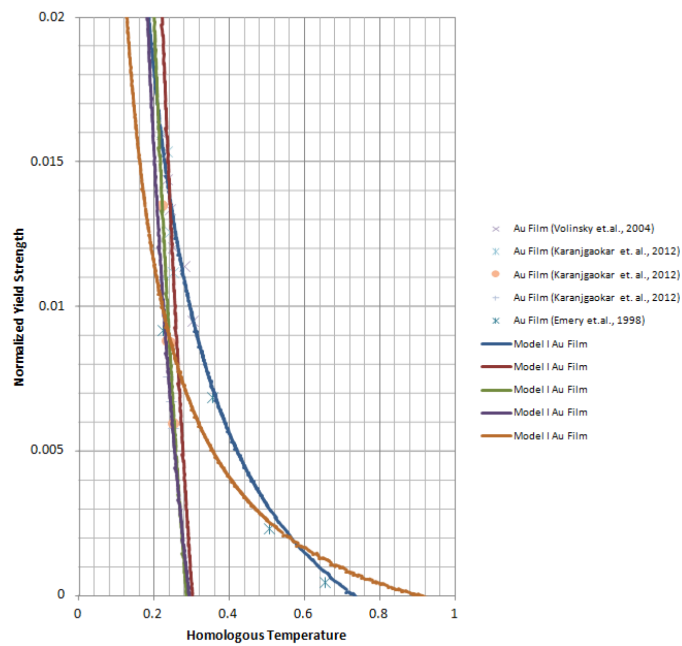

Figure 5-11 Model I fitted to the experimental data of confined Au

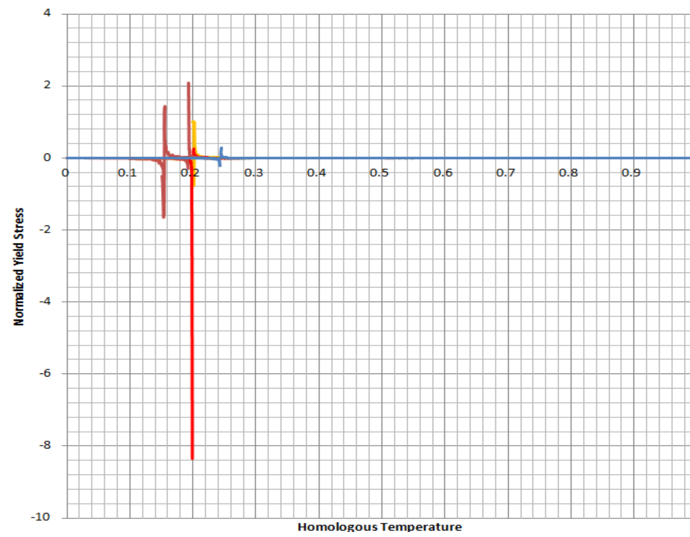

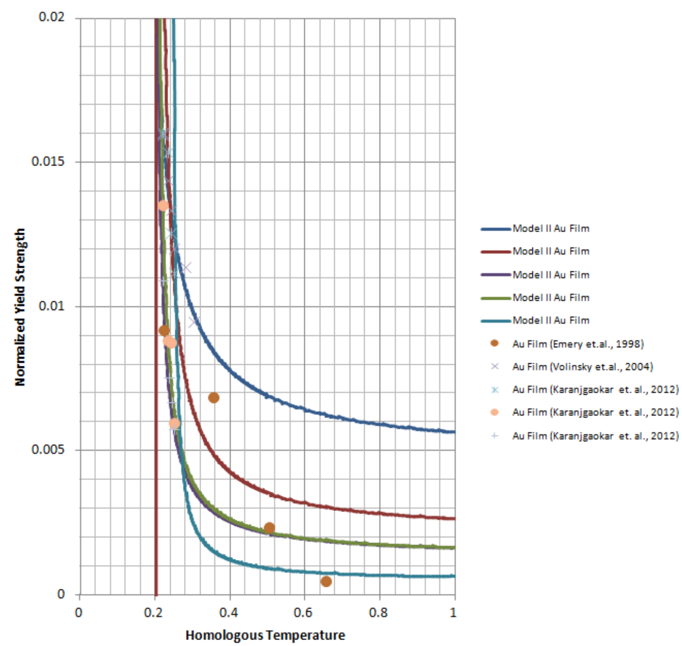

Figure 5-12 Model II fitted to the experimental data of confined Au

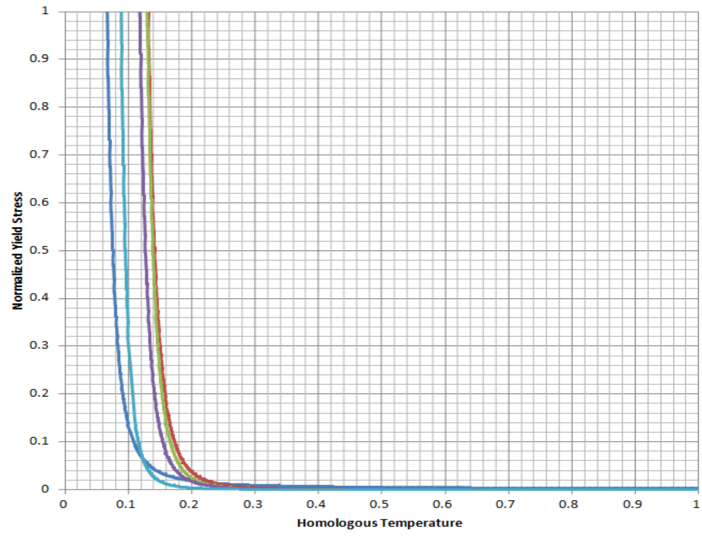

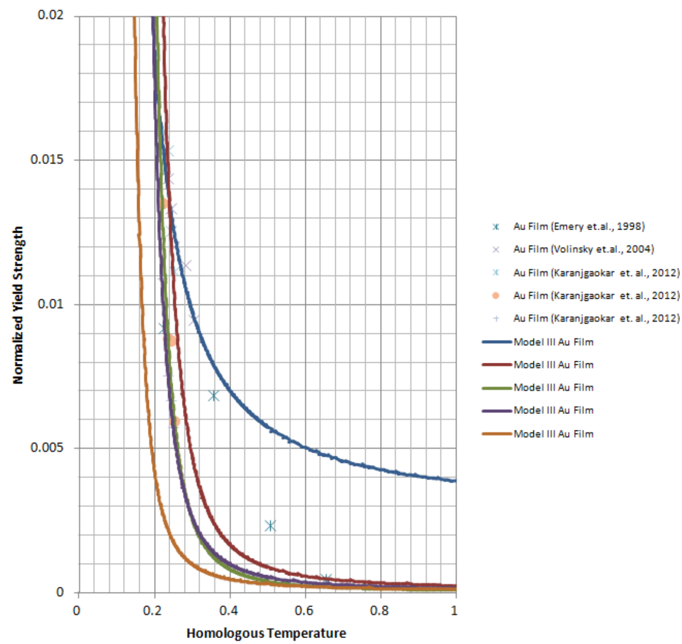

Figure 5-13 Model III fitted to the experimental data of confined Au

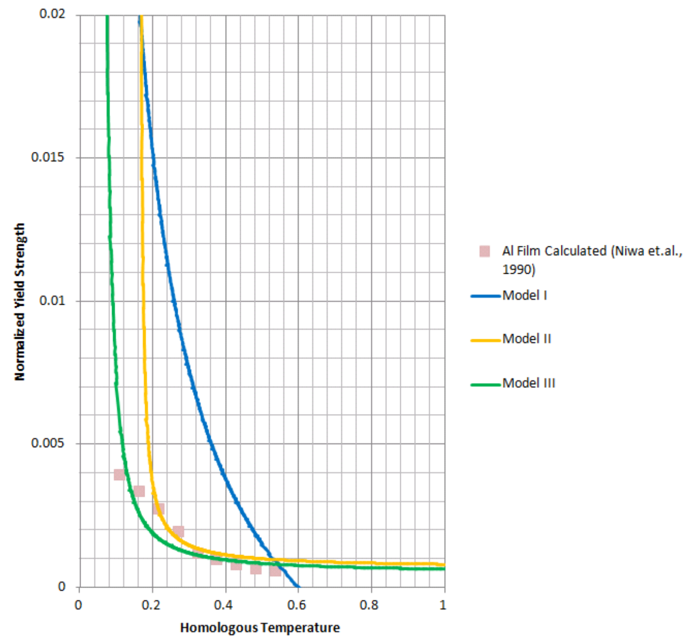

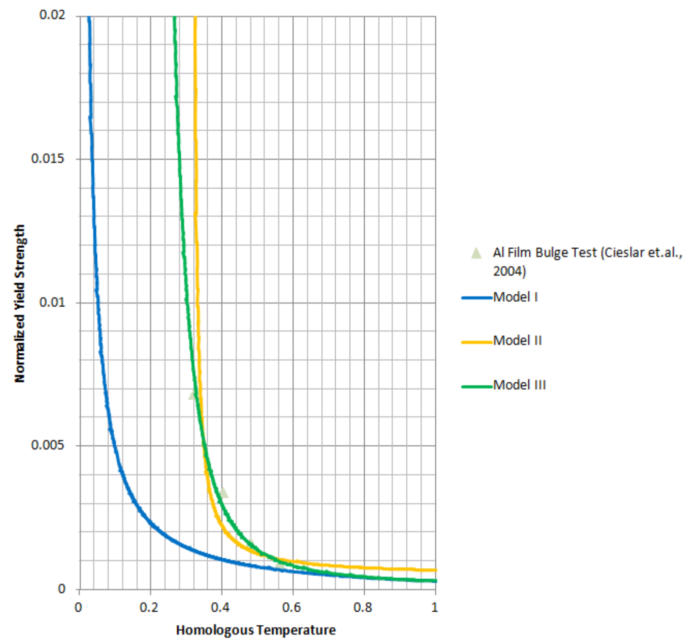

Figure 5-14 Model I, II, III fitted to the experimental data of confined Al

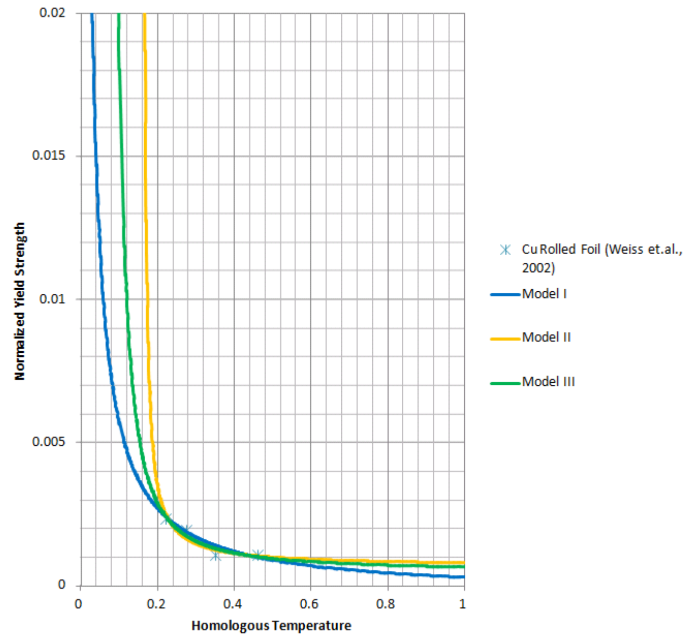

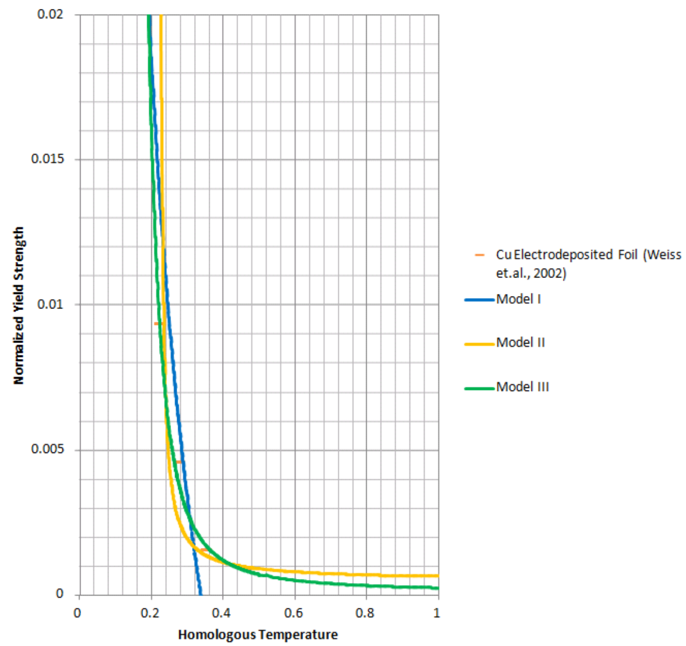

Figure 5-15 Model I, II, III fitted to the experimental data of confined Cu

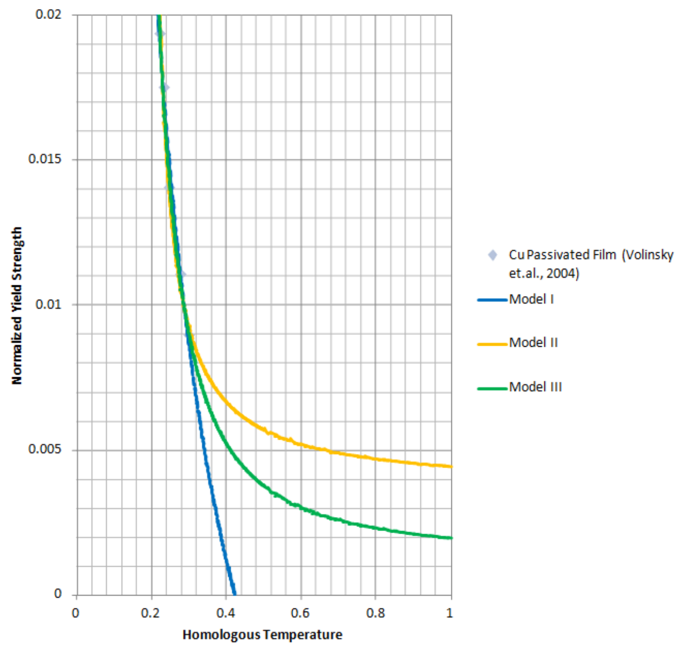

Figure 5-15 Continued

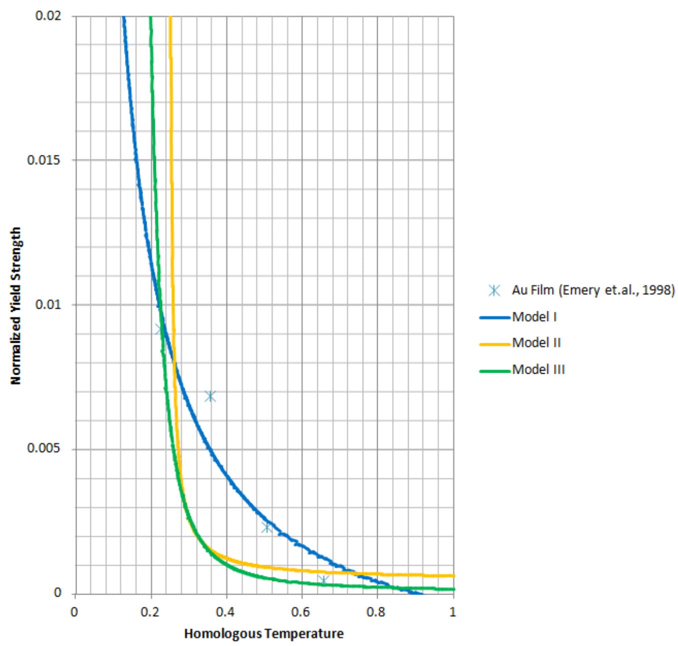

Figure 5-16 Model I, II, III fitted to the experimental data of confined Au

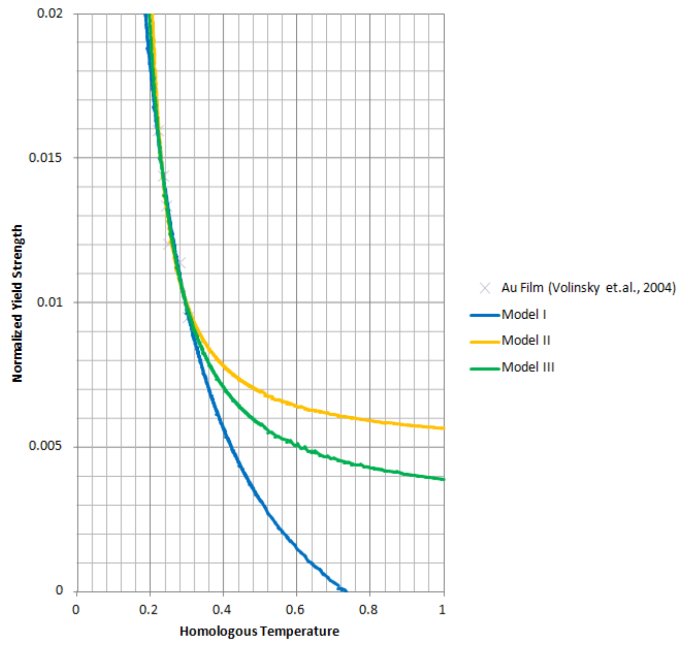

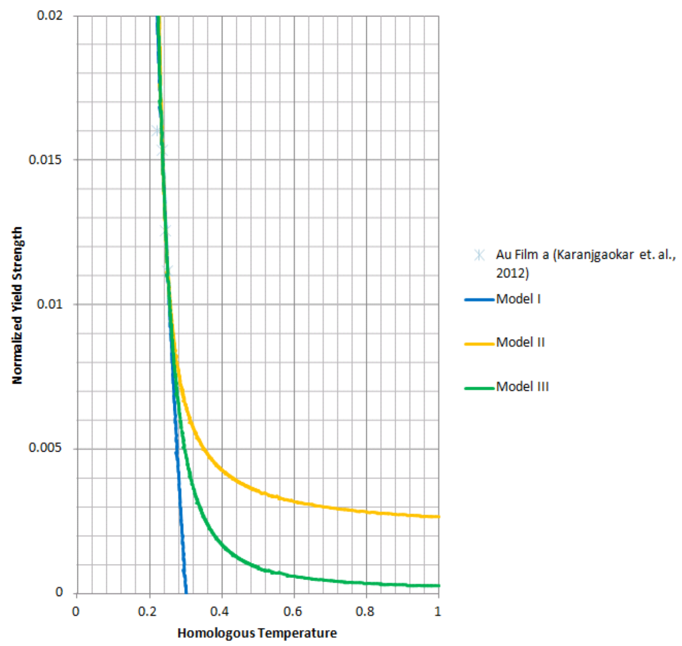

Figure 5-16 Continued

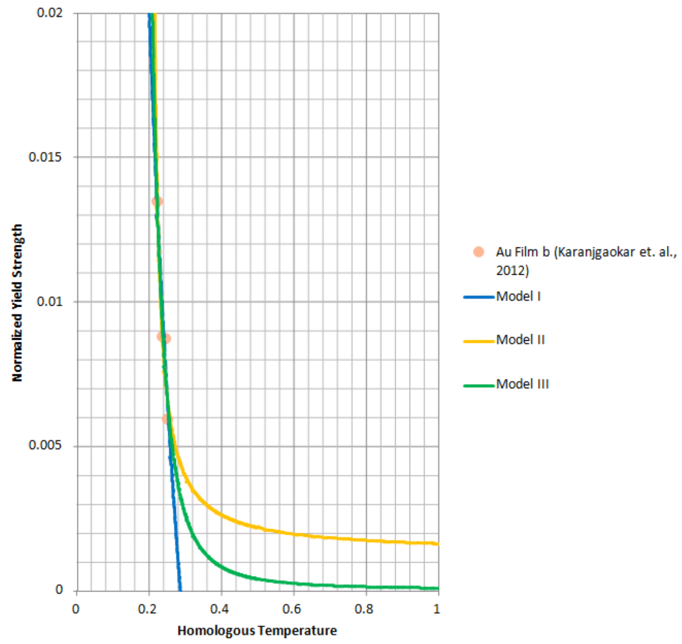

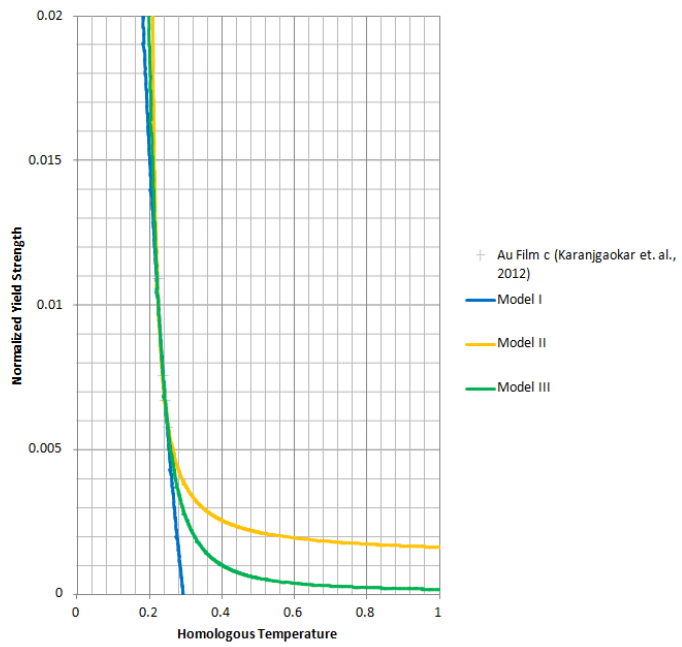

Figure 5-16 Continued

One of the important figures captured in the models is a critical temperature T_c. The temperature where flow stress is no longer temperature-dependence has an important theoretical implication. Theoretically, it can be simply understood as the situation when the 'effective stress', i.e. the (mechanical) work done to overcome local obstacles, is equal to zero. Physically, it can be interpreted as a state when the all immobile dislocations in the structure, which are initially pinned by short-range barriers, have been completely released by a thermal activation mechanism. The stress, by itself, represents the a-thermal component of the flow stress that is independent on the temperature except through the temperature-dependence of elastic modulus. Practically, this part flow stress will remain contribute to the strength of thin film at elevated temperature. With regard to the practical aspects, this critical point is very important in the context of design for reliability.

Despite of its significance, plateau-like behavior may not be obviously and explicitly seen from either the experimental data scatter within the space of interest or the extrapolation of the model equation. In term of describing plateau behavior, proposed model II provides higher value of constant stress compared to the other models (Figure 5-14-Figure 5-16). Model I, on the other hand, consistently defines underestimated values of constant flow stress which are all negatives. Model III defines intermediate positive values between the two extremes.

Theoretically, the approximated critical temperature can be tentatively specified by defining zero gradient of flow stress. The zero gradient of flow stress, however, may not be readily defined from the model. In our case of confined Cu, for example, the gradient of flow stress described by model III ranging from the order of 10^2 to the order of 10^{-3} but never equal to zero. Since flow stress gradients are, in fact, never equal to zero

in all three models being studied, it is important to reinterpret the model and define a critical gradient of the flow stress.

In order to make the relationship simpler Flinn et.al.[7] had proposed an hypothetical temperature (T_F) in association with the critical stress of stress relaxation for a given strain rate and temperature (Eq. 2-45). It was defined as the temperature where the flow stress would equal to zero. In general, it is assumed that some other phenomena took place before the point is reached, including the melting temperature T_M. In attempts to develop minimal model of dislocation dynamics, Langer et.al.[110] have thermodynamically redefined an activation temperature associated with a potential well of depth in the absence of an external stress. In fact it might be greater than melting temperature but should be much smaller than that associated with the energy required to form a dislocation. From a practical point of view, the idea seems to be less plausible and applicable.

Another critical feature that is expected to be captured from the observed behavior is the mechanical threshold stress (MTS), i.e. the appeared measurable stress corresponding to the threshold energy of the thermal activation region that is used as the internal state parameter. None of the three models, however, readily defines a reasonable value of back-extrapolated threshold stress. The extrapolated MTS of Model I and III in confined Cu, for example, are around 9 times higher in magnitude than corresponding shear modulus. This unusual value cannot be explained by the established theories. The realistic values of normalized stress that cover all materials are 10^{-8} – 1[97].

One of the best-available attempts to define a realistic MTS is by back-extrapolating a rather poor fitted function representing typical behavior. The general approximation (R^2=0.5271) gives a value of 0.0774μ(3258.448MPa). Referring to

Kocks[64], MTS could be experimentally measured by excluding the range of temperature below the Zone II (<0.04T_M) and constructing $\sigma^{\frac{1}{2}} vs. T^{\frac{2}{3}}$ plot. Back-extrapolating the normalized data of confined materials in such a way (R^2=0.589) results in a value of 0.02305μ (1382.129 MPa). It can be learned from the general estimation that the MTS should be in the order of 10^3.

Despite it seems to be theoretically sound, the measurements and determination of MTS are not a straight forward practice. In fact, the measurement of flow stress at temperature below 76K has never been reported due to some technical reasons. The determination of MTS is practically very much dependent on the extrapolation of the stress to absolute zero. Earlier study of the behavior of Bulk Copper[72,111], for example, has demonstrated such rigorous procedures and complexities related to the chosen thermal-activation law, empirical parameters, and strain-rate sensitivity as well as estimation of a-thermal stress.

Nevertheless, the capability to predict extrapolated and interpolated values without expecting too much error is one of the key attributes of a sound model. Attempts are required to reinterpret the model and underlying principles with particular reference in the area close to absolute zero.

Despite of the problems attached to the models being developed, a linearized equation is inherently better and more advanced than a polynomial equation, at least for three reasons[104]. Firstly, the proper choice of the curve will provide a physical-mechanistic insight on the experimental data. Secondly, the manipulation of the curve can be more soundly performed, involving differentiation, integration, interpolation, and extrapolation. Thirdly, fewer numbers of parameters are required for estimating value. These characteristics are very important in developing a physically sound model with a vivid underlying mechanism.

One of the major concerns in using this type of equation is the effect of the linearization to its statistical properties. There are extensive dispute with regards to the least-square analysis. Klucka and Kubacek[112], for example, argued that the ordinary least-square (OLS) estimator were constructed based on the normal distribution and homoscedastic assumption of the parameter vectors. It was conceptually demonstrated that the logarithmic transformation alters error distribution effectively. As a result, the initial homoscedastic observation vector became clearly heterocedastic. It was concluded confidently in ref.[112] that generalized a least-square (GLS) estimator must be replaced by OLS whenever a linear regression over a non-linear equation was selected. Sundenberg[113], quite differently, presented a scientific argument supported with empirical data, for staying with the constant variance in the analysis and only performing model fit to the data check for unrealistic results.

Model to data fit check of the Linearized Log-Reciprocal Model (Proposed Model III) to confined Cu data, for example, have indicated that the un-weighted constant variance can reasonably be used to analysis the parameter (Figure 5-17).

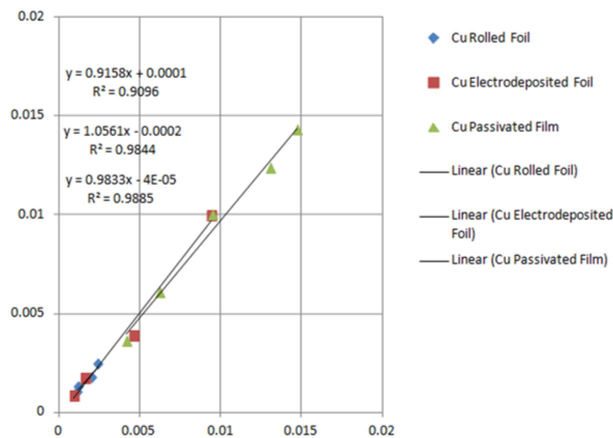

Figure 5-17 Model to data fit check of linearized logarithmic reciprocal model (model III check to confined Cu data)

Adding some complexities, the linearized merit function $\ln f(x) = a + \frac{b}{x}$ is not specifically related to the functional form $f(x) = \exp\left(a - \frac{b}{x}\right)$ or $f(x) = \exp\left(a + \frac{b}{x}\right)$, but also $f(x) = a\exp\left(\frac{b}{x}\right)$. Another established variance of the temperature-dependent equation is $f(x) = ax^b \exp\left(-\frac{c}{x}\right)$ [100,114-116]. On the other side, the Arrhenius type equations may also empirically fit in $\ln f(x)\ v.s..\ T$ and $\ln f(x)\ v.s..\ \ln T$ in addition to $\ln f(x)\ v.s.\ \frac{1}{T}$ [115]

Another concern related to the Arrhenius types of equations is highly correlated parameters of the experimental data. Schwaab et.al.[117,118] have revealed the established method of the re-parameterization of the Arrhenius equation involving problems with single and multiple constants. Mathematical manipulations can basically be done by introducing an optimum reference temperature.

Model Development and Evaluation

Referring back to the foundation for the model (Eq. 3-1), the two most recommended models of ours can be intentionally re-written as:

$$\sigma(T) = \sigma_a(\mu(T)) + \hat{\sigma}\frac{1}{T} \qquad 5\text{-}1$$

$$\sigma(T) = \sigma_a(\mu(T)) + \hat{\sigma}\exp\frac{-\Delta G}{kT} \qquad 5\text{-}2$$

Models to data fit of the two recommended models have been depicted in the Fig. 5-7 – Fig. 5-15 in normalized frame of reference ($\frac{\sigma(T)}{\mu(T)} vs. \frac{T_M}{T}$). In order to get an insight into the physical origin and operating mechanism of the behavior, the equations

must be transformed from its original coordinates into the normalized coordinates so that physical parameters can be readily derived and interpreted from the constitutive models.

Normalizing with relevant physical parameters and rearranging the variable components on the right hand side of the equations, the first model (Eq. 5-3) can be re-written as motivated (Eq. 3-1).

$$\frac{\sigma(T)}{\mu(T)} = \frac{\sigma_a(\mu(T))}{\mu(T)} + \hat{X}\frac{T_M}{T} \qquad \text{5-3}$$

It can be seen that the homologous temperature functions can be simply interpreted as a scaling factor of the non-linear decrease of flow stress from its maximum value to its minimum. Based on this simple analysis, a physical parameter can be readily obtained from the plot of normalized strength vs. reciprocal of homologous temperature. The intercept of the line defines a-thermal component of flow stress normalized by the shear modulus. The flow stress is related to the interaction of dislocations with long-range barriers. This internal stress can be confirmed directly or indirectly from the experiments based on flow stress measurement at a constant strain-rate or stress relaxation[69]. It was also learned from the dimensional check that the Eq.5-3 is physically sounder than the Eq. 5-1. One of the drawbacks of this simple equation is that it does not reflect explicitly the Boltzmann Statistics of the Thermal Activation process.

Transforming Eq.5-2 from original $\sigma(T) - .T$ system into the $\sigma(T)/\mu(T) - .T/T_M$ system, one may write:

$$\frac{\sigma(T)}{\mu(T)} = \frac{\sigma_a(\mu(T))}{\mu(T)} + \hat{X}\exp\frac{-\Delta G}{k}\frac{T_M}{T} \qquad \text{5-4}$$

One of the important problems of this equation is that the physical dimension of the exponential term is not plausible. It was known that the exponential term in a constitutive equation should be set dimensionless in order to physically sound, which was

not the case in 5-4. To make Eq.5-4 physically sounder, a new constant need to be introduced.

To achieve the target we have to define an effective temperature that reflects the energy required to change an equilibrium state into the activated state (free energy of activation), which is a function of obstacle energy and effective stress. The temperature, T_{tact} is defined as:

$$T_{tact} = \frac{\Delta G}{k} = \frac{T_M}{k_{RSD}} \quad \text{5-5}$$

By defining the temperature and constant, we reserved the physical meaning of the equation as well as the dimensional correctness of the exponential term in the new frame of reference (normalized coordinate system).

$$\frac{\sigma(T)}{\mu(T)} = \frac{\sigma_a(\mu(T))}{\mu(T)} + \widehat{X} \exp \frac{-T_M}{k_{RSD} T} \quad \text{5-6}$$

Because of the high correlation between parameter as well as the multi-interpretation of $\ln \frac{\sigma(T)}{\mu(T)} vs. \frac{T_M}{T}$ plot, additional arrangements are required to extract the real parameter. Rearranging Eq. 5-6, one may assume Eq. 5-7.

$$\ln\left[\frac{\sigma(T)}{\mu(T)} - \frac{\sigma_a(\mu(T))}{\mu(T)}\right] = \ln \widehat{X} - \frac{1}{k_{RSD}} \frac{T_M}{T} \quad \text{5-7}$$

Provided $\frac{\sigma_a(\mu(T))}{\mu(T)}$ is well defined, k_{RSD} can be obtained directly from the slope(b) of *y=a+bx* line. The activation energy can be derived from the constant.

Assuming Eq.5-3 and Eq. 5-4 are nested and complimentary three key parameters can be specified and estimated from the two models by linear regression analysis.

Table 5-1 Physically sound parameters obtained from the models

Material	Normalized A-thermal Stress Component $\sigma_a(\mu(T))/\mu(T)$ Eq.5-3	Assumed Normalized Internal State Parameter $\widehat{X}$ Eq.5-3	Assumed Normalized Internal State Parameter $\widehat{X}$ Eq.5-4	Normalized Gibbs Free Energy of Activation $-1/k_{RSD}$ Eq.5-4
Cu Rolled Foil	-0.0003±0.0005	0.0006	0.0007	0.3085+0.0769
Cu Edeposited Foil	-0.0080 ±0.0023	0.0037	0.0044	0.2924+0.0402
Cu Passivated Film	-0.0209± 0.0023	0.0090	0.0127	0.2528+0.0127

It can be seen from the Table 5-1 that the assumed normalized internal state parameters obtained from Eq. 5-3 and Eq. 5-4 is similar in one order of magnitude. These facts indicated that our assumption is not unacceptable. The most important different between two models is that in the first model (Eq. 5-3), the internal parameter is scaled directly by the (normalized) reciprocal homologous temperature whereas in the second model (Eq. 5-4) it is scaled by an exponential factor involving the reciprocal of homologous temperature and stress-dependent Gibbs Free Energy of Activation. To find the exact correlation between the two model equations Eq. 5-3 can be re-written as:

$$\frac{\sigma(T)}{\mu(T)} = \frac{\sigma_a}{\mu(T)} + \widehat{X}\, k_{CUK} \frac{T_M}{T} \qquad 5\text{-}8$$

k_{CUK} is a constant that provides physical relationship between the two equations:

$$k_{CUK} = \frac{T}{T_M} \exp\left(\frac{T_M}{T} \frac{-1}{k_{RSD}} \right) \qquad 5\text{-}9$$

Our simple models assumed 3 key parameters. The parameters in these basic models can be physically discriminated into those related to the *long-range order* and *short-range order* stress fields. The entire mechanism of producing a macroscopic plastic deformation is assumed to be driven by the sum of the athermal and thermally-

activated processes of dislocation lines overcoming obstacles. In the thermal part, the release of *pinned dislocation* can be considered as *a critical gate* for the *dislocation gliding*, *a conditio sine qua non* for noticeable permanent deformation. Alternatively, the local obstacles can also be thought as *the weakest chain* of the entire system. This gives an idea on how a local mechanism drives a global behavior.

Two *key parameters* of the *local thermally activated mechanisms* are explicitly proposed in the foundation for the model involving (1) an *internal state parameter* (short-range barrier controlled characteristics structure) and (2) *a depinning rate factor* containing the Arrhenius type *equations* (Boltzmann probability of successful event and the attempt frequency). The energy and hence the force required to initially start total long-range glide will be effectively controlled by (1) the number of pinned dislocation and (2) the strength of obstacles in addition to the long-range order barriers.

While the more complex model (5-4) explicitly contained both of thermally-activated key parameters, the simpler model (5-3) has only one that is explicitly defined.

Despite of its simplicity, equation (5-3) is superior in defining the plateau stress as it can be exactly obtained from the intercept of the curve while also predicting the internal state parameters. To compensate the deficiency of this basic equation in discriminating the two parameters related to the local thermally activated mechanism, a constant k_{CUK} has been introduced. Equation (5-4), on the other hand, despite of its adequacy of discriminating the two parameters, has need of the plateau stresses to be well defined. In term of practical use, two models are complimentary in giving more accurate estimated parameters.

It can be seen from the results in Table 5-1 that the *normalized internal state parameters* assumed from (5-3) and (5-4) is similar in one order of magnitude. These facts indicate that our initial assumption is not unacceptable. It can be more confidently

assumed that (5-3) and (5-4) are *nested models*. The most important disparity between two models is that in (5-3) the internal parameter is simply attenuated by the reciprocal of normalized temperature whereas in (5-4), it is attenuated by an exponential term involving Boltzmann probability function. Since (5-3) does not contain explicitly the Boltzmann function we introduced a constant that can physically be interpreted as in (5-4).

$$k_{CUK} = \frac{T}{T_M} \exp\left(\frac{T_M}{T} \frac{-1}{k_{RSD}} \right) \qquad 5\text{-}10$$

Not only did our new constant k_{RSD} relate the melting temperature T_M to physically sounder temperature T_{tact}, it also eliminated the dimensional problem of using conventional energy of activation parameter terms ΔG with normalized independent variables.

Non local parameter in the basic structure is related to the interaction of gliding dislocation with long-range internal stress field. Although the normalized parameter values of the bottom stress were readily obtained from (5-3), they are not soundly self-explained. The values of plateau stress derived from (5-3) are all negative and so are those obtained from non-linear regression. These *non-sensible* results might be either reinterpreted statistically as 0 (insignificant parameter) or mechanically as (residual) compressive. Another speculative explanation is that they may be caused by the averaging of micro-mechanisms which involves internal short-range and long-range stress fields whose number and proportion should be significantly altered by dimensional constraints.

It can be seen from Table 5-1 that the standard error for the plateau stress is large for all data points larger than an order of magnitude (the parameter should at least

larger than approximately 2.5 times of the absolute error). Large error simply means that this parameter was basically not known quite well. In extreme case, since all linear x terms are multiplied by the coefficient, it is statistically sound to replace it with 0.

Although no single data point used in model to data fit is zero or less, we may assume from the process history of sample and specimen preparation and testing method that a little amount of residual compressive stresses might not be completely removed by the pre-testing procedure.

Also, as had been discussed in previous chapter, the long-range stress field may at a particular condition have a negative value. Since the macroscopic behavior in small volume materials is only averaged over a small cross section, this might become important.

Constraining the parameters was able to results in non negative value of plateau stress but yet the value is too small to be interpreted as non zero parameter.

Despite the proposed two basic models and the corresponding model prototype fits well with the experimental data of small volume Cu of various ranges of arguments, the physical interpretation of the obtained parameters did not readily explain the assumed mechanism. The application of the models to more global data sets of small volume materials less than 5000nm failed to converge into best fit sensible parameters in most general cases.

Regardless of the shortcomings of the two basics models, they have been able to provide insight into the process and mechanism behind the analysis, which are consistent with our initial assumption. More importantly, assuming them as nested and complementary, physically sound initial parameters can be obtained for more advanced regression analysis.

More advanced and plausible model, increased data points, and wider range of arguments should hypothetically provide more obvious explanation. This, however, requires a more careful and critical formulation of the merit function.

With respects to the physical mechanism, the derivation and interpretation of activation energy is very significant. In MTS model, as it had been discussed previously, the activation energy is assumed to be stress-dependent and hence temperature-dependent since the flow stress varies with temperature. The stress-dependence of activation energy flow stress had been empirically specified by an empirical relationship between the applied mechanical work and thermal activation energy.

Assuming an Arrhenius rate equation with a constant parameter of activation energy, the energy is practically the slope of an Arrhenius plot $\ln \dot{\varepsilon}(T)\ vs\ \frac{1}{T}$.

$$\dot{\varepsilon}(T) = \dot{\varepsilon}_0 \exp\left(\frac{-\Delta G}{kT}\right) \qquad \text{5-11}$$

The value, by its experimental definition, is given by the following differential form of Eg. 5-8.

$$\frac{-\Delta G}{k} = T^2 \frac{d \ln \dot{\varepsilon}(T)}{dT} = \frac{d \ln \dot{\varepsilon}(T)}{d\frac{1}{T}} \qquad \text{5-12}$$

Full derivation of the equation allowing both ΔG and $\dot{\varepsilon}_0$ to be temperature-dependent:

$$\frac{-\Delta G(T)}{k} = \frac{d \ln \dot{\varepsilon}(T)}{d\frac{1}{T}} = \frac{d \ln \dot{\varepsilon}_0(T)}{d\frac{1}{T}} + \frac{1}{k}\left(\Delta G(T) - T\frac{d\Delta G(T)}{d\frac{1}{T}}\right) \qquad \text{5-13}$$

In the view of experimental definition of Eq. 5-8, $\dot{\varepsilon}_0(T)$ and $\Delta G(T)$ are related:

$$\frac{d\ln\dot{\varepsilon}_0(T)}{dT} = \frac{1}{kT}\frac{d\Delta G(T)}{dT} \tag{5-14}$$

Historically, activation energy was understood as the required amount of energy to convert the reacting substance into its "active" form. It is generally accepted that for high energy "reaction" it can be interpreted as a measure of threshold energy. For low energy, however, it is fundamentally differed from the threshold energy. In the context of plastic deformation by thermal activation of dislocation line overcoming obstacles mechanism, it was clearly discussed in Chapter 2 that the activation energy is not equal to the threshold energy of the low energy short-range barriers, which is a combined contribution of mechanical stress and thermal energy of activation. For that reason, mechanical threshold stress had been more conveniently defined. The relationship between the free energy of activation and the threshold energy can be defined empirically as discussed in Chapter 2 (Eq. 2-12, 2-13, and 2-44).

With respect to the long-range barriers, the effective mechanical energy is much lower than the threshold energy of the high energy long-range barriers. In this case, the threshold energy can be assumed to be equal to the activation energy. In reality, the threshold energy is very much higher that can never be overcome by thermal energy (see Fig. 2-5).

One of the most significant advantages of our simplified models (Eq. 5-4) is that the energy of activation was assumed to be invariant and hence it can be derived from the yield strength – temperature data without necessarily defining strain rate as a function of temperature. The model has find the middle ground of the facts that in many polycrystalline materials, the yield strength are not significantly affected by the rate of deformation and the underlying principles that dislocation glide is a kinetic process. The assumption had differentiated the simplified model from the MTS model.

Reference (Physical) Model

Assuming the constant energy of activation, a general model can be originally derived to describe and predict accurately the flow behavior metals at different testing temperature. The assumption is more physically sound in the normalized framework when the reference energy is linked to the reference temperature. In this particular situation, the energy is redefined as a reference constant energy that characterizes the local mechanism process independent of the rate and material characteristics.

$$\frac{d(\sigma/\mu(T))}{d(T/T_M)} = \exp\left(\dot{\varepsilon}_0' + \frac{\Delta G}{k}\frac{T_M}{T}\right) \qquad 5\text{-}15$$

Based on above assumption, a general relationship of flow stress and temperature can be expressed in the form of:

$$y = \int \exp\left(a + \frac{b}{x}\right)dx$$
$$y = x\exp\left(a + \frac{b}{x}\right) - \exp a\, b\, Ei\left(\frac{b}{x}\right) \qquad 5\text{-}16$$

where,

$$Ei(x) = \int_x^{\infty} \frac{e^{-u}}{u}du,\ x > 0 \qquad 5\text{-}17$$

Series of expansion at two extremes are defined as follow

$$at \quad x = 0,$$

$$\frac{1}{2}e^{a}\left(e^{\frac{b}{x}}\left(-2x+O\left(x^{2}\right)\right)+e^{\frac{b}{x}}\left(2x+O\left(x^{2}\right)\right)-2i\pi b\left[\frac{-\arg\left(-\frac{1}{b}\right)-\arg(x)+\pi}{}\right]\right)+$$

$$2i\pi b\left[\frac{-\arg\left(\frac{1}{b}-\arg(x)+\pi\right)}{2\pi}\right]+2i\pi h\left[\frac{-\arg(-b)+\arg(x)+\pi}{2\pi}\right]-$$

$$2i\pi b\left[\frac{-\arg(b-\arg(x)+\pi)}{2\pi}\right]-b\log\left(\frac{1}{b}\right)+b\log\left(\frac{1}{b}\right)+b\log(-b)-b\log(b)$$

$$at \quad x = \infty$$

$$e^{a}x-\frac{1}{2}e^{a}b\left(-\log\left(\frac{1}{b}\right)+\log(b)+2\left(\log\left(\frac{1}{x}\right)+\gamma-1\right)\right)-\frac{e^{a}b^{2}}{2x}+O\left(\left(\frac{1}{x}\right)^{2}\right) \qquad 5\text{-}18$$

where:

$\arg(x) =$ the complex argument

$[x] =$ the floor function

$\log[x] =$ the natural logarithm

$\gamma =$ the Euler

The derivation of this original basic (2 parameters) merit functions allow us to define exactly the two key parameters of the Arrhenius type equation directly from the flow stress – temperature relationship.

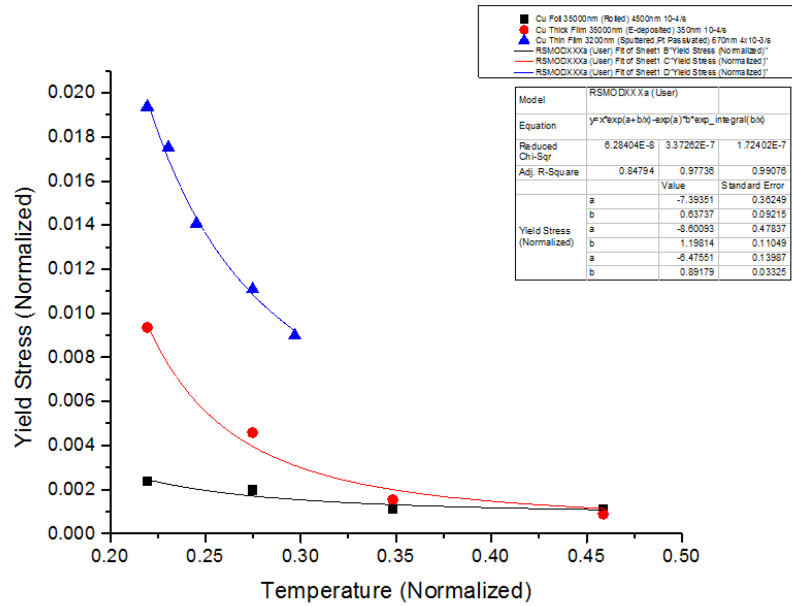

Figure 5-18 Model to data global fit to small volume Cu

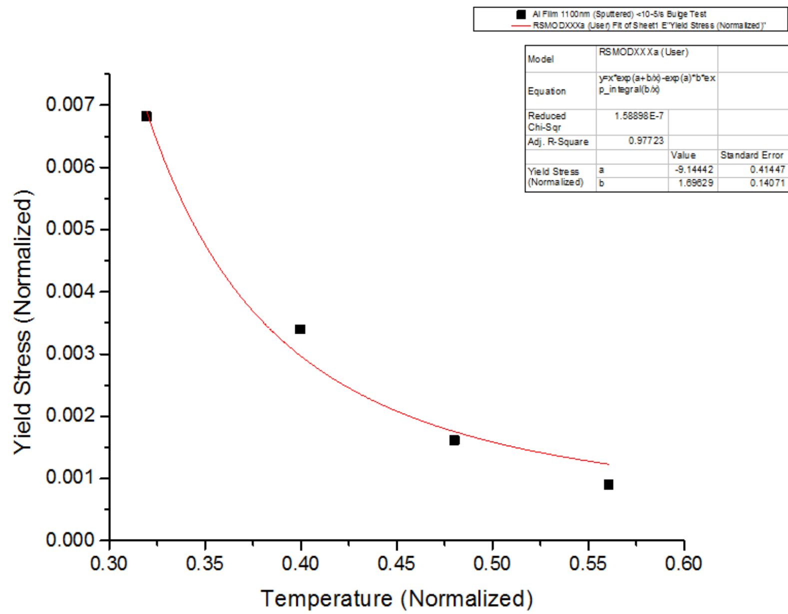

Figure 5-19 Model to data global fit to small volume Al

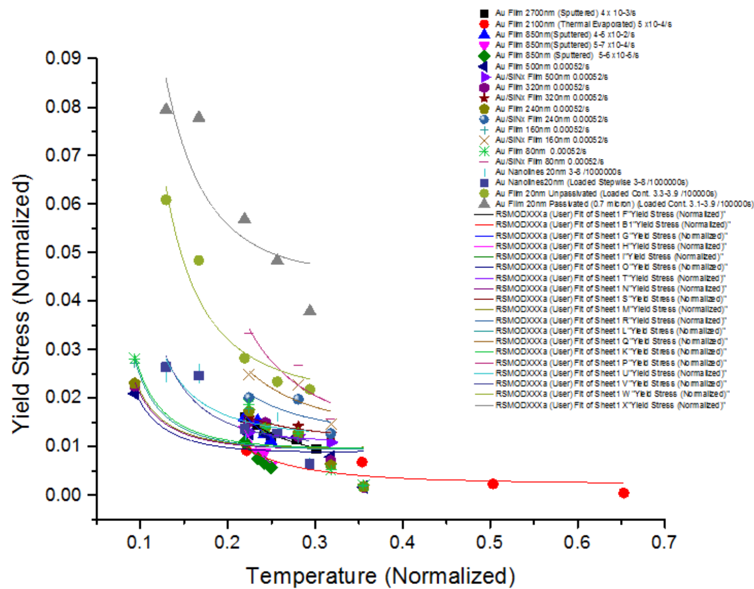

Figure 5-20 Model to data global fit to small volume Au

In general, assuming a constant energy of activation and Arrhenius type rate equations, not only can the original simplified model be used to model temperature-dependence of flow stress in small volume Cu but also Al and Au at all thickness range below 5000 nm.

A more exact solution for the original model can be assumed by defining best estimate value of an obstacle characteristic constant. Accommodating the geometrical parameter of obstacles, model for temperature-dependence of flow stress can be more precisely written in the form of:

$$\int_{\sigma_a}^{\sigma} d(\sigma(T)/\mu(T)) = \int_{T_c}^{T} \exp\left(\dot{\varepsilon}_0^{'} + \frac{\Delta G(T)}{k}\frac{T_M}{T}\right) d(T) \qquad \text{5-19}$$

$$\sigma(T)/\mu(T) = \sigma_a(\mu(T))/\mu(T) + \int_{T_c}^{T} \exp\left(\dot{\varepsilon}_0^{'} + \frac{\Delta G(T)}{k}\frac{T_M}{T}\right) d(T) \qquad 5\text{-}20$$

In order to solve the problem analytically, the energy of activation, which varies with flow stress, must be redefined to be a function of Temperature independently. The relationship is shown in Eq.5-21 where p and q are the characteristics of short barriers.

$$\frac{\Delta G^*}{\Delta F} = \left(1 - \left(1 - \left(\frac{T}{T_c}\right)^p\right)^q\right) \qquad 5\text{-}21$$

Equation 5-20 then can be re-written as:

$$\sigma(T)/\mu(T) = \sigma_a(\mu(T))/\mu(T) + \int_{T_c}^{T} \exp\left(\dot{\varepsilon}_0^{'} + \frac{-\Delta F}{kT}\left(1 - \left(1 - \left(\frac{T}{T_c}\right)^p\right)^q\right)\right) d(T) \qquad 5\text{-}22$$

The equation can be mathematically re-written as Equation 5-23,

$$\int_{c}^{x} \exp\left(a + \frac{b}{x}\left(1 - \left(1 - \left(\frac{x}{c}\right)^p\right)^q\right)\right) dx \qquad 5\text{-}23$$

By this time, however, the mathematical solutions for the problem have not been available.

Assuming q=1 will result in:

$$\int_{c}^{x} \exp\left(a + \frac{bx^{p-1}}{c}\right) dx \qquad 5\text{-}24$$

The problem is mathematically solved as:

$$\frac{e^a x\left(-\frac{bx^{p-1}}{c}\right)^{\frac{1}{1-p}} \Gamma\left(\frac{1}{p-1}, \frac{-bx^{p-1}}{c}\right)}{1-p} \qquad 5\text{-}25$$

Where:

$\Gamma =$ gamma function

Reference (Empirical) Model

A purely geometric-based model was derived as a reference model. The model is depicted as follow:

$$\frac{\sigma}{\mu(T)} = \frac{\sigma_a(\mu(T))}{\mu(T)} + \widehat{X}\left(1-\left(\frac{T}{\chi_{RSD}T_M}\right)^{\frac{1}{q}}\right)^{\frac{1}{p}} \qquad 5\text{-}26$$

The p and q coefficients are empirical constants that represent the geometric relationship of the temperature-dependence of flow stress. The physical meaning of the equation can be derived from the two parameters representing top and bottom threshold stress.

In the case of small volume Cu the two parameters model describes and predicts the behavior better than geometrical-based data with assume value of obstacles characteristics constants that works in most metals being under investigation. The comparison is depicted in Figure 5-21. No statistical analysis is demanded two compare the results since a less parameter sensible model with better goodness of fit, lower standard of errors, and higher level of confidence, had been self-explained.

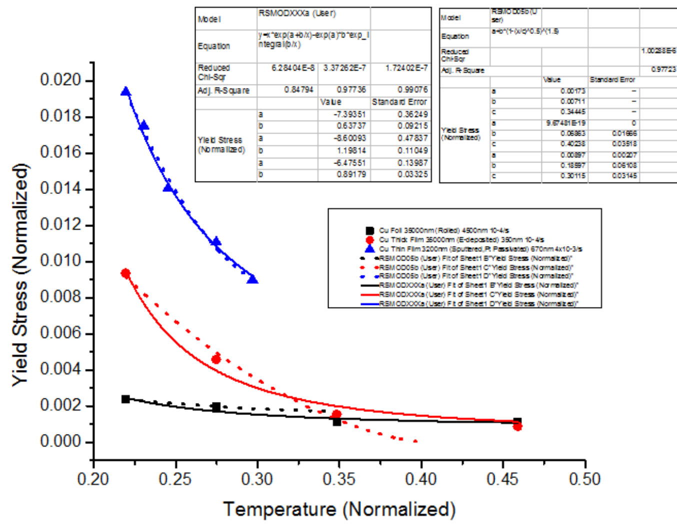

Model	RSMODXXXa (User)		
Equation	y=x*exp(a+b/x)-exp(a)*b*exp_Integral(b/x)		
Reduced Chi-Sqr	6.28404E-8	3.37262E-7	1.72402E-7
Adj. R-Square	0.84794	0.97736	0.99076
		Value	Standard Error
Yield Stress (Normalized)	a	-7.39351	0.36249
	b	0.63737	0.09215
	a	-8.60093	0.47837
	b	1.19814	0.11049
	a	-6.47551	0.13987
	b	0.89179	0.03325

Model	RSMOD05b (User)			
Equation	a+b*(1-(x/c)^0.5)^(1.5)			
Reduced Chi-Sqr				1.00288E-6
Adj. R-Square				0.97723
		Value	Standard Error	
Yield Stress (Normalized)	a	0.00173	--	
	b	0.00711	--	
	c	0.34445	--	
	a	9.67481E-19	0	
	b	0.06863	0.01666	
	c	0.40238	0.03518	
	a	0.00897	0.00207	
	b	0.18597	0.06108	
	c	0.30115	0.03145	

Dashed Line: Geometric-based Model (3 Parameters)
Solid Line: RSD-Original Model (2 Parameters)

Figure 5-21 Comparison of the two models

Exponential Decay Model

Our exponential decay model simply assumes that the temperature-dependence of flow stress is governed by the release of pinned dislocation with the aid of thermal activation. The initial stress represents both the initial quantities and qualities of pinned dislocations within the structure. Rate of breakdown is inversely proportional to the energy of activation divided by the temperature, which can also be interpreted as the probability of a successful thermal activation occasion.

Flow stress is defined as the onset of plastic deformation without elastic deformation being included. It is related to the glide of dislocation overcoming obstacles. Multiple dislocation pinning mechanisms may exist within the structure. Dislocation will

glide when the applied stress exceeds a critical stress for gliding by each single mechanism.

Total plastic strain is assumed to be the sum of all dislocation glide.

$$\varepsilon_p = \sum_i \varepsilon_i \tag{5-27}$$

Applying Hooke's law, the expression can be re-written to articulate the flow stress:

$$\frac{\sigma_y}{\mu} = \sum_i \frac{\sigma_i}{\mu} \tag{5-28}$$

Knowing that the entire glide involves a-thermal and thermal process, a general expression of flow stress can be written in the form of:

$$\frac{\sigma_y}{\mu} = \frac{\sigma_a}{\mu} + \sum_j \frac{\sigma_j}{\mu} \tag{5-29}$$

Exponential decay model assume that the flow stress exponentially decreases in the amount of $\Delta\sigma$ from the threshold stress, to the a-thermal plateau stress, σ_a , with a constant rate $\exp - cT$ as illustrate in Figure 5-22. The flow stress temperature relationship is expressed in a 3 parameters equation:

$$\sigma_y = \sigma_a + \Delta\sigma \exp(-cT) \tag{5-30}$$

The a-thermal stress is independent on temperature and strain rate and related to the long-range barrier that may come from grain boundary, surface and interface. The decay amplitude can be physically interpreted as the consequence of pinned dislocation in the structure that can be thermally activated. The rate of decay represents the thermally activated mechanism of gliding, which can be related to the rate of deformation and activation energy.

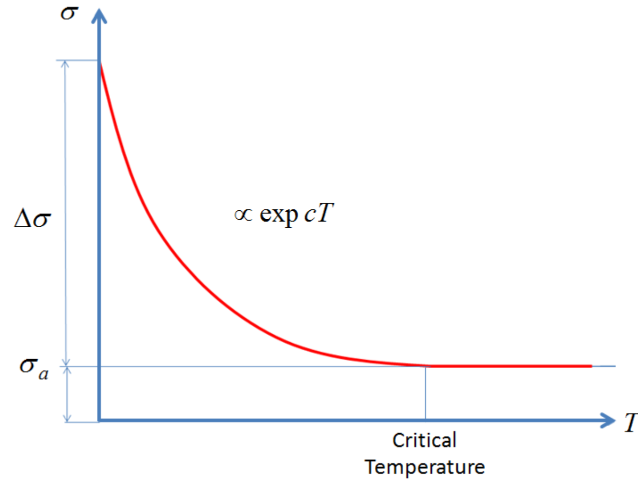

Figure 5-22 Exponential decay model

The model can be written in the form of:

$$\frac{\sigma}{\mu(T)} = \frac{\sigma_a(\mu(T))}{\mu(T)} + \frac{\Delta\sigma}{\mu(T)} \exp\left(c' \frac{T}{T_M}\right) \quad \text{5-31}$$

The physical interpretation of the model parameter can be derived from the connection to the MTS model that had been explained in previous chapter.

$$\frac{\sigma_y}{\mu} = \frac{\sigma_a}{\mu} + \sum_j S_j(\dot{\varepsilon}, T) \frac{\Delta\sigma_j}{\mu_0} \quad \text{5-32}$$

where:

$$S_j(\dot{\varepsilon}, T) = \left[1 - \left(\frac{kT}{\Delta F_j} \ln \frac{\dot{\varepsilon}_0}{\dot{\varepsilon}_j}\right)^{\frac{1}{q}}\right]^{\frac{1}{p}} \quad \text{5-33}$$

Assuming the empirical geometric constants p and q, which represents the non-ideality of the shape and distribution of obstacles, are equal to unity Taking j=1 to account only single thermal mechanism exists, a simplified relationship can be written in a power law relationship.

$$\frac{(\sigma_y - \sigma_a)/\mu}{\Delta\sigma_1/\mu_0} \approx \left(\frac{\dot{\varepsilon}_0}{\dot{\varepsilon}_1}\right)^{\frac{kT}{\Delta F_1}} \tag{5-34}$$

From this relationship, the proportionality of the thermal component of the flow stress and the stress decay amplitude can be written as:

$$\frac{(\sigma_y - \sigma_a)/\mu_0}{\Delta\sigma_1/\mu} = \exp\left\{\frac{kT}{\Delta F_1}\ln\left(\frac{\dot{\varepsilon}_0}{\dot{\varepsilon}_1}\right)\right\} \tag{5-35}$$

Key parameter constants c’ in 5-31, therefore, can be readily interpreted as:

$$c' = \left\{\frac{k}{T_M \Delta F_1}\ln\left(\frac{\dot{\varepsilon}_0}{\dot{\varepsilon}_1}\right)\right\} \tag{5-36}$$

It can be seen that the parameter contains information about the material and rate characteristics as well as the obstacles or short barrier characteristics. Model to small volume Cu data fit is depicted in Figure 5-23

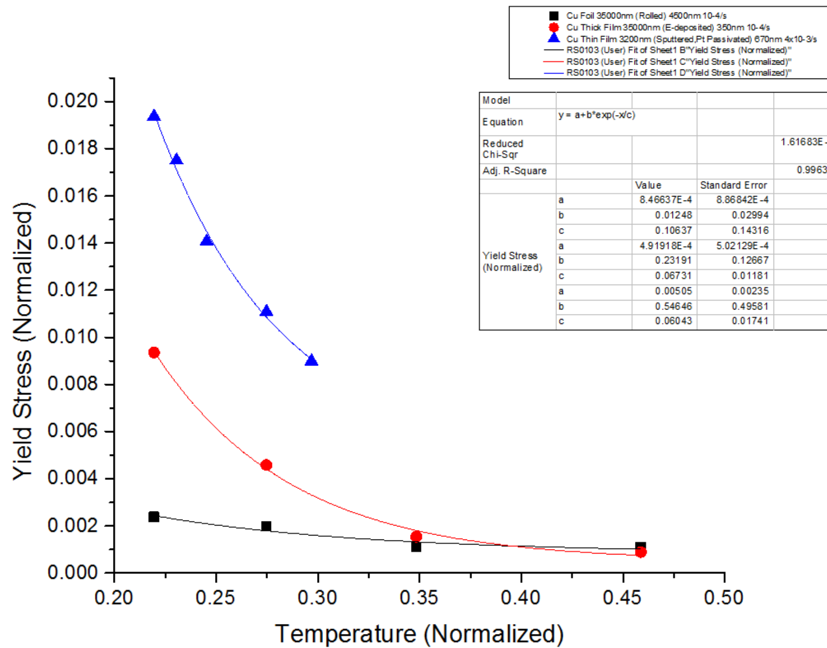

Model				
Equation	y = a+b*exp(-x/c)			
Reduced Chi-Sqr				1.61683E-7
Adj. R-Square				0.99633
		Value	Standard Error	
Yield Stress (Normalized)	a	8.46637E-4	8.86842E-4	
	b	0.01248	0.02994	
	c	0.10637	0.14316	
	a	4.91918E-4	5.02129E-4	
	b	0.23191	0.12667	
	c	0.06731	0.01181	
	a	0.00505	0.00235	
	b	0.54646	0.49581	
	c	0.06043	0.01741	

Figure 5-23 Exponential decay model to small volume Cu data global fit

Application of the Exponential Decay Model

In the previous part of discussion we have developed a simple physically sound model that is descriptive and predictive. This model will be employed to explain the temperature-dependence of flow stress in small volume metallic materials from the multiple datasets collected from different published literature. In particular, it will be applied to understand the key dimensional and microstructure factors that affect the flow stress of metallic thin film at different temperatures.

This understanding is very important since metallic thin film is the backbone of many devices and it is generally acknowledge that the mechanism of reliability failure is closely related to the flow stress. On the other hand, the measurement, description, and prediction of flow stress in thin film are challenging.

In general, the measured flow stress in thin films is affected by the testing conditions and geometry of the samples in addition to the microstructures that involves dislocations, solute, and precipitates as well as surface and interface. The simultaneous effect will result in some complexities.

In general, the flow stress behavior in thin film can be described as follows. Firstly, the flow stress in thin film is always higher in thin film compared to that in bulk counterpart. Secondly, in thin flow stress change with temperature more rapidly. There are some critical questions need to be addressed with regards to the flow stress phenomena. What is the mechanism of excessive strength? Is it governed by the surface, interface, grain size or something else? More specifically, what is the role of surface and interface? Is it a strong pinning site as generally assumed? Also, what is the role of grain boundary? Is the strengthening mechanism preserved at extremely small grain? Is the sensitivity to the temperature is consistent with the assumed mechanism of the simplified model?

To address the problem which such a complexity from various scattered data, a few logical assumptions are initially set. Firstly, creep and strain hardening mechanism will not be considered. Since material under investigation is FCC metal with high purity, strengthening by precipitate and probably solute atoms will not be taken into account. As a consequence, only surface/interface, grain boundary, and dislocation density will be taken into the main possibility for strengthening mechanism.

Effect of size parameter can be assumed to affect the key parameters as illustrated in Figure 5-24. *Thickness (h, l)* had been readily identified as a chief *material size-parameter*. Two relevant *micro-structural size-parameters* involve *grain size (d)* (grain boundary) and *obstacle spacing (λ)* (dislocation density). Additional constraints can be derived indirectly from *grain size to thickness* ratio *(d/h)*. Surface/interface conditions had also contributed to the strengthening through out dimension and microstructure respectively.

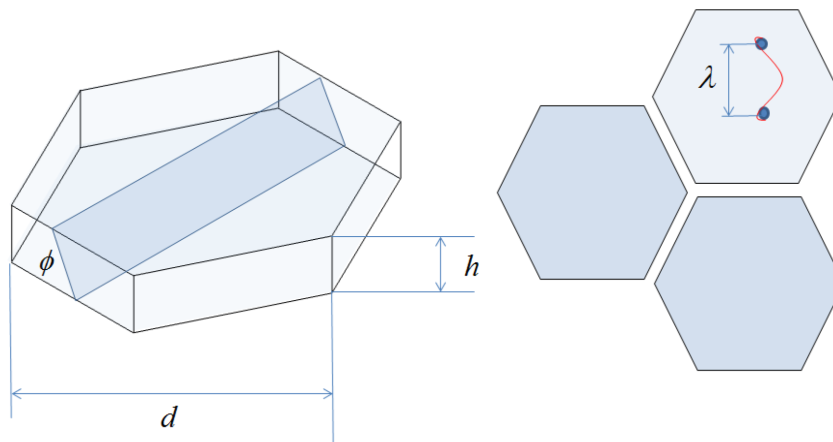

Figure 5-24 Three key size parameters of dimensional and micro-structural constraints

Grain size to thickness ratio can be used as a discriminating factor separating two cases of different arguments. When $d/h > 1$ and $\lambda < d$, it can be reasonably assumed

that dislocation lines will only be pinned at the surface/interface. Effects of grain size in this case can be reasonably ignored leaving alone the material thickness as the main size-parameter.

The thickness contribution to the increase of flow stress had been predicted in previous models for low constant temperature[51,54-59,87]. They are, for example, dependent by the factor of inverse square root of thickness as predicted by *work hardening model*[55] or by the inverse of it as assumed by *force criterion model* [51,54] *and Thompson model* [87]. In *energy criterion model* [56-59], quite differently, the flow stress was predicted to be dependent on the thickness by the by the factor of *1/h log h*.

When d/h < 1, the simplest model assumed that dislocation line is pinned at grain boundaries and both material surfaces/interfaces. In this case material can generally treated as polycrystalline. The contribution of grain size was assumed to be correspondent to its inverse square root as predicted by work hardening model or by its inverse as predicted by the Thompson model.

With respect to our original model, those size-parameters were assumed to be implicitly embedded in the *three parameters*. In facts, it is not a straight forward interpretation as they are interlinked and multifaceted. Comparing our foundations with the earlier models at low constant temperature[51], it is generally sound to assume at this point that dimensional and micro-structural constraints will only affect *geometrically necessary dislocations* (excess of dislocation stored in crystal for deformation compatibility). It means that only the *thermal components of flow stress* will be significantly affected by these constraints. The effects are assumed to be embedded in *depinning parameter* as well as *internal state parameter*. The internal state parameters are assumed to chiefly represent the number of pinned dislocations (*pinned dislocations*

quantity) whereas the depinning factor corresponds to the pinning characteristics (*pinning quality*).

Within the limited data from the scattered experimental arguments, some consistency does exist. The exponential decay model fit reasonably well with most of data sets of small volume materials, with particular reference in the range of thickness larger than 500 nm with some exception. From the general observation, it can be reasonably assumed that the surface does not act as an adequately strong pinning site that maintains its effect with the temperature increase. It can also be generally observed that the role of grain boundary has altered, from the a-thermal to the thermal mechanism.

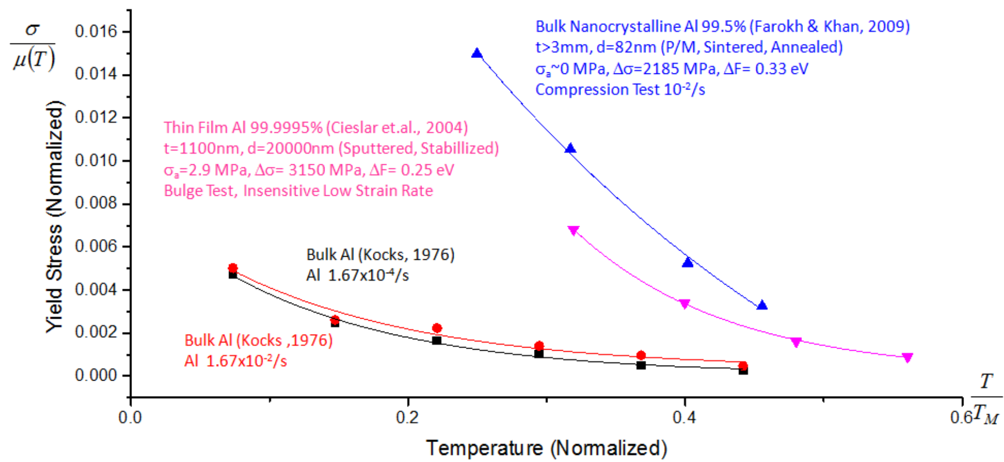

Figure 5-25 Role of grain boundary from Al data sets

It can be seen from Al data sets in Figure 5-25 that the contribution of grain boundary and surface to the a-thermal part of flow stress does not significantly exist in bulk nanocrystalline and thin film with relatively large grain size. Large stress decay amplitude is assumed to be dictated by (1) high density of dislocation in thin film and (2) large number of grain boundary in bulk nanocrystalline. High temperature sensitivity, as

indicated by the activation energy, is related to dislocation density (0.25eV) and grain boundary (0.33 eV).

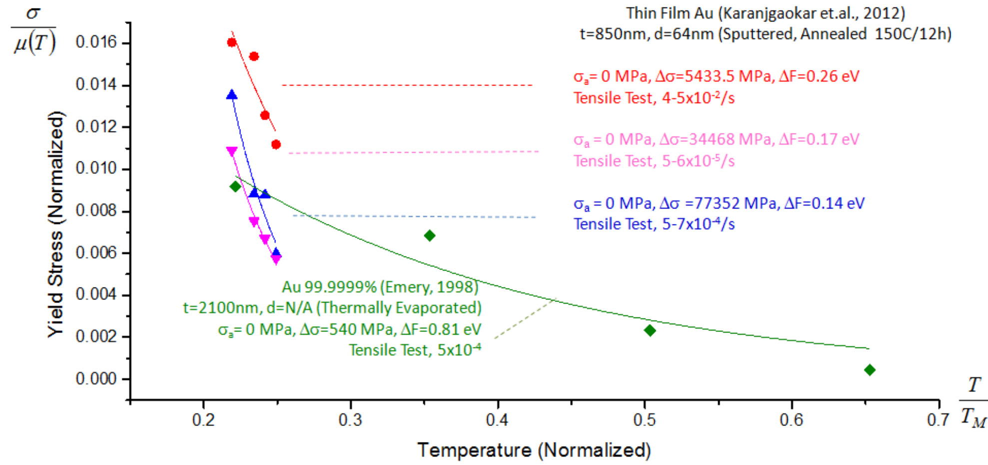

Figure 5-26 Role of surface from Au data sets

Observation of Au data sets have shown that regardless to the strain rate and film thickness, no a-thermal stress was observed in all data sets. This fact, consistent with finding from Al data sets, confirms that surface does not play role in the athermal part of flow stress. It can also be learnt from the figure that the high decay stress amplitude is chiefly dictated by the (1) grain size, and (2) dislocation density.

From the datasets of rolled and electroplated Cu foil, it can also be seen that grain size does not significantly contribute to the athermal stress component. This finding to some extent is consistent with those in Au and Al. Large stress decay amplitude is produced by dislocation density and probably the grain size. Source and mechanism of high a-thermal stress in passivated film is unknown. It can be assumed from the interface created by the passivation but must be confirmed by further investigation.

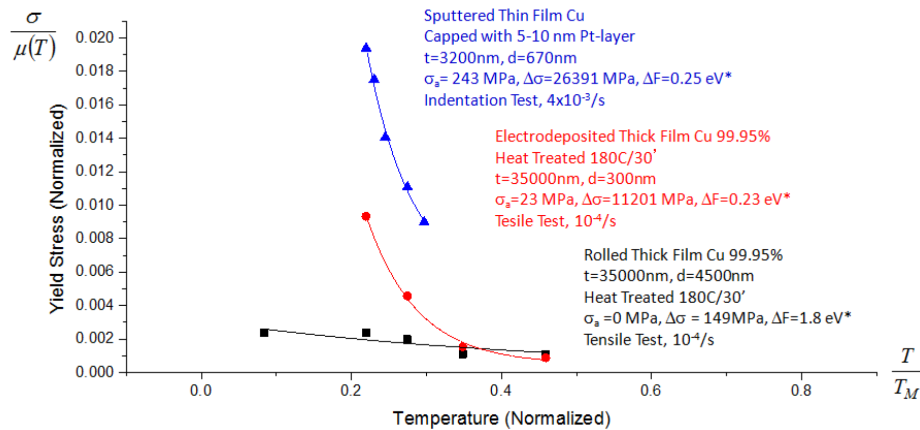

Figure 5-27 Findings from Cu data sets

Some conclusions can be drawn from the general and specific observation of the behavior with the aid of exponential decay model.

Firstly, free surface has negligible influence on the flow stress in thin film as that generally accepted in bulk. This is quite different with the conventional assumption made in the field. The strong effect of interface, however, may remain exist.

Secondly, the strengthening mechanism by grain boundary can no longer be considered as athermal but has altered to the thermal part. This is consistent with recent finding in the field that the conventional Hall-Petch relationship is no longer valid when the size of grain reaches a critical size.

Thirdly, high flow strength in thin film is chiefly dictated by the density of dislocation and grain boundary. In most cases, this are related to the thermal part of the flow stress.

The changing of role of grain size in thin film can be explained by the inverse of Hall-Petch relation. Among other plausible explanation one of them will be discussed here. The first explanation is that the breakdown of the relation takes place at a point

when grain becomes too small to withstand shear stress. As a consequence, dislocation will shear through the entire grain instead of gliding on its slip system. More detailed qualitative and quantitative explanation of the inverse phenomena was found in [119]. Excess volume of interface and interfacial excess energy was specified to characterize the critical point. In the coarse grain, whose excess volume interface and interfacial excess energy are large, dislocation movement is hindered within the grain whereas in extremely small grain size value of excess volume interface and interfacial excess energy are so small that dislocation can pass through several grains. In nano-crystalline grain, not only does a reduction of grain result in an increase of interface fraction but also a reduction of interfacial energy and excess volume interface. A reduction of interfacial excess volume will result in the essential reduction of the ability of grain boundary to impede dislocation. As a consequence the material will soften with the decrease of the grain.

From the perspective of thermal activation process, it can be assumed that the reduction of the interfacial energy and excess volume of interface will result in the feasibility of thermal activation process. When the energy barrier at the boundary is not too high, it can be overcome by thermal activation process. In other words, the role of grain boundary as the long-range barrier has been shifted into the short-range barrier.

One of the interesting points to be address is the limit of the conventional behavior. At low temperature, it had been defined by the condition of dislocation plasticity that *"at least one dislocation loop must fit into an average grain"*[120]. In simple words, it is assumed that the mechanism must be break down when the diameter of smallest loop no longer fit into the grain. So far, the prediction is reasonably agreed with experimental observation in bulk. In thin film however the relationship is not as clear as

in general material. Whether it can be modeled with Hall-Petch relationship with modified constant parameter or should be expressed by different expression remains unclear.

The role of surface had been studied in single crystalline, from which conventional models and understanding were developed. TEM evidences in polycrystalline material, however, are quite differently from the simple assumption. In situ cross-sectional observation of thick polycrystalline Cu film on Si substrate with an amorphous diffusion barrier for instance did not reveal both dislocation impedance and deposition by at the interface/surface. Instead the interface acts as a sink for dislocation. The fading of dislocation contrast at the interface had also supported the argument of interfacial dislocation core spreading.

Our findings have supported the alternative assumptions against the work hardening mechanism that relies on the role of surface pinning and dislocation. We support “bulk-like” behavior theories that the flow stress is controlled by the impendence of internal dislocation whose density increasing with the geometry constraints. Our finding that the characteristic density of pinned dislocation dictating the flow stress is also supported by the evidence of discontinuous dislocation motion as discussed in the theory.

With respect to the role of the surface, we suggested “indirect” effect of surface and interface in increasing flow stress. Instead of pinning the threading dislocation the surface pins the boundary, preventing it from growth. In addition, surface also plays an important role in stabilizing trapped dislocation within the boundary by preventing dislocation annihilation at annealing temperature.

Chapter 6

Conclusion

Typical behaviors of small volume materials are not similar to that of bulk counterparts. Efforts have been made to develop a simple but physically correct and predictive model to understand the flow stress in thin metallic film at different temperature. Exponential decay model-inspired phenomenology approach had been employed to reveal the key factors affecting the behavior and find the direction for more complete constitutive model.

Our exponential decay model can generally describe the behavior at confined dimension. In particular, the model is able to capture, explain, and anticipate temperature sensitivity and strengthening mechanism as well as grain boundary and surface roles. Several points had been drawn from the simplified observation and analysis through the model application. Role of free surface in strengthening is negligible but interface may still important. Role of grain boundary in small volume alters from long-range to short-range order. High density of dislocation and grain boundary are the main source of the high stress in the thermal part. Surface and interface indirectly affect the flow stress by pinning the grain boundary at the surface and stabilizing confined dislocation.

Despite of its physical validity, our model has limitation in explaining all existing data and observed phenomena. Two or more mechanisms may need to be developed within the space of interest. Link to more advanced atomistic model and selected experimental verification may be necessary to improve the model.

References

1. P.L. Castro and J.F. Campbell, Ohmic Contacts to Semiconductor, 323-338 (1969)
2. P.A. Flin, *J. Mater. Res.* **6**, 1498-1501 (1991)
3. A. Katz, S. Nakahara, and M. Geva, *J. Appl. Phys.* **70**, 7342-7348 (1991)
4. A.K. Sinha and T. T. Sheng, *Thin Solid Films* **48**, 117-126 (1978)
5. M. Hershkovitz, I.A. Blech, and Y. Komem, *Thin Solid Films* **130**, 87-93 (1985)
6. M.F. Doerner, D.S. Gardner, and W.D. Nix, *J. Mat. Res.* **1**, 845-851 (1986)
7. P.A. Flinn, D.S. Gardner, and W.D. Nix, *IEEE Trans. Mat. Dev.* **34**, 689-699 (1987)
8. D.S. Gardner and P.A. Flinn, *IEEE Trans. Mat. Dev.* **35**, 2160-2169 (1988)
9. D.S. Gardner and P.A. Flinn *, J. Appl. Phys.* **67**, 1831-1844 (1990)
10. A. Tezaki, T. Mineta, H. Egawa, T. Noguchi, 28th *Annual Int. Rel. Phys. Symp., IEEE Symp. Proc.,* New Orleans, LA, 221-229 (1990)
11. B.L. Draper and Thomas A. Hill, *J. Vac. Sci. Technol.* **B 9**, 1956 (1991)
12. A. Katz, S. Nakahara, and Pvl. Geva, *J. Appl. Phys.* **70**, 7342-7348 (1991)
13. M.D. Thouless, J. Gupta, and J.M.E. Harper, *J. Mater. Res.* **8**, 1845-1852 (1993)
14. C.A. Volkert, C.F. Alofs, and J.R. Liefting, *J. Mater. Res.* **9**, 1147-1155 (1994)
15. A. Witvrouw , J. Proost, B. Deweerdt, Ph. Roussel, K. Maex, *Mat. Res. Soc. Symp. Proc.* **356**, 441-446 (1994)
16. R.P. Vinci, E.M. Zielinski, J.C. Bravman, *Thin Solid Films* **262**, 142-153 (1995)
17. J. Proost, A. Witvrouw, P. Cosemans, Ph. Roussel, K. Maex, *Microelectron. Eng.* **33,** 137-147 (1997)
18. R.M.Keller, S.P. Baker and E. Arz, *J. Mater. Res.* **13**, 1307 1317(1998)
19. Y.L. Shen, S. Suresh, M. Y. He, A. Bagchi, O. Kienzle, M. Ruhle, A. G. Evans, *J. Mater. Res.* **13**, 1928 -1937 (1998)

20. R. Emery, C. Simon, B. Mazin, and G.L. Povirk, *Mat. Res. Soc. Symp. Proc.* **505**, 57-62 (1998)
21. J. Koike, S. Utsunomiya, Y. Shimoyama, K. Maruyama, and H. Oikawa, *J. Mater. Res.* **13**, 3256-3264 (1998)
22. A. Witvrouw, J. Proost, and Ph. Roussel, *J. Mater. Res.* **14,** 1246-1254 (1999)
23. R.M. Keller, S.P. Baker, and E. Arzt, *Acta Mater.* **47**, 415-426 (1999)
24. O. S. Leung, A. Munkholm, S. Brennan, and W. D. Nix, *J. Appl. Phys.* **88**, 1389 (2000)
25. G. Dehm, D. Weiss, E. Arzt, *Mat. Sci. Eng.* **A309–310**, 468-472 (2001)
26. S.P. Baker, A. Kretschmann, and E. Arzt, *Acta Mater*. **49**, 2145-2160 (2001)
27. W. Weihnnacht and W. Bruckner, *Acta Mater.* **49**, 2365-2372 (2001)
28. D. Weiss, H. Gao, and E. Arzt, *Acta Mater.* **49** (2001) 2395–2403
29. B. Weiss, V. Groger, G. Khatibi, A. Kotas, P. Zimprich, R. Stickler, B. Zagar*,* *Sensors and Actuators A* **99**, 172-182 (2002)
30. O. Kraft, L. B. Freund, R. Phillips and E. Arzt, *MRS Bulletin* **27**, 30-37 (2002)
31. E.S. Ege and Y.L. Shen, *J. Electron. Mat.* **32**, 1000-1011 (2003)
32. Y.L. Shen and U. Ramamurty, *J. Vac. Sci. Technol.* **B 21**, 1258-1264 (2003)
33. S. Hyun, W. L. Brown, and R. P. Vinci, *Appl. Phys. Lett.* **83**, 4411 (2003)
34. G. Dehm, T. J. Balk, H. Edongue, E. Arzt, *Microelectron. Eng.* **70**, 412–424 (2003)
35. M. Cieslar, V. Oliva, A. Karimi, J.L. Martin, *Mat. Sci. Eng. A* **387–389,** 734–737 (2004)
36. A.A. Volinsky, N.R. Moody, W.W. Gerberich, *J. Mater. Res.* **19**, 2650 (2004)
37. P.A. Gruber, S. Olliges, E. Arzt and R. Spolenak, *J. Mat. Res.* **23**, 2406 2419 (2008)
38. S. Olliges, S. Frank, P. A. Gruber, V. Auzelyte, K. Kunze, H.H. Solak and R. Spolenak, *Scripta Mater.* **60**, 273–276 (2009)

39. S. Olliges, S. Frank, P.A. Gruber, V. Auzelyte, H. Solak, R. Spolenak, *Mat. Sci. Eng.* **A 528**, 6203–6209 (2011)
40. C.E. Murray, E.T. Ryan, P.R. Besser, C. Witt, J.L. Jordan-Sweet, M.F. Toney, *Microelectron. Eng.* **92**, 95–100 (2012)
41. N.J. Karanjgaokar, C.-S. Oh, J. Lambros, I. Chasiotis, *Acta Materialia* **60**, 5352–5361 (2012)
42. H. Niwa, H. Yagi, H. Tsuchikawa, and M. Kato, *J. Appl. Phys.* **68**, 328 (1990)
43. ASM Handbook Vol. 2 Properties and Selection: Nonferrous Alloys and Special Purpose Materials, 10th ed.
44. M.E. Kassner, *Acta Mater.* **52**, 1–9 (2004)
45. U.F. Kocks, *J. Eng. Sci. Tech*, 76-86 (1976)
46. S. Nemat-Nasser and Y.L. Li, *Acta. Mater.* **46**, 565-577 (1998)
47. B. Farrokh, A.S. Khan, *Int. J. Plast.* **25**, 715–732 (2009)
48. G.R. Johnson and W.H. Cook, *Eng. Fract. Mech.* **21**, 31-48 (1985)
49. D.A. Hardwick, *Thin Solid Film* **154**, 109-124 (1987)
50. P. S. Alexopoulos and T. C. O'Sullivan, *Annu. Rev. Mater. Sci.* **20** 391-420 (1990)
51. M. Ronay, *Phyl. Mag. A* **40**, 145-160 (1979)
52. H.J. Frost, *MRS Proceedings* **265**, 3 (1982)
53. J. W. Matthews, S. Mader, and T. B. Light, J. Appl. Phys. 41, 3800 (1970)
54. T-S. Kuan and M. Murakami, *Metal. Trans.* **13A**, 383-391 (1982)
55. M. Murakami and T-S. Kuan, *Treat. Mat. Sci. Tech.* **24**, 163-210 (1982)
56. L.B. Freund, *J. App. Mech.* **54**, 553-57 (1987)
57. L.B Freund, *Int. J. Sol. Struc.* **37,** 185-196 (2000)
58. W.D. Nix, *Met. Trans. A* **20A**, 2217-2245 (1989)
59. W.D. Nix, *Scrip. Mater.* **39**, 545–554 (1998)

60. C. S. Hau-Riege and C. V. Thompson, *J. Appl. Phys.* **87**, 8467 (2000)

61. O. Kraft, L. B. Freund, R. Phillips and E. Arzt, *MRS Bulletin* **27**, 30-37 (2002)

62. O. Kraft, P.A. Gruber, R. Monig, and D. Weygand, *Ann. Rev. Mat. Res.* **40**, 293–317 (2010)

63. M.F. Ashby, *Mat. Sci. Tech.* **8**, 102-111 (1992).

64. U.F. Kocks, Constitutive Behavior based on Crystal Plasticity, in Constitutive Equations for Creep and Plasticity edited by A.K. Miller, (Elsevier, London, 1987), 1-88.

65. A.S. Argon, Physical Basis of Constitutive Equations for Plasticity in Constitutive Equation in Plasticity edited by A.S. Argon, (The MIT Press, Cambridge, 1975), 1-22.

66. A. H. Cottrell, *Proc. Inst. Mech. Eng. Conf. 1957*, 18 (1957)

67. J. Rosler, H. Harders, and M. Baker, Mechanical Behavior of Engineering Materials: Metals, Ceramics, Polymers, and Composites, Springer, Berlin, 2007

68. U.F. Kocks, A.S. Argon, M.F. Ashby, Thermodynamics and Kinetics of Slip in Progress in Materials Science 19, edited by Chalmers, Christian, and Massalki (Pergamon Press, New York, 1975) 1-288.

69. H. Conrad, *Mater. Sci. Eng.* **6**, 265-273 (1970).

70. C. Zener and Z.A. Hollomon, *J. Appl. Phys.* **15**, 22 (1944)

71. F.J. Zerilli and R.W. Armstrong, *J. Appl. Phys.* **61**, 1816 (1987)

72. P.S. Follansbee, U.F. Kocks, *Act. Met.* **1**, 81-93 (1988)

73. U.F. Kocks, *Mat. Sci. Eng*. **A317**, 181-187 (2001)

74. S. Nemat-Nasser and Y.L. Li, *Acta. Mater.* **46**, 565-577 (1998)

75. S. Nemat-Nasser, L. Ni, T. Okinaka, *Mech. Mat.* **30**, 325-341 (1998)

76. S. Nemat-Nasser, T. Okinaka, and L. Ni, *J. Mech. Phys. Solids,* **46**, 1009-1038 (1998)

77. R. Kapoor and S Nemat-Nasser, *Met. Mat. Trans.* **31A**, 815-823 (2000)

78. S. Nemat-Nasser, Physically-based Rate- and Temperature-Dependent Constitutive Models for Metals in *Handbook of Material Behavior Models*, edited by J. Lemaitre (Academic Press, San Diego, 2001), 387-397.

79. D.M. Goto, J.F. Bingert, W.R. Reed and R.K. Garrett, Jr, *Scripta Mater.* **42**, 1125–1131 (2000)

80. O. Oussouaddi, L. Daridon, S. Ahzi, D. Bouami, *Revue de Mécanique Appliquée et Théorique,* **1**, 239-251 (2003)

81. B. Banerjee, *Int. J. Sol. Struc.* **44**, 834-859 (2007)

82. B. Banerjee and A.S. Bhawalkar, *J. Mech. Mat. St.* **3**, 391-424 (2008)

83. B. Holmedal, *Act. Mat.* **55**, 2739-2746 (2007)

84. M-C Cai, L-S. Niu, X-F Ma, H-J Shi, *Mech. Mats.* **42**, 774-781 (2010).

85. S.P. Baker, Mechanical Behavior of Thin Film in *Enc. Cond. Mat. Phys.*, edited by O. Gourdon, D. Gout and G.J. Miller (Elsevier, Amsterdam, 2005), 187-194.

86. O. Kraft and H. Gao, Measurement of Stresses in Thin Films and Their Relaxation in Diffusion Processes in Advanced Technological Materials edited by D. Gupta (Springer, Berlin Heidelberg, 2005) 365-404

87. C.V. Thompson. *J. Mat. Res.* **8**, 237-238 (1993)

88. G. Dehm, B.J. Inkson, T.J. Balk, T. Wagner, and E. Arzt, *Mat. Res. Soc. Symp. Proc.* **673**, P2.6.1-P2.6.12 (2001)

89. E. Arzt, G. Dehm, P. Gumbsch, O. Kraft, D. Weiss, *Prog. Mat. Sci.* **46,** 283-307 (2001)

90. G. Dehm, T. Wagner, T.J. Balk, E. Arzt, B.J. Inkson, *J. Mater. Sci. Technol.* **18**, 113–7 (2002)

91. G. Dehm, T.J. Balk, H. Edongue, E. Arzt, *Microelectron. Eng.* **70**, 412–24 (2003).

92. G. Dehm, *Prog. Mat. Sci*. **54**, 664–688 (2009)

93. M. J. Kobrinsky and C.V. Thompson, *Acta Mater.* **48**, 625-633 (2000)

94. J. Weertman, *Trans. ASM* **61**, 681-694 (1968)

95. M.F. Ashby, *Act. Mat.* **20**, 887-897 (1972)

96. M.F. Ashby and H.J. Frost, The Kinetics of Inelastic Deformation above 0 K in *Constitutive Equations in Plasticity*, edited by A.S. Argon (The MIT Press, Cambridge, 1975)

97. H.J. Frost and M.F. Ashby, Deformation Mechanism Maps, The Plasticity and Creep of Metals and Ceramics, Pergamon Press, Oxford, 1982.

98. F.R. Brotzen, C.T. Rosenmeyer, C.G. Cofer, and R.J. Gale, *Vacuum* **41**, 1287-1290 (1990)

99. R.P. Vinci and J.J. Vlassak, *Annu. Rev. Mater. Sci.* **26**, 431-62 (1996)

100. S. Arrhenius, *Zeit. Phys. Chem.* **4**, 226 (1889)

101. A.A. Frost and D.R. Kalwarf, *J. Chem. Phys.* **21**, 264-267(1953)

102. F.X. Schumacer, *J. Forestry* , 819-820 (1939)

103. K. I. Ramachandran · G. Deepa · K. Namboori, Computational Chemistry and Molecular Modeling, Principles and Applications, Springer Verlag, Berlin, 2008, pp. 326-332

104. A.T. Johnson, Curfitting in Digital Biosignal Processing edited by R. Weitkunat (Elsevier, Amsterdam, 1991), 309-336

105. A. Seeger, The Mechanism of Glide and Work Hardening in Face-Centered Cubic and Hexagonal Close-Packed Metals, in Dislocations and Mechanical Properties of

Crystals edited by J.G. Fisher, W.G. Johston, R. Thomson, T. Vreeland, Jr. (John Wiley & Son, Inc., New York, 1957), 243-327

106. J. Friedel, Regarding Seeger's Paper on Work Hardening, in Dislocations and Mechanical Properties of Crystals edited by J.G. Fisher, W.G. Johston, R. Thomson, T. Vreeland, Jr. (John Wiley & Son, Inc., New York, 1957), 330-332.
107. R.E. Smallman and R.J. Bishop, Modern Physical Metallurgy and Materials Engineering: Science, Process, and Applications 6th ed., Butterworth Heinemann, Oxford, 1999.
108. T.G. Langdon and F.A. Mohamed, *J. Mat. Sc.* **13**, 1282-1290 (1978)
109. T.G. Langdon and F.A. Mohamed, *Mat. Sc. Eng*. **32**, 103-112 (1978)
110. J.S. Langer, E. Bouchbinder, T. Lookman, *Act. Mat.* **58**, 3718-3732 (2010)
111. P.S. Follansbee, U.F. Kocks, and G. Regazzoni, *J. de Physique* **8**(46), C5-25 (1985)
112. R. Klucka and L. Kubacek, *Chem. And Intel. Lab. Syst.* **39**, 69-75 (1997)
113. R. Sundberg, *Chem. And Intel. Lab. Syst.* **41**, 69-75 (1998)
114. S.R. Logan, *J. Chem. Ed.* **59**, 279-281 (1982)
115. K.J. Laidler, *J. Chem. Ed.* **61**, 494-498 (1984)
116. M. Menzinger and R. Wolfgang, *Angew. Chem.* **81**, 446 (1969)
117. M. Schwaab and J.C. Pinto, *Chem. Eng. Sci*. **62**, 2750-2764 (2007)
118. M. Schwaab, L.P. Lemos, J.C. Pinto, *Chem. Eng. Sci.* **63**, 2895-2906 (2008)
119. K. Lu and M.L. Sui, *Script. Met. Mat.* **28**, 1465-1470 (1993).
120. E. Arzt, *Acta Mat.* **46**, 5611-5626 (1998)

Biographical Information

Rahmat Saptono did a five year undergraduate study in Metallurgical Engineering at the University of Indonesia and earned his degree in the late 1993. He started his career at the University in 1995 as a Junior Faculty Member. During the early periods of his academic career, he attended non degree postgraduate courses in Metallographic Analysis at the National Agency for Atomic Energy in Indonesia and Non-Destructive Test at North East Wales Institute of Higher Education in the UK while working as a Trainee Engineer at the Center for Material Testing and Failure Analysis. In 2000 he was awarded an Australian Development Scholarship to pursue his Master degree at the University of New South Wales in Australia and earned a Master of Science and Technology in Engineering Materials in 2002. He continued his career at the University as a Lecturer in Mechanical Metallurgy and Engineering Design Principles as well as Head of Metal Forming Laboratory.

In 2010, he received a 3 years Fulbright-DIKTI Program Scholarship to pursue his Ph.D. degree in Material Science and Engineering at the University of Texas at Arlington.